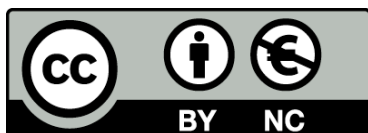




UNIVERSITAT_{DE}
BARCELONA

DBD plasma reactor for CO₂ methanation

Martí Biset Peiró



Aquesta tesi doctoral està subjecta a la llicència **Reconeixement- NoComercial 4.0. Espanya de Creative Commons**.

Esta tesis doctoral está sujeta a la licencia **Reconocimiento - NoComercial 4.0. España de Creative Commons**.

This doctoral thesis is licensed under the **Creative Commons Attribution-NonCommercial 4.0. Spain License**.

Tesi doctoral

DBD plasma reactor for CO₂ methanation

Martí Biset Peiró



UNIVERSITAT DE
BARCELONA

DBD plasma reactor for CO₂ methanation

Programa de Doctorat en Nanociències

Autor:

Martí Biset Peiró



Directora:

Dra. Teresa Andreu Arbella

Tutor:

Prof. Joan Ramón Morante Leonart

Lloc on s'ha dut a terme la tesi

Institut de Recerca en Energia de Catalunya (IREC)



UNIVERSITAT DE
BARCELONA



UNIVERSITAT DE
BARCELONA



Shaping Energy for a Sustainable Future

DBD plasma reactor for CO₂ methanation

Martí Biset Peiró



Aquesta tesi doctoral està subjecta a la llicència [Reconeixement-NoComercial 4.0. Espanya de Creative Commons](#).

Esta tesis doctoral está sujeta a la licencia [Reconocimiento-NoComercial 4.0. España de Creative Commons](#).

This doctoral thesis is licensed under the [Creative Commons Attribution-NonCommercial 4.0. Spain License](#).

Index

List of acronyms	i
Acknowledgements	iii
Preface	v
Abstract	v
Resum	vii
Chapter 1: Introduction	1
1.1. CO ₂ Conversion.....	3
1.1.1. Overview. A perspective on the climate emergency	3
1.1.2. CO ₂ conversion process.....	5
1.1.3. CO ₂ to CH ₄ : Power to Gas	6
1.1.4. Methanation technologies	8
1.2. Plasma	10
1.2.1. Plasma background.....	10
1.2.2. Plasma generation	12
1.2.3. High-pressure plasma. Arc Discharge	13
1.2.4. Dielectric Barrier Discharge	15
1.3. Plasma reactions and plasma-catalysis	17
1.3.1. Plasma-chemical reactions	17
1.3.2. Plasma-catalysis	18
1.4. State of the art	21
1.4.1. Catalyst for CO ₂ methanation	21
1.4.2. Plasma CO ₂ conversion	22
1.5. Aim of the thesis.....	23
1.6. References	24
Chapter 2: DBD reactor setup and experimental methodology	29
2.1. Introduction	31
2.2. Experimental setup overview	31
2.3. DBD-catalytic reactor	33
2.3.1. DBD reactor configuration: thermal, pseudo-adiabatic and adiabatic	34
2.4. Electrical system	36

2.4.1. Plasma power supply	36
2.4.2. Electrical characterization	37
2.4.3. Power measurement	38
2.5. Analytical system	39
2.6. Figures of merit	40
2.7. Catalyst synthesis	41
2.7.1. Ni catalyst supported in zeolites	42
2.7.2. One-pot synthesis of Ni-Ce catalyst	42
2.7.3. Wet impregnation of Ni-Ce on commercial mesoporous alumina	44
2.8. Summary	45
2.9. References	46

Part I. Catalyst for plasma CO₂ methanation

Chapter 3: Ni-Ce zeolite based catalyst	49
3.1. Introduction.....	51
3.2. Catalyst for CO ₂ methanation	52
3.2.1. Physicochemical characterization	52
3.3. DBD plasma reactor validation	55
3.4. Catalytic results of Ni-Ce zeolite	56
3.5. Discussion	61
3.6. Conclusions	64
3.7. Reference	65
Chapter 4: On the role of Ce in Ni-Ce/Al₂O₃ catalyst	69
4.1. Introduction	71
4.2. Catalyst	72
4.2.1. Physicochemical characterization	72
4.3. Catalytic results of Ni-Ce/Al ₂ O ₃	75
4.3.1. Effect of Ce	75
4.3.2. CO methanation	79
4.4. Discussion: difference in activation path	80
4.5. Energy efficiency and comparison with literature	82
4.6. Conclusions	85
4.7. References	86

Part II. DBD reactor configuration

Chapter 5: Adiabatic DBD plasma reactor	89
5.1. Introduction	91
5.2. Experimental setup: reactor and catalyst	92
5.3. Results	93
5.3.1. Adiabatic and pseudo-adiabatic reactor	93
5.3.2. Gas flowrate effect	96
5.3.3. Adiabatic configuration at high GHSV	97
5.4. Energy efficiency	99
5.5. Conclusions	102
5.6. References	103
Chapter 6: Plasma ignition and autothermal operation	105
6.1. Introduction	107
6.2. Experimental setup: hybrid DBD adiabatic reactor	108
6.3. Results	109
6.3.1. Plasma ignition	109
6.3.2. Autothermal operation	111
6.3.3. Fast and efficient operation	114
6.4. Discussion	117
6.5. Conclusions	119
6.6. References	120
Chapter 7: Conclusions	121
Appendix	127
A. Appendix of chapter 2	129
B. Appendix of chapter 3	135
C. Appendix of chapter 4	136
D. Appendix of chapter 5	144
E. Appendix of chapter 6	148
Curriculum vitae	153

List of acronyms

Acronyms

AC	Alternating current
APGD	Atmospheric pressure glow discharge
BET	Brunauer-Emmett-Teller
BF TEM	Bright-field transmission electron microscopy
BJH	Barrett-Joyner-Halenda
DBD	Dielectric barrier discharge
DC	Direct current
DRIFTS	Diffuse reflectance infrared Fourier transform spectroscopy
EC	Energy cost
EELS	Electron energy loss spectroscopy
EISA	Evaporation-induced self-assembly
GA	Gliding Arc
GHS	Greenhouse gas
GHSV	Gas hourly space velocity
H ₂ -TPR	Hydrogen temperature programmed reduction
HAADF	High-angle annular dark-field imaging
HRTEM	High-resolution transmission electron microscopy
HV	High voltage
ICDD	International centre for diffraction data
IPC	In-plasma catalysis
IPC	Plasma elemental analysis
IPCC	Intergovernmental panel on climate change
LHV	Low heating value
LTE	Local thermal equilibrium
non-LTE	Non local thermal equilibrium
P2G	Power-to-Gas
PEM	Polymer electrolyte membrane
PPC	Post-plasma catalysis
RES	Renewable energy sources
RWGS	Reverse water gas shift
SEI	Specific energy input

List of acronyms

SNG	Synthetic natural gas
SS	Stainless steel
TCD	Thermal conductivity detectors
TEM	Transmission electron microscopy
TGA-DSC	Thermogravimetric analysis - Differential Scanning Calorimetry
uGC	Micro gas chromatography
VOCs	Volatile Organic Compounds
XRD	X-ray diffraction

Acknowledgements

First of all, I would like to thank my research supervisor Dra. Teresa Andreu for giving me the opportunity and confidence to do the PhD at IREC. A long road that I started 6 years ago with the master thesis, doing water splitting in a small setup at the ESEH lab. Thank you for your patience, knowledge, and support during all this time.

I would like to thank my tutor and head of the group, Prof. Juan Ramon Morante to give me the opportunity to work and contribute to the ESEH group. Also, I want to especially thank Dr. Jordi Guilera for all the support given during the PhD. Together with Dra. Teresa Andreu have contributed a lot to improve my skill, my publications and knowledge in the field of catalysis.

To my friends and colleagues of the ESEH group; Nina, Sebastián, Jordi Jacas, Erdem, Hemesh, Carles, Javi, Miriam, José Antonio, José Miguel, Antonio Miguel, Andreina, Viktoriia, Kele, Tandava, Marcelo, Monalisa, Marisa, Elias, Prakasha, PengYi, Ting, ... It has been a pleasure to work and collaborate with all of you and, of course, to share many good moments outside the lab.

To other colleagues at IREC, in special thanks to Dra. Diouldé, Dra. Doris, Dra. Yudania and Dr. Albert, for the good moments, advice, and support.

And, lastly, of course, to my family and friends for your continuous support and love.

Financial support

I also gratefully acknowledge the funding of this work by CoSin project (COMRDI15-1-0037), funded by ACCIÓ and the European Regional Development Fund(FEDER) under the RIS3CAT Energy Community. The work was also partially supported by MCIN/AEI/10.13039/501100011033 projects CCU+OX(PID2019-108136RB-C33), WINCOST(ENE2016-80788-C5-5-R), PEJ-2014-A22497 grant and by Generalitat de Catalunya, M2E(2017SGR1246).

Abstract

One of the most serious challenges facing society is the need to reduce the emissions of greenhouse gases such as carbon dioxide (CO₂), mainly caused by the widespread use of fossil fuels. The energy transition to renewable energies is currently in its initial stages of its implementation. Due to the need to increase renewable energy sources, it is necessary to develop new technologies that can adapt the fluctuating generation of renewables with the energy consumption.

The conversion of CO₂ into synthetic fuels using electrical energy, technologies known as Power to Gas, presents a solution to the energy storage. In the specific case of the methanation reaction, CO₂ is converted to methane (CH₄, synthetic natural gas), which can be stored and distributed in large quantities. In this way, synthetic natural gas is used as an energy vector, providing a solution as energy storage and as a method of CO₂ valorization.

In the last years, Power to Gas technologies are being implemented in several pilot plants with conventional thermochemical technologies for the methanation reaction. In this regard, alternative methods to thermal catalysis are being studied, which could potentially have advantages in terms of conversion or reduction of energy costs, among others. The use of plasmas in the conversion of CO₂ is particularly promising due to the ability of plasma to activate stable molecules such as CO₂ or N₂.

In this context, the aim of this thesis is the development of a dielectric barrier discharge plasma reactor for the conversion of CO₂ to CH₄, the development of catalysts for this reaction and the optimization of both the catalysts and the plasma reactor. Following these objectives, the thesis is structured in 6 main chapters. The first chapter presents the general context, the motivation of the research regarding CO₂ conversion technologies and a basic introduction of plasma technologies. In chapter 2, all experimental setup and material synthesis are explained. The following chapters are focused on the main results obtained during the development of the thesis, which can be divided into two parts. The first part is focused on the catalyst evaluation for plasma-CO₂ methanation (chapter 3 and chapter 4). The second part is focused on the optimization of the plasma reactor (chapter 5 and chapter 6).

In the catalyst evaluation for plasma-CO₂ methanation, different types of catalyst were synthesized, physicochemical characterized and evaluated in thermal and plasma methanation. Operation temperature was reduced to 100-200 °C in the case of plasma methanation. The effect of different catalysts composition and structure was analyzed. The incorporation of cerium in nickel based catalyst boosted the conversion and efficiencies. The different role of plasma activation and catalyst activity were evaluated.

In the second part, DBD reactor optimization, different reactor configurations were tested. The role of temperature was analyzed in pseudo-adiabatic and adiabatic DBD reactor. The use of adiabatic reactors allows to increase the energy efficiency. Finally,

a new approach was evaluated based on using DBD-plasma as reaction ignitor, rather than the classical approach of continuous operation. After plasma ignition, the operation in autothermal conditions without any external energy input was evaluated. The new methodology allowed to faster start the reaction, due to the plasma activation at a lower temperature, minimizing the start-up time and the energy cost.

Resum

Un dels reptes més importants al qual s'enfronta la societat és la necessitat de reduir les emissions de gasos d'efecte hivernacle, principalment el diòxid de carboni (CO_2), causades per l'ús generalitzat dels combustibles fòssils. La transició energètica cap a energies renovables està actualment en les primeres fases de la seva implementació. Atesa la necessitat d'augmentar les energies renovables, és necessari desenvolupar noves tecnologies que puguin adaptar la generació fluctuant de les renovables amb el consum energètic.

La conversió de CO_2 a combustibles sintètics emprant energia elèctrica, tecnologia que es coneix com a *Power to Gas*, presenta una solució a l'emmagatzematge d'energia. En el cas concret de la reacció de metanització, el CO_2 és convertit a metà (CH_4 , gas natural sintètic), el qual es pot emmagatzemar i distribuir en grans quantitats. D'aquesta forma, el gas natural sintètic s'utilitza com a vector energètic, proporcionant una solució al emmagatzematge d'energia i com a mètode de valorització de CO_2 .

En els últims anys, s'estan implementant diferents projectes a nivell de plantes pilots utilitzant tecnologies termoquímiques per a la metanització. En aquest aspecte, també hi ha interès en el desenvolupament de mètodes alternatius a la catàlisi tèrmica, que puguin potencialment presentar avantatges, entre d'altres, en termes de conversió o reducció dels costos energètics. L'ús de plasmes en la conversió de CO_2 és particularment prometedor, degut a la capacitat del plasma per activar molècules estables com CO_2 o N_2 .

En aquest context es presenta la tesi amb l'objectiu de desenvolupar un reactor de plasma de descàrrega de barrera dielèctrica per a la conversió de CO_2 a CH_4 , el desenvolupament de catalitzadors per a aquest reacció i la optimització tant dels catalitzadors com del reactor de plasma. Seguint aquests objectius, la tesi s'estructura en 6 capítols. El primer capítol presenta el context general, la motivació de la investigació i una introducció bàsica de les tecnologies de plasma. En el segon capítol s'explica tota la configuració experimental del reactor de plasma i la síntesi de catalitzadors. En els següents capítols es mostren els principals resultats obtinguts durant el desenvolupament de la tesi, els quals es divideixen en dues parts. La primera part comprèn els capítols 3 i 4 i se centra en l'avaluació de catalitzadors per a la reacció de metanització del CO_2 . La segona part se centra en l'optimització del reactor de plasma (capítols 5 i 6).

En la primera part, avaluació de catalitzador per a la metanització amb plasma, es van sintetitzar diferents tipus de catalitzadors, es van caracteritzar fisicoquímicament i avaluar en la metanització tèrmica i metanització amb plasma. En el cas de la metanització amb plasma, la temperatura de treball es va reduir fins als 100-200 °C. Tot seguit es va estudiar l'efecte de la composició i l'estructura de diferents catalitzadors. La incorporació de ceri en els catalitzadors de níquel augmentà

considerablement els nivells de conversió i eficiència energètica. Finalment, s'ha avaluat el rol de l'activació mitjançant el plasma i l'activació del catalitzador.

En la segona part, l'optimització del reactor, es van analitzar diferents configuracions del reactor de plasma. Es va analitzar el rol de la temperatura en configuracions pseudo-adiabàtica i adiabàtica, demostrant que l'ús de reactors adiabàtics ha permès augmentar l'eficiència energètica. Finalment, es va avaluar un nou enfocament basat en l'ús del plasma DBD com a iniciador de la reacció, en lloc de l'enfocament clàssic d'operació contínua. Després de l'encesa del plasma, es va avaluar el funcionament en condicions autotèrmiques, sense cap aportació externa d'energia. La nova metodologia permet iniciar més ràpidament la reacció, gràcies a l'activació del plasma a baixes temperatures, minimitzant el temps i el cost energètic.

Chapter 1

Introduction

1.1 CO₂ conversion

1.1.1 Overview. A perspective on the climate emergency

The human influence on the climatic change due to the emissions of greenhouse gases (GHG) is already considered an established fact [1]. The main GHG is CO₂, which anthropogenic emissions over the last century have raised the concentration in the atmosphere from 275 ppm to 400 ppm (**Figure 1.1**). These atmospheric concentration values had not been reached for more than 2 million years [1]. The main human source of CO₂ comes from the combustion of fossil fuels, which emissions reached 37.5 Gt only in 2018 [2], involving an increase of 20 Gt over the last 50 years. Even with the different climate policies, the CO₂ emissions continuously grow every year, and no signs of peaking are observed.

In this regard, the Intergovernmental Panel on Climate Change (IPCC) publishes regular assessments of climate change, giving scientific basis, impacts, future models, options for adaptation and mitigation information. In 2014, the IPCC released the five-assessment report, where it made clear the effects and the importance to reduce fossil fuels during the next decade [3]. Afterwards, in the Paris Agreement, 196 parties (174 states and the European Union) agreed to implement different climate policies to limit the global warming to below 2 °C, above pre-industrial levels [4]. The sixth report of IPCC has been released recently, following the same trends of the 2016 report, while room for manoeuvre is reduced.

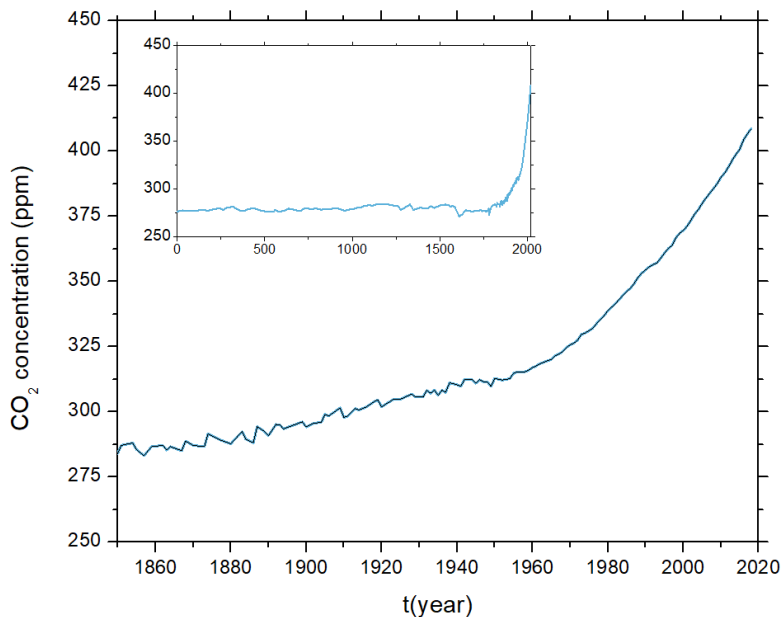


Figure 1.1. Average atmospheric CO₂ concentration. Data adapted from [5].

Evidence already corroborated the increase in global surface temperature caused by humans (**Figure 1.2**), which has increased faster in the last 50 years than over any similar period over the last 2000 years. The assessment also reported the different effects; warming, change in precipitation, glacier retreat, decrease in Arctic sea ice, global acidification of oceans, sea level increased, etc. Many of these changes have scales unprecedented over centuries to thousands of years.

All this data and facts mark the urgent need to reduce CO₂ levels. The percentage of energy from renewable energy sources (RES) must be increased, as opposed to fossil fuels (whether oil, natural gas or coal).

On the other hand, the direct CO₂ emissions could also be reduced by CO₂ re-utilization and conversion to value-added products (fuels and materials) as a direct alternative to the use of fossil fuels as a primary energy source or raw material in the chemical industry. In order to be effective, this approach should be applied with an emphasis on the conversion of CO₂ from biologic origin (e.g., biogas), waste management or industry where the generation of CO₂ could not be eliminated (e.g., cement plant, steel production or fermentation process), rather than the CO₂ recycling from fossil fuels combustion.

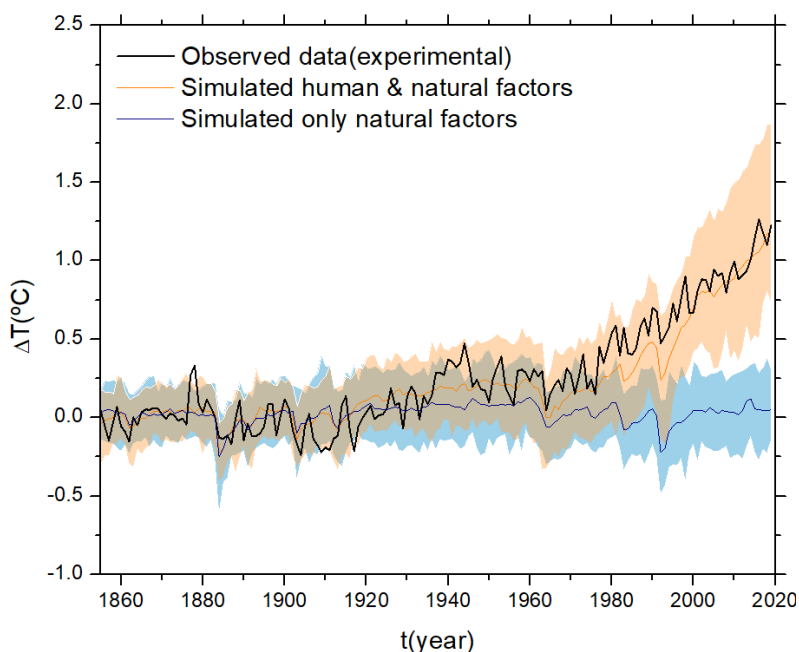


Figure 1.2. Change in global surface temperature (1850-2020): observed average annual temperature, simulated using human and natural factors, and simulated using only natural factors (solar and volcanic). Data adapted from IPCC (2021) [6].

1.1.2 CO₂ conversion process

There are different options to valorize and transform CO₂ into value-added products [7]. The possible products have applications in different markets, such as energy and transportation (synthetic fuels), agriculture (fertilizers) and other chemicals and materials (e.g., plastics, adhesives, cosmetics, cleaning solutions, antiseptics, etc.).

Regarding the CO₂ origin, CO₂ can come from biogenic sources (biogas or biomass), industrial processes (cement, steel, fermentation, chemical industry, etc.) or even from air capture. Following the recommendations explained in the previous section, it is necessary to reduce fossil fuels. Thus, the carbon source (CO₂) should come from waste and biological (biogas, biomass) or industrial sources rather than from a fossil origin.

On the other hand, several CO₂ conversion processes use hydrogen as a co-reactant to form different products. The three basic hydrogen sources for CO₂ hydrogenation are H₂O, CH₄ and H₂. In this regard, it is important to consider the origin of the hydrogen source from an environmental impact point of view. Currently, almost all the hydrogen that is produced in the world (95%) is generated from fossils fuels by natural gas reforming. The generated hydrogen is classified as grey hydrogen, as during the process is generating high quantities of CO₂ (11 tons of CO₂ per ton of H₂) [8]. The green alternative is to produce the hydrogen using RES (like water electrolysis using RES) being a clean hydrogen source from an environmental point of view.

Regarding the conversion to fuels [9], **Figure 1.3** presents the most typical routes for CO₂ conversion. Processes can be divided into direct hydrogenation of CO₂ and process in which CO₂ is firstly reduced to CO and then hydrogenated with H₂. In this last option, the mixture obtained is known as syngas (CO/H₂) and is used as a raw reactant. For example, synthetic fuels can be obtained by Fisher-Tropsch synthesis,

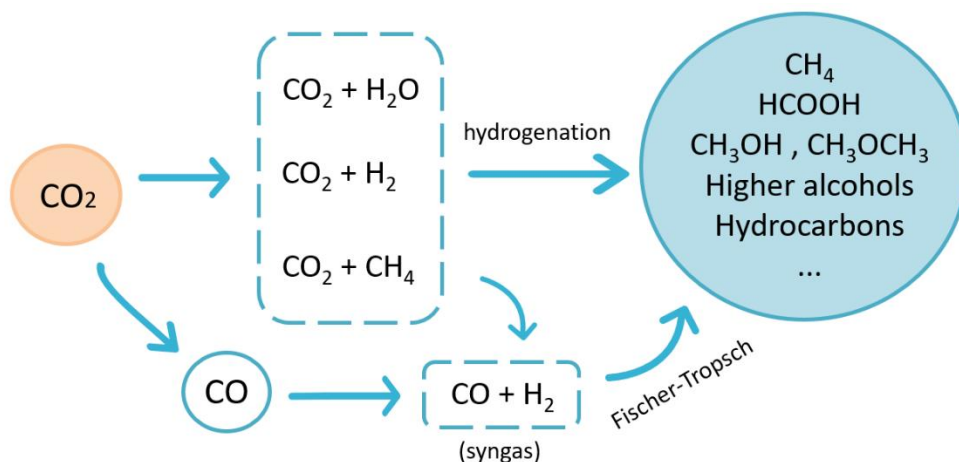


Figure 1.3. CO₂ conversion to C₁-C₅ fuels-chemicals with H₂O, H₂ and CH₄ as co-reactants or by CO₂ reduction to CO.

where long chains C_5 to C_{18} are produced (similar products as diesel and gasoline). By this way, synthetic fuels can be obtained from alternative sources (e.g., biogenic) to fossil ones.

On the other hand, the direct hydrogenation of CO_2 is performed with different co-reactants as hydrogen sources. In the same way of syngas reactions, different products could be obtained, from C_1 molecules (CH_4 , CH_3OH , $HCOOH$, CH_2O_2 , etc.), C_2 (C_2H_6 , C_2H_4 , etc.), to higher C_{3+} molecules (alcohols and hydrocarbons).

Among all the possible products exposed, the valorization of CO_2 through its hydrogenation to CH_4 has a great interest in its application in the field of energy storage. Specifically, methane is proposed as an energy carrier capable of storing large amounts of energy. This is the basis of technologies known as Power-to-gas (PtG), which can provide a solution in the intermittent nature of RES.

1.1.3 CO_2 to CH_4 : Power to Gas

It is well known that RES have an intermittent character in time, depending on external factors (intensity of the sun, wind, meteorology, etc). In addition, the energy transition plans developed in the EU aim to increase the RES of the total energy during the next years [10]. This supposes a change from fossil energies that can be adapted very well to the demand at any time, to other energies less flexible over time. In order to take full advantage of the RES and improve its flexibility, the energy surplus during peak productions can be stored and used when the demand increases. The selected storage technologies must be capable of storing large amounts of energy over a long period of time. Among the different technologies (**Figure 1.4**), the use of fuels, whether hydrogen or methane, are the technologies capable of storing large quantities of energy.

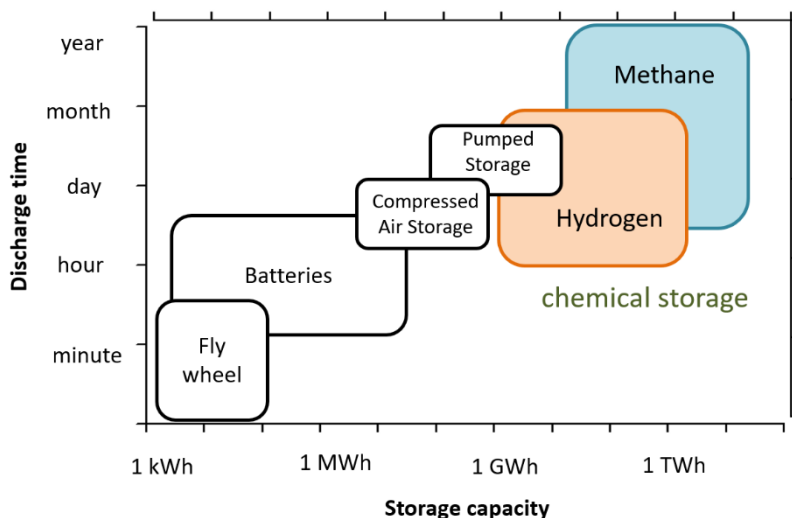


Figure 1.4. Energy storage technologies.

The technology that generated gaseous fuels using the energy surplus from the electrical grid is known as Power-to-Gas technologies (**Figure 1.5**). The first option is the use of hydrogen as an energetic vector, produced from the electrolysis of water. However, this technology has some bottlenecks for its deployment, mainly the lack of infrastructure. In this sense, hydrogen can be injected into the natural gas grid. However, the current policy limits the amount of hydrogen to a 1-10%. Specific infrastructure needs to be built to transport pure H₂, being one of the key priority areas in the European Green Deal.

An alternative is to combine the H₂ and CO₂ to produce CH₄ (as seen in the previous section). The obtained CH₄, known as synthetic natural gas (SNG), can be injected directly into the natural gas grid. The SNG has to fulfil the quality requirement in terms of purity, which depends on the country (>90 % of CH₄ in Spain).

In summary, the main advantages of CO₂ conversion to CH₄ and its use as chemical storage are:

- Transport vector of H₂ .
- Long term and high capacity of energy storage.
- Easy implementation using the natural gas infrastructure.
- Reuse and valorization of CO₂. Valorization of biogenic CO₂. In this sense, they are also a solution to issues of organic waste treatment. Valorization of CO₂ from industrial processes. Generation of carbon-neutral methane.

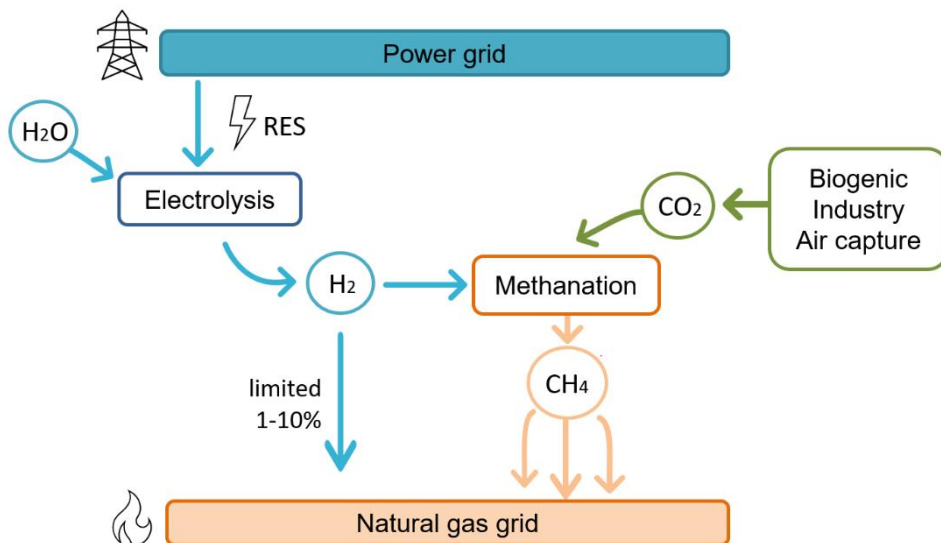
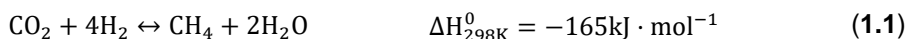


Figure 1.5. Scheme of Power to Gas.

1.1.4 Methanation technologies

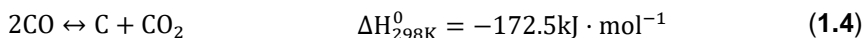
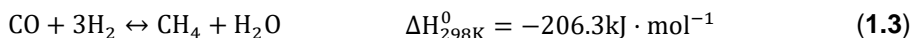
There are several methanation technologies such as thermochemical, biological, photoelectrochemical or plasma methanation among others [11]. The most developed methanation technology is the thermochemical, currently developed in several pilot plants in PtG research projects [12,13].

In thermochemical routes, the conversion of CO₂ to CH₄ is done by the Sabatier reaction (**Eq. 1.1**), which is an exothermic reaction.



The reaction is thermodynamically favoured at high pressure and low temperature (Le Chatelier's principle), shifting the equilibrium to higher CO₂ conversion. However, the use of catalyst and moderated temperatures are necessary to activate the CO₂ molecule and overcome the activation barrier (kinetic limitations) [14].

On the other hand, the reaction has a thermodynamic limit at high temperatures due to the appearance of secondary reactions such as reverse water gas shift (RWGS) (**Eq. 1.2**), shifting the selectivity to CO.



Other important secondary reactions are reverse dry reforming (**Eq. 1.3**) and Boudouard reaction (**Eq. 1.4**) [14]. The Boudouard reaction is one of the mechanisms that cause carbon deposition on the catalyst, which leads to catalyst deactivation. The carbon deposition is favoured at a higher temperature compared with the methanation reaction (<450 °C), despite at lower temperature have also been observed [15]. In addition, the catalyst structure can be modified by metal sintering at high temperatures, decreasing the activity.

According to all the above-mentioned constraints, the application of catalyst that can work at low temperatures is preferred. In thermochemical methanation, the reaction is typically performed at moderated temperature (250-500 °C) and pressure (1-10bar). Due to its exothermic nature, temperature management in the reactor is essential for high productivity. The objective of temperature control is to avoid hot spots while keeping the temperature in the optimal range to maximize conversion.

In this sense, there are different types of thermal catalytic reactors [12,14]. From the structural configuration, reactors can be divided into: fix-bed reactors, fluidized bed reactors, three-phase and microstructured reactors. In addition, depending on the thermal management (adiabatic, diathermic, etc) different temperature profiles can be obtained (isothermal, polytropic, etc).

Although most applications use fixed bed configuration, new approaches of thermal reactors have been investigated over the last years [16–19]. The new configurations promise to increase the performances in thermo-catalytic methanation (yields and energy efficiency). On the other hand, there is interest to use different technologies to perform the methanation reaction.

In this regard, during the last years, the use of plasma has been proposed as an alternative method to thermo-catalytic route for the CO₂ conversion [20,21]. Compared to thermo-catalytic process, the use of plasma promises to have advantages in terms of synergetic effect between plasma and catalyst, operating at mild conditions and fast reaction start-up times (**Figure 1.6**). Even plasma technology is already applied at commercial levels for some chemical reactions (e.g., ozone generation), the application in the CO₂ methanation is recently new and further investigations are needed. In this context, the essential background about plasma and plasma-catalytic reactors for CO₂ methanation are presented in the following sections.

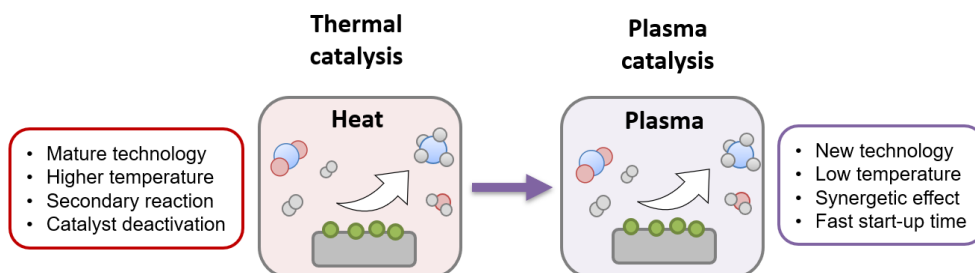


Figure 1.6. Thermal-catalysis and plasma-catalysis comparison.

1.2 Plasma

1.2.1 Plasma background

Plasma is usually known as the fourth state of matter, being an easy way to understand and visualize it. In this sense, following the different state transitions when heat is supplied (solid to liquid and liquid to gas), gas can be transformed to a new state, known as plasma, where some gas molecules are ionized (**Figure 1.7**). In this plasma state, the gas is found in some degree of ionization (fully or partially), meaning that some of the electrons are unbound from the atoms, forming ions and free electrons. Thus, the main constituents of plasma are positive ions, electrons, negative ions and neutral particles. In addition, the interaction between the electrons and heavy particles (molecules) generates additional species as excited molecules and radicals. All these reactive species are interesting for chemical conversion applications, as will be explained in the next section.

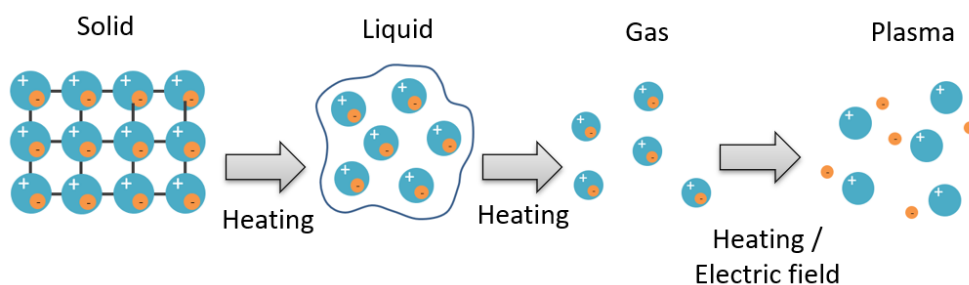


Figure 1.7. The three classic states of matter and plasma as the 4th state of matter.

Plasma is an electrically conductive gas due to the presence of these electrically charged species and can be affected by electromagnetic fields. Despite this, the plasma is electrically neutral (quasi-neutral) at the macroscopic scale, as negative and positive charges are presented in the same proportion. The ionization degree of the plasma (α) is defined as the ratio between the amount of ions (n_i) and the total number of species, including the neutral particles (n_n) defined by **Eq. 1.5**.

$$\alpha = \frac{n_i}{n_i + n_n} \quad (1.5)$$

There are a large variety of plasma with different ionization degree, ranging from fully ionized plasma ($\alpha \approx 10^{-1}$) to partially ionized or weakly ionized ($<10^{-6} < \alpha < 10^{-1}$) [22]. Moreover, the degree of ionization is also related to the plasma temperature.

One of the most important parameters is plasma temperature. As mentioned, plasma is made up of different components, which may not be in thermal equilibrium due to the considerable mass difference between them. Consequently, each group of particles can have different kinetic thermal energy, commonly called “particle

temperature". In particular, we can define three relative temperatures for the three main groups: neutral particles (T_{gas}), ions (T_i) and electrons (T_e). By considering the plasma temperatures and the ionization degree, the different types of plasma can be divided in two main blocks: high temperature or fusion plasma and low-temperature plasma (**Figure 1.8**) [20,23].

In high temperature plasma, the gas is usually completely ionized and in thermodynamic equilibrium, reaching temperatures between 10^6 and 10^8 K. In this category, we can find all the fusion plasma, such as tokamaks, stellarators, plasma pinches, solar wind, etc.

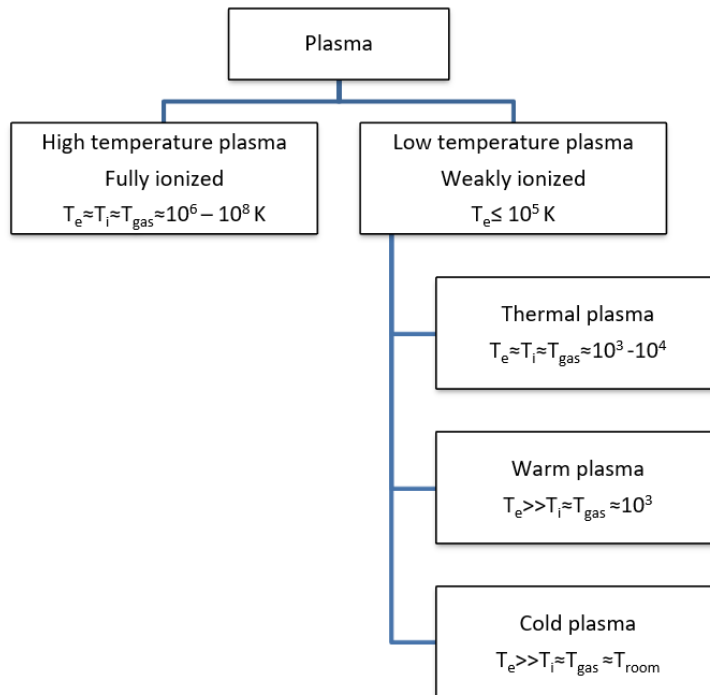


Figure 1.8. Plasma classification as a function of ionized degree and temperature.

On the other hand, we would have the low temperature plasmas, which are weakly ionized plasma with lower temperatures (10^5 K), also known as gas discharge plasmas, being the most used artificial type of plasma with several applications. The low-temperature plasma can be further divided into thermal plasma, warm plasma and cold plasma. Thermal plasmas are the ones that the plasma is found in quasi-equilibrium, or local thermal equilibrium (LTE), with a local equal temperature for all the species ($T_e \approx T_i \approx T_{\text{gas}}$). The temperature can reach values between $3 \cdot 10^3$ and $1 \cdot 10^4$ K. In the case of cold plasma, the different species are not in thermal equilibrium (non-LTE). The electron temperature can reach temperature of 10^5 K (higher than thermal plasma) while the gas temperature is kept at temperature near the room temperature ($T_e \gg T_i \approx T_{\text{gas}}$). These types of plasma are typically known as non-thermal plasmas.

Finally, warm plasma is a non-equilibrium plasma, but it has some properties of both thermal and cold plasma [20]. In these types of plasma, the gas temperature can reach 2000-3000 K while the electron temperature is still at higher temperatures ($T_e > T_i \approx T_{\text{gas}}$).

As mentioned before, there is a wide range of applications for low temperature plasmas. On the one hand, thermal plasmas are used in applications such as welding, cutting or spraying, in which elevated temperatures are needed. On the other hand, warm and cold plasmas are applied for chemical conversion, surface deposition and treatment, lamp and light generation and gas cleaning, among others.

Specifically, in chemical conversion, cold plasma stands out for its high chemical efficiency, as the input energy is mainly transferred to electrons (avoiding thermal losses) which generates high reactive species. In addition, cold plasma can be combined easily with catalyst, known as plasma-catalysis, increasing conversion and selectivity to the desired product.

1.2.2 Plasma generation

As explained in the previous section, gas can be transformed into plasma when heat is supplied. In this case, the energy to ionize the gas molecules is provided by thermal energy. However, the most typical way to generate plasma, in almost all applications, is by using an electromagnetic field. A large variety of plasma can be obtained using electromagnetic fields as several parameters can be varied, such as type and characteristics of electromagnetic field, temporal behaviour (e.g., direct current (DC), alternating current (AC), pulsed DC, etc.), discharge configuration (e.g., electrode and volume) or pressure and gas composition [24]. Thus, it provides different types of plasmas with specific characteristics (e.g., temperatures, species and plasma, interactions, LTE or non-LTE, etc.) [23]. In fact, by varying these parameters, the final reactions and excited species can be channelled to the desired ones [25].

In this thesis, we will focus on the plasma generated by applying an electric field between two electrodes. The most basic configuration consists of two metallic electrodes filled by a volume of gas (**Figure 1.9**). When a voltage is applied between the two electrodes, the free electrons present in the gas will be accelerated by the electric field. For the plasma ignition, the energy obtained by electrons must be sufficient to ionize the gas's neutral species. In that case, initial electrons can produce an avalanche effect, ionizing and generating more free electrons that, in turn, will ionize other atoms/molecules (**Figure 1.9**) [26]. By this chain reaction, the plasma is ignited. Apart from ionization, collisions between electrons and atoms/molecules will generate other species, such as excited species (electronic, vibrational and rotational), radicals, etc. The proportion between reactions and the produced species will depend on the type of plasma. The different reactions and species will be further discussed in **section 1.3**.

As we have commented, the electron energy must be sufficient to ionize and produce an avalanche effect. In this way, we can define a minimum voltage to generate plasma, known as breakdown voltage (V_b). The V_b mainly depends on the gas pressure and distance between electrodes (p-d). It also depends on constant parameters of the type of gas and used electrode. The V_b follows the Paschen's Law [27], as a function of p-d values, with a minimum voltage value that increased for higher p-d values. In this sense, the V_b can range from a few hundred volts up to thousands of volts.

After the plasma is ignited by the electrical breakdown process, the plasma can mainly evolve to a glow discharge or arc-spark discharge, depending on the configuration.

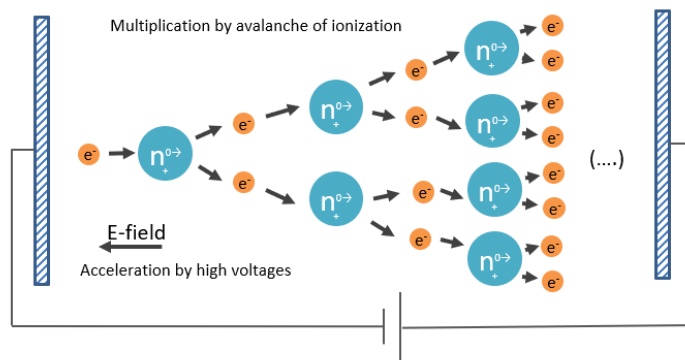


Figure 1.9. Basic plasma setup. Plasma generation by avalanche ionization between electrodes.

1.2.3 High-pressure plasma. Arc Discharge

It is easy to produce cold plasma (non-thermal plasma) at low pressure by the mechanism explained in the previous section. In these cases, the ionization process takes place in the bulk gas. The plasma is generated as a diffused discharge along the gap, known as Townsend discharge. However, when working at higher pressure (atmospheric pressure), some instabilities appear in the plasma, and the discharge characteristics change from diffused to arc-spark discharge. In some specific cases, glow discharge can be presented at higher pressure, known as atmospheric pressure glow discharge (APGD)[24].

In general terms, the collision frequency increases together with the number of electrons at high pressure. Consequently, the electric field generated by the charged species is no longer negligible compared to the applied electric field. The electric field is enhanced at the avalanche head, generating an intense autoionization in the avalanche head [22]. Consequently, the discharge is developed as a stream between the electrodes (**Figure 1.10**).

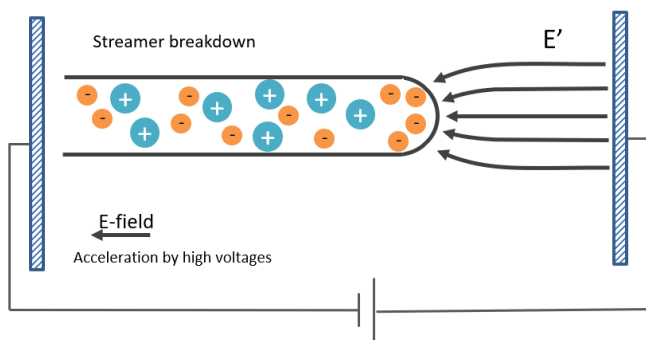


Figure 1.10. Plasma generation: stream mechanism.

An important difference, apart from the discharge formation mechanism, is the plasma properties generated. As a consequence of the increase in collision frequency and electron density, the gas heating increase, which can change the type of plasma from cold to thermal plasma. This is the case of arc discharge, which is an electrical discharge generated between two electrodes at atmospheric pressure (**Figure 1.11**). The electrical current can increase significantly while the temperature reaches values higher than 1000 °C. The higher temperatures make it useful for applications as welding or cutting. However, there are limitations to applying it in chemical conversion due to the elevated temperatures.

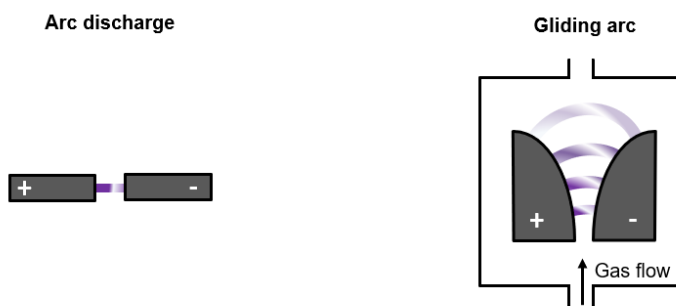


Figure 1.11. Arc discharge and gliding arc configuration.

A more interesting type of arc discharge is the gliding arc (GA) discharge. The GA is a type of plasma classified as warm plasma, with large electron density, current and power, while the gas temperature is kept at relatively low temperature (compared with thermal plasma). The simplest GA configuration is made with two diverging electrodes, where gas flows along the electrodes (**Figure 1.11**). When a certain voltage is applied, plasma is generated between the electrodes in the zone with the smallest distance. The discharge is displaced upwards due to the gas flows until it is extinguished. Right after, new discharges are reignited at the shortest electrode distance. Interestingly, at the closest position to the electrode, the generated plasma is a quasi-thermal plasma, and it becomes a non-thermal plasma as the discharge moves towards the upper part of the electrodes. Therefore, GA plasma combines both

thermal and non-thermal plasma generation, which make it interesting for some chemical conversion. However, the combination with catalyst is not trivial, and the higher temperature can be inconvenient for some applications.

1.2.4 Dielectric Barrier Discharge

Dielectric Barrier Discharge (DBD) is a type of plasma that works at atmospheric pressure and in non-thermal regime (cold plasma), which uses a dielectric material to limit the current and the transition to arc (thermal plasma) [28]. As explained previously, arc discharge is generated when a high voltage (HV) is applied between two electrodes at atmospheric pressure (in the range of kV). In order to avoid the transition to arc, discharges should stop previous to the arc transition, keeping the plasma in non-thermal regime. A typical method is to limit the current before the transition. DBD uses one or two dielectric layers between the electrodes in order to limit the current and the transition to an arc discharge. The dielectric material limits the current by blocking the current flow and charge deposition into the dielectric surface.

Thus, the plasma in DBD is generated as streams (as seen in the previous section), where the higher electron density produces a high space charge (modifying the electric field), producing a self-propagating stream. Once the stream is completely formed, the current flow through the gap and charges are accumulated at the dielectric surface. The charge accumulation produces that the local electric field is reduced until the point that the ionization is stopped, and the discharge is choked. In the case that the applied voltage is still higher than the V_b , additional discharge can be formed at different positions (far from the influence area of the first discharge, where the local field is reduced). Typically discharge has a diameter of 100 μm with a duration in the range of 100 ns [28].

Therefore, DBD plasma consists of several micro-discharges (10^6 micro-discharge per cm^2 and second) generated along all the electrode area [28]. The dielectric prevents the transition to thermal plasma and distributes the discharge over all the electrode area. On the other hand, the effect of charge accumulation on the dielectric surface limits the type of voltage to an AC signal (in the range of 1-10 kV and Hz to kHz).

An example of an applied voltage and measured current is shown in **Figure 1.12a**. The micro-discharges (observed as spikes in the current waveform) are generated during the half-cycle when the voltage is higher than the V_b . After the voltage is completely reversed, the plasma is again ignited. **Figure 1.12b** shows an example of DBD plasma. It can be observed the different micro-discharge formed around the electrode.

DBD can be configured with different geometries depending on the dielectric barrier and electrode configuration [29]. **Figure 1.13** shows the most common geometry; planar and cylindrical or coaxial. For gas conversion or treatment, the most used

configuration is the cylindrical, as it offers advantages in terms of easy materials, sealing and simple scalability. In this configuration, the electrodes and dielectric materials are directly the reactor's wall without needing any additional structure (walls).

In addition, DBD reactors allow filling the space between the electrode with packing material, in order to modify the plasma properties (dielectric materials) or work in plasma-catalysis configuration (catalytic materials). Thus, DBD plasma stands out as a cold plasma that can operate at atmospheric pressure, with easy catalyst incorporation (plasma-catalysis), easy structure and scale-up. DBDs have been applied for different uses, from ozone generation, surface modification, plasma chemical vapour deposition and flat plasma displays and chemical conversion. In addition, new applications are being investigated in plasma chemical conversion with DBD, such as volatile organic compounds (VOCs) degradation, NO_x abatement and CO_2 conversion [25].

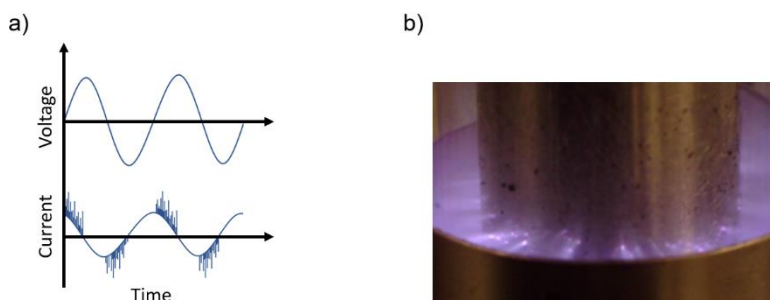


Figure 1.12. a) Voltage and current in DBD. b) Micro-discharge observed in DBD.

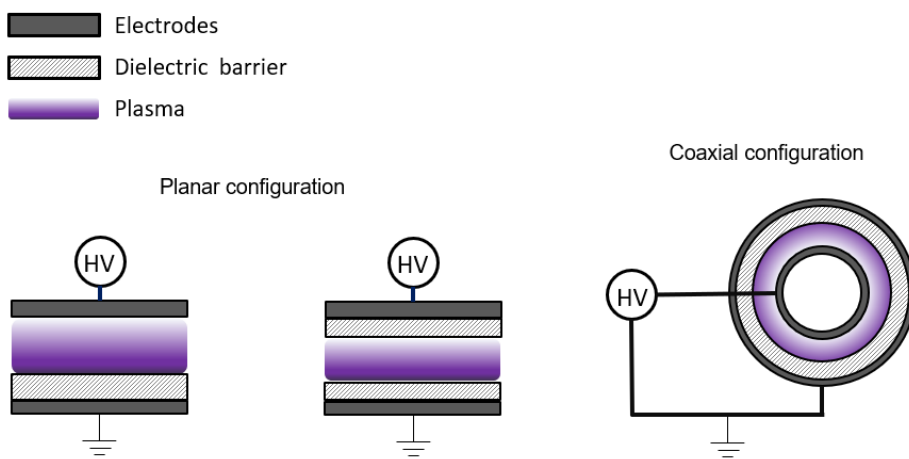


Figure 1.13. DBD reactor configuration (planar and coaxial).

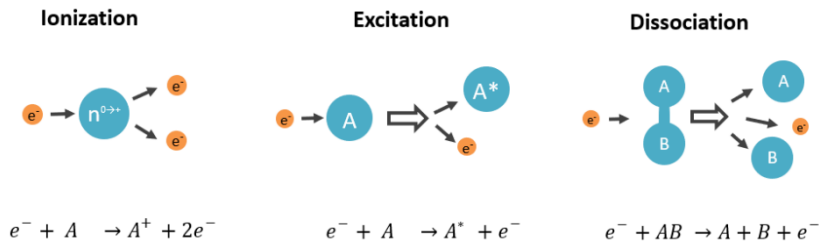
1.3 Plasma reactions and plasma-catalysis

1.3.1 Plasma-chemical reactions

In this section, we are going to review the main particle reaction in plasma to understand the process that takes place during plasma and plasma-catalytic processes. We will be focused on ionization, excitation and dissociation process, among all the possible reactions (**Figure 1.14**). A more extensive review of the plasma-chemical reactions can be found in the literature [27].

As explained previously, the electrical energy is initially transferred to the electrons. Then the generated high energetic electron interacts with other particles by elastic and inelastic collisions. For elastic collisions, the total kinetic energy is conserved. Due to the large difference of mass of the high energy electrons and atom/molecules, a very small quantity of kinetic energy is transferred between the species.

In the case of inelastic collision, part of kinetic energy is transferred to the internal energy. This process causes that the atom can be excited to a higher energy state, being excited or, if the transferred energy is sufficient, ionized or dissociated (molecules). Therefore, the different types of processes are ionization, excitation and dissociation that will depend on the electron energy.



Reaction		Equation
Ionization	Electron ionization	$e^- + A \rightarrow 2 \cdot e^- + A^+$
	Attachment	$e^- + A + B \rightarrow AB^-$
	Photoionisation	$h\nu + A \rightarrow e^- + A^+$
Excitation	Electronic	$e^- + A \rightarrow e^- + A^*$
	Vibrational	
	Rotational	
Dissociation	Electron dissociation	$e^- + AB \rightarrow e^- + A + B$
	Dissociative attachment	$e^- + AB \rightarrow 2 \cdot e^- + A + B^-$
	Dissociative recombination	$e^- + AB^- \rightarrow A + B$

Figure 1.14. Few examples of ionization, excitation, and dissociation processes.

These three processes can be produced by other reaction than direct electron collisions. For example, other ionization processes are: photoionization, stepwise ionization, ionization due to collision with heavy particle (atom-atom) or surface ionization. In the case of dissociation, alternative mechanisms are dissociative electron attachment, dissociative ionization, dissociative recombination or stepwise

dissociation with excited molecules (vibrational). As an example of the high amount of possible chemical reactions, R. Aerts et al. published an experimental and computational study of CO₂ splitting in DBD, where in the simulation was used 42 chemical species and 501 chemical reactions (electron impact reaction, ion-ion, ion-neutral and neutral-neutral reaction) [30].

Considering the main processes (ionization, excitation and dissociation), the fraction of energy transferred to the different processes will depend on the electron energy (electron temperatures). The distribution of energy transfer follows the following trends: rotational excitation is produced at low electron energies ($\ll 1\text{eV}$), while vibrational excitations are more important at intermediate electron temperature (1eV) and electronic excitation and ionization have more importance at higher electron temperature ($1>\text{eV}$).

The specific energy distribution will depend on the gas composition and the electron temperature will depend on the type of plasma. Therefore, some channels can be promoted depending on the plasma setups (**Figure 1.15**). In the case of DBD plasma, the main channel is electronic excitation, ionization and dissociation.

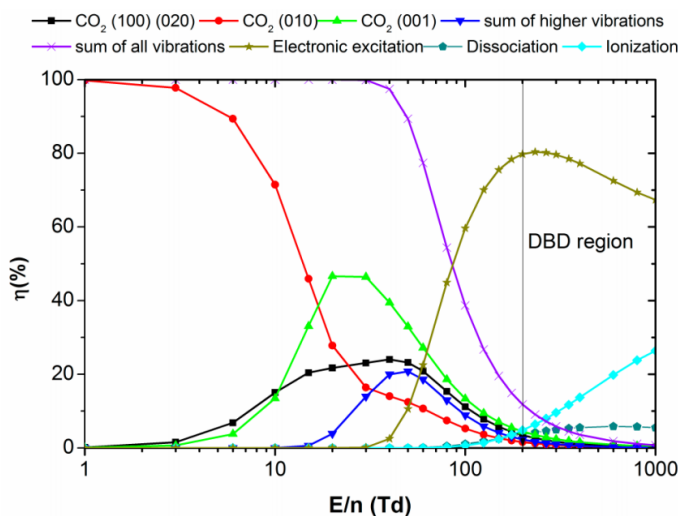


Figure 1.15. Fraction of energy transferred to the different processes. Adapted with permission from R. Aerts et al. [31]. Copyright © 2012, American Chemical Society.

1.3.2 Plasma-catalysis

The use of catalyst is needed to overcome the kinetic limitations of some reactions (**section 1.1.4**) and trigger the reaction to the desired products. The use of catalyst decreases the activation energy or energy barrier of the reaction, increasing the reaction rate. In a similar way, in a plasma-catalysis process, plasma excited species can be adsorbed in the catalyst, lowering the energy barrier compared with thermal-catalysis by increasing the energy of the reactants (**Figure 1.16**).

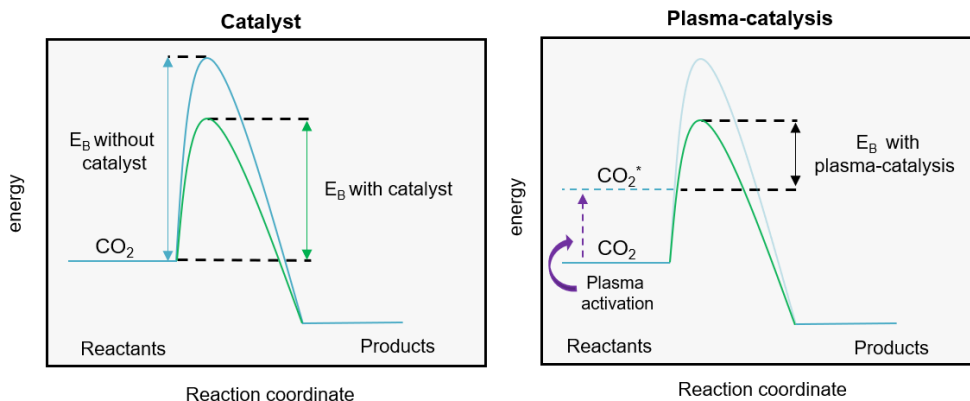


Figure 1.16. Energy barrier (E_b) without catalyst, with catalyst and with plasma-catalysis.

The combination of plasma and catalyst allows the different plasma species to interact with the catalyst and to be converted into specific products. Thus, by its combination (plasma-catalysis), better efficiencies, conversion and selectivity have been obtained in different applications.

The combination of plasma-catalysis can be done with two main different reactor configurations: in-plasma catalysis (IPC) and post-plasma catalysis configuration (PPC) [25]. In IPC, the catalyst is placed in the plasma region, while in PPC the catalyst is placed after the plasma region. The main advantage of IPC configurations is that the short lifetime species generated by the plasma can interact directly with the catalyst. While in PPC, the conditions of the catalyst bed could be independent of the plasma, despite only long-life species can interact with the catalyst. Moreover, in IPC as the plasma is generated directly in the catalyst, different effects may appear between plasma and catalysis.

In this regard, in addition to the catalytic behaviour of the different species generated by the plasma, there are other synergies between the catalyst and the plasma [32–34].

On the one hand, there are different effects of catalysts on plasma. One of the most important effects is the modification of the electric field. The presence of a catalyst in the plasma region can enhance the electric field at specific geometry points due to the polarization effect in dielectric packing materials. As a consequence of the electric modification, the electron energy distribution will be modified, changing the chemical composition of the plasma. In addition, the type of the plasma discharge can also be modified, changing from streamer type to surface discharge type over the packing material. The direct effect is an enhancement of the concentration of reactive species. Other effects are the formation of plasma discharge inside the catalyst pore and the species adsorption in the catalyst (changing gas composition).

On the other hand, there are effects of plasma on the catalyst. First, the plasma can produce changes in the physicochemical properties (higher adsorption and higher

surface area) and the reduction/oxidation state of the catalyst. Other important effects are the change in work function, the catalyst heating (100-150 °C) and supply of reactive species. In this aspect, plasma supplies new reactive species, which can create new reaction pathways and lower the activation barrier.

The combination of these effects can improve the final reaction performance. Thus, catalysts can be designed with properties that can trigger specific synergies that enhance reactivity.

1.4 State of the art

1.4.1 Catalyst for CO₂ methanation

As explained previously, the use of catalyst is needed to perform the reaction in thermochemical methanation. The catalyst is composed of the active phase, the support and the promotor. The active compounds are typically metals, such as Ru, Fe, Ni, Co and Mo, responsible for carrying out the reaction [35]. Between them, Ni and Ru based catalysts are the most common materials applied in thermal-catalysis due to their high activity and selectivity. For commercial applications, Ni stands out for the relatively low cost, allowing much higher metal-loadings, while it is restricted in the case of Ru [36,37].

The active phase could be used directly for the CO₂ methanation, as unsupported material, although typically active metals are supported in other materials [38]. Supports with higher surface area are required to increase the contact area between the active phase and the reactive gas. In addition, support gives structural and chemical stability to the catalyst. The most common supports are metal oxides such as Al₂O₃, TiO₂ and zeolites, with surface areas that can be higher than 200 m²·g⁻¹.

Finally, promotors are materials which added to the catalyst with the finality of increase the activity and stability. Despite the fact that the difference between support and promotor is sometimes difficult to discern; a promotor will have an important role in the reaction mechanism, but it is not intrinsically active, as the support. Recent studies showed that the incorporation of metal oxides, such as CeO₂, La₂O₃ and Y₂O₃ [39], or its use as porous support [40] improved the performance of Ni-based catalysts. Among them, a proper interaction between Ni and Ce plays an important role in the thermal catalytic route [41,42]. It is well-reported that the incorporation of Ce favours the CO₂ activation and the Ni metallic dispersion in thermal-catalysis [41,43]. In addition, the presence of Ce can change the reaction pathway due to the presence of moderate basic sites.

Regarding the reaction mechanism, two main mechanisms have been reported for CO₂ hydrogenation: CO₂ associative and CO₂ dissociative mechanism [15]. In CO₂ associative, CO₂ and H₂ are initially associatively adsorbed, forming oxygenated intermediates. These intermediates, carbonates and formates, are subsequently hydrogenated, forming CH₄. In nickel catalysts, H₂ is typically adsorbed in Ni, while CO₂ could be adsorbed in the substrate (e.g., Ce/Zr) [42]. In addition, the active site is found at the interface between the metal and support. In dissociative methanation, CO₂ is directly dissociated to carbonyl (CO intermediates), which is subsequential hydrogenated. In a similar way to the associative mechanism, the H₂ is initially adsorbed in the metal particle, as H_{ad} adatom, while CO₂ can be adsorbed in the support, as carbonyl, and in the Ni surface.

From the reaction pathways, it is clear that the promotors or substrate can contribute to the reaction mechanism, as the adsorption of CO₂ or the adsorption of CO₂ as

carbonyl. Thus, mechanisms depend on catalysts and reaction conditions (pressure, temperature, H_2/CO_2 ratio).

1.4.2 Plasma CO_2 conversion

The conversion of CO_2 into value-added products by plasma activation has been studied during the last decade [20,44–47]. Specifically, plasma technologies have been applied in CO_2 splitting [30,48,49], dry reforming of methane [21,50–52], hydrogenation to methanol or ethanol [53–57] and CO_2 hydrogenation to CH_4 [58–64].

Regarding the plasma CO_2 methanation, studies have been mainly focused on DBD setups due to the possibility to use catalysts in plasma-catalysis approach. Few studies have also been done with other setups, such as corona [65].

Following the trends of thermal methanation, Ni and Ru based catalysts have been reported [59,66], supported mainly over Al_2O_3 , Zr-Ce or zeolite [67]. Other works have also been reported Cu, Mn and Cu-Mn catalyst [68]. Ni has been found to be as active in plasma-catalytic CO_2 methanation than in thermal-catalysis (following similar behaviour than thermal methanation). The effect of support and promotor has been less studied compared with thermal-catalysis literature.

In general, experimental data showed an increase in activity at low temperatures by the effect of plasma. E. Jwa et al. studied Ni-Zeolite catalyst with plasma in a controlled temperature range of 180-360 °C [59]. They observed a displacement of the activity to lower temperature when the reaction was assisted by plasma (from 360 °C to 260 °C). They stated that the main effect of plasma-assisted methanation was the reduction of the working temperature due to the plasma activation of CO_2 . Lately, M.Nizio et al. studied Ni-Zr/Ce catalyst with plasma in a temperature range between 80-450 °C (externally heating)[61]. They also found that plasma enhances the reaction at lower temperatures (conversion increased from 0 to 97% at a temperature lower than 260 °C) while the effect at higher temperature was not relevant.

Other studies have worked in plasma methanation without any heating system [62,67]. In this works, reactor reached a temperature between 100-200 °C due to the heat released by the plasma and the methanation reaction. Under these conditions, working temperatures as low as 110 °C were obtained using Ni-Ce/Zr catalyst activated by plasma [67].

Overall, few studies have deeply investigated catalyst composition and promotor effect or analyzed the energy efficiency compared with thermal processes. In this thesis, we will investigate Ni-based catalysts and improve DBD reactors, focusing on the energy efficiency.

1.5. Aim of the thesis

This thesis is focused on the CO₂ methanation in a DBD plasma reactor. The main objectives are:

- Develop a DBD reactor for the CO₂ conversion to CH₄.
- Synthesize and optimize Ni-based catalyst for plasma CO₂ methanation.
- Study the differences between plasma and thermal methanation.
- Study the energy efficiency and energy cost of the plasma methanation reaction and compare it with thermal methanation.
- Develop and optimize novel reactor configuration to reduce the energy cost.

In order to achieve these objectives, this thesis is structured as described below:

- **Chapter 2** presents the DBD reactor, the reactor setup, experimental methodology and the main catalyst synthesis.

Part I. Catalyst for plasma CO₂ methanation.

- **Chapter 3** presents the DBD reactor validation and the catalytic evaluation of Ni-zeolite based catalyst.
- **Chapter 4** presents the catalytic evaluation of Ni-Ce catalyst synthesized by one-pot synthesis. The chapter is focused on the role of Ce in Ni-Ce catalyst.

Part II. DBD reactor optimization.

- **Chapter 5** is focused on the adiabatic and pseudo-adiabatic configurations. The synergies in adiabatic configuration are shown.
- **Chapter 6** presents a hybrid plasma-catalytic where the role of plasma is to ignite the reaction that can be self-sustained in autothermal conditions.

Finally, the main conclusions are summarized in **Chapter 7**. In addition, **Appendixes** are included with additional experimental data and results of each chapter.

1.6. References

- [1] IPCC, 2021: Climate Change 2021: The Physical Science Basis. Contribution of Working Group I to the Sixth Assessment Report of the Intergovernmental Panel on Climate Change [Masson-Delmotte, V., P. Zhai, A. Pirani, S. L. Connors, C. Péan, S. Berger, N. Ca.
- [2] A. Edo, E. Hertwich, N. Heeren, Emissions Gap Report 2019, 2019. <http://www.unenvironment.org/emissionsgap>.
- [3] IPCC, 2014: Climate Change 2014: Synthesis Report. Contribution of Working Groups I, II and III to the Fifth Assessment Report of the Intergovernmental Panel on Climate Change [Core Writing Team, R.K. Pachauri and L.A. Meyer (eds.)]. IPCC, Geneva, Switzer.
- [4] UNFCCC. Adoption of the paris agreement. 2015. https://unfccc.int/sites/default/files/english_paris_agreement.pdf .
- [5] H. Ritchie, M. Roser, CO₂ and other greenhouse gas emissions, Our World Data. (2017). <https://ourworldindata.org/co2-and-other-greenhouse-gas-emissions#>, .
- [6] IPCC (2021): Summary for Policymakers of the Working Group I Contribution to the IPCC Sixth Assessment Report. NERC EDS Centre for Environmental Data Analysis, date of citation.
- [7] A.D.N. Kamkeng, M. Wang, J. Hu, W. Du, F. Qian, Transformation technologies for CO₂ utilisation: Current status, challenges and future prospects, Chem. Eng. J. 409 (2021) 128138. doi:10.1016/j.cej.2020.128138.
- [8] J.R. Morante, T. Andreu, G. García, J. Guilera, A. Tarancon, M. Torrell, Hidrógeno. Vector energético de una economía descarbonizada, Fundación Naturgy, 2020.
- [9] G. Centi, S. Perathoner, Opportunities and prospects in the chemical recycling of carbon dioxide to fuels, Catal. Today. 148 (2009) 191–205. doi:10.1016/j.cattod.2009.07.075.
- [10] P. Capros, A. De Vita, N. Tasios, P. Siskos, M. Kannavou, A. Petropoulos, S. Evangelopoulou, M. Zampara, D. Papadopoulos, C. Nakos, EU Reference Scenario 2016: Energy, Transport and GHG Emissions—Trends to 2050, 2016. doi:10.2833/9127.
- [11] M. Götz, J. Lefebvre, F. Mörs, A. McDaniel Koch, F. Graf, S. Bajohr, R. Reimert, T. Kolb, Renewable Power-to-Gas: A technological and economic review, Renew. Energy. 85 (2016) 1371–1390. doi:10.1016/j.renene.2015.07.066.
- [12] S. Rönsch, J. Schneider, S. Matthischke, M. Schlüter, M. Götz, J. Lefebvre, P. Prabhakaran, S. Bajohr, Review on methanation – From fundamentals to current projects, Fuel. 166 (2016) 276–296. doi:10.1016/j.fuel.2015.10.111.
- [13] M. Bailera, P. Lisbona, L.M. Romeo, S. Espatolero, Power to Gas projects review: Lab, pilot and demo plants for storing renewable energy and CO₂, Renew. Sustain. Energy Rev. 69 (2017) 292–312. doi:10.1016/j.rser.2016.11.130.
- [14] K. Ghaib, K. Nitz, F.-Z. Ben-Fares, Chemical Methanation of CO₂: A Review, ChemBioEng Rev. 3 (2016) 266–275. doi:10.1002/cben.201600022.
- [15] B. Miao, S.S.K. Ma, X. Wang, H. Su, S.H. Chan, Catalysis mechanisms of CO₂ and CO methanation, Catal. Sci. Technol. 6 (2016) 4048–4058. doi:10.1039/C6CY00478D.

- [16] E. Moioli, N. Gallandat, A. Züttel, Model based determination of the optimal reactor concept for Sabatier reaction in small-scale applications over Ru/Al₂O₃, *Chem. Eng. J.* 375 (2019) 121954. doi:10.1016/j.cej.2019.121954.
- [17] J. Bremer, K. Sundmacher, Operation range extension via hot-spot control for catalytic CO₂ methanation reactors, *React. Chem. Eng.* 4 (2019) 1019–1037. doi:10.1039/C9RE00147F.
- [18] F. Kosaka, T. Yamaguchi, Y. Ando, T. Mochizuki, H. Takagi, K. Matsuoka, K. Kuramoto, Thermal management of CO₂ methanation with axial staging of active metal concentration in Ni-YSZ tubular catalysts, *Int. J. Hydrogen Energy.* 46 (2021) 4116–4125. doi:10.1016/j.ijhydene.2020.10.247.
- [19] A. Alarcón, J. Guilera, T. Andreu, An insight into the heat-management for the CO₂ methanation based on free convection, *Fuel Process. Technol.* 213 (2021) 106666. doi:10.1016/j.fuproc.2020.106666.
- [20] R. Snoeckx, A. Bogaerts, Plasma technology – a novel solution for CO₂ conversion?, *Chem. Soc. Rev.* 46 (2017) 5805–5863. doi:10.1039/C6CS00066E.
- [21] P. Mehta, P. Barboun, D.B. Go, J.C. Hicks, W.F. Schneider, Catalysis Enabled by Plasma Activation of Strong Chemical Bonds: A Review, *ACS Energy Lett.* 4 (2019) 1115–1133. doi:10.1021/acseenergylett.9b00263.
- [22] P.K. Chu, X. Lu, eds., *Low Temperature Plasma Technology*, CRC Press, 2013. doi:10.1201/b15153.
- [23] R.A. Wolf, *Atmospheric Pressure Plasma for Surface Modification*, John Wiley & Sons, Inc., Hoboken, NJ, USA, 2012. doi:10.1002/9781118547519.
- [24] A. Bogaerts, E. Neyts, R. Gijbels, J. van der Mullen, Gas discharge plasmas and their applications, *Spectrochim. Acta Part B At. Spectrosc.* 57 (2002) 609–658. doi:10.1016/S0584-8547(01)00406-2.
- [25] S. Nijdam, E. van Veldhuizen, P. Bruggeman, U. Ebert, *Plasma Chemistry and Catalysis in Gases and Liquids*, 2012. doi:10.1002/9783527649525.
- [26] J. Loureiro, J. Amorim, *Kinetics and Spectroscopy of Low Temperature Plasmas*, Springer International Publishing, Cham, 2016. doi:10.1007/978-3-319-09253-9.
- [27] A. Fridman, *Plasma Chemistry*, Cambridge University Press, Cambridge, 2008. doi:10.1017/CBO9780511546075.
- [28] U. Kogelschatz, Dielectric-Barrier Discharges: Their History, Discharge Physics, and Industrial Applications, *Plasma Chem. Plasma Process.* 23 (2003) 1–46. doi:10.1023/A:1022470901385.
- [29] R. Brandenburg, Dielectric barrier discharges: progress on plasma sources and on the understanding of regimes and single filaments, *Plasma Sources Sci. Technol.* 26 (2017) 053001. doi:10.1088/1361-6595/aa6426.
- [30] R. Aerts, W. Somers, A. Bogaerts, Carbon Dioxide Splitting in a Dielectric Barrier Discharge Plasma: A Combined Experimental and Computational Study, *ChemSusChem.* 8 (2015) 702–716. doi:10.1002/cssc.201402818.
- [31] R. Aerts, T. Martens, A. Bogaerts, Influence of vibrational states on CO₂ splitting by dielectric barrier discharges, *J. Phys. Chem. C.* 116 (2012) 23257–23273. doi:10.1021/jp307525t.

- [32] H.H. Kim, Y. Teramoto, N. Negishi, A. Ogata, A multidisciplinary approach to understand the interactions of nonthermal plasma and catalyst: A review, *Catal. Today*. 256 (2014) 13–22. doi:10.1016/j.cattod.2015.04.009.
- [33] E.C. Neyts, A. Bogaerts, Understanding plasma catalysis through modelling and simulation—a review, *J. Phys. D. Appl. Phys.* 47 (2014) 224010. doi:10.1088/0022-3727/47/22/224010.
- [34] E.C. Neyts, K. Ostrikov, M.K. Sunkara, A. Bogaerts, Plasma Catalysis: Synergistic Effects at the Nanoscale, *Chem. Rev.* 115 (2015) 13408–13446. doi:10.1021/acs.chemrev.5b00362.
- [35] S. Rönsch, J. Schneider, S. Matthischke, M. Schlüter, M. Götz, J. Lefebvre, P. Prabhakaran, S. Bajohr, Review on methanation - From fundamentals to current projects, *Fuel*. 166 (2016) 276–296. doi:10.1016/j.fuel.2015.10.111.
- [36] E.Z. Golosman, V.N. Efremov, Industrial catalysts for the hydrogenation of carbon oxides, *Catal. Ind.* 4 (2012) 267–283. doi:10.1134/S2070050412040071.
- [37] G. Garbarino, P. Riani, L. Magistri, G. Busca, A study of the methanation of carbon dioxide on Ni/Al₂O₃ catalysts at atmospheric pressure, *Int. J. Hydrogen Energy*. 39 (2014) 11557–11565. doi:10.1016/j.ijhydene.2014.05.111.
- [38] P. Frontera, A. Macario, M. Ferraro, P. Antonucci, Supported Catalysts for CO₂ Methanation: A Review, *Catalysts*. 7 (2017) 59. doi:10.3390/catal7020059.
- [39] H. Muroyama, Y. Tsuda, T. Asakoshi, H. Masitah, T. Okanishi, T. Matsui, K. Eguchi, Carbon dioxide methanation over Ni catalysts supported on various metal oxides, *J. Catal.* 343 (2016) 178–184. doi:10.1016/j.jcat.2016.07.018.
- [40] L. Atzori, M.G. Cutrufello, D. Meloni, C. Cannas, D. Gazzoli, R. Monaci, M.F. Sini, E. Rombi, Highly active NiO-CeO₂ catalysts for synthetic natural gas production by CO₂ methanation, *Catal. Today*. 299 (2018) 183–192. doi:10.1016/j.cattod.2017.05.065.
- [41] S. Tada, T. Shimizu, H. Kameyama, T. Haneda, R. Kikuchi, Ni/CeO₂ catalysts with high CO₂ methanation activity and high CH₄ selectivity at low temperatures, *Int. J. Hydrogen Energy*. 37 (2012) 5527–5531. doi:10.1016/j.ijhydene.2011.12.122.
- [42] P.A.U. Aldana, F. Ocampo, K. Kobl, B. Louis, F. Thibault-Starzyk, M. Daturi, P. Bazin, S. Thomas, A.C. Roger, Catalytic CO₂ valorization into CH₄ on Ni-based ceria-zirconia. Reaction mechanism by operando IR spectroscopy, *Catal. Today*. 215 (2013) 201–207. doi:10.1016/j.cattod.2013.02.019.
- [43] A. Westermann, B. Azambre, M.C. Bacariza, I. Graça, M.F. Ribeiro, J.M. Lopes, C. Henriques, Insight into CO₂ methanation mechanism over NiUSY zeolites: An operando IR study, *Appl. Catal. B Environ.* 174–175 (2015) 120–125. doi:10.1016/j.apcatb.2015.02.026.
- [44] A. Bogaerts, A. Berthelot, S. Heijkers, S. Kolev, R. Snoeckx, S. Sun, G. Trenchev, K. Van Laer, W. Wang, CO₂ conversion by plasma technology: Insights from modeling the plasma chemistry and plasma reactor design, *Plasma Sources Sci. Technol.* 26 (2017). doi:10.1088/1361-6595/aa6ada.
- [45] S. Xu, H. Chen, C. Hardacre, X. Fan, Non-thermal plasma catalysis for CO₂ conversion and catalyst design for the process, *J. Phys. D. Appl. Phys.* 54 (2021) 233001. doi:10.1088/1361-6463/abe9e1.

- [46] V. Palma, M. Cortese, S. Renda, C. Ruocco, M. Martino, E. Meloni, A review about the recent advances in selected nonthermal plasma assisted solid–gas phase chemical processes, *Nanomaterials*. 10 (2020) 1–56. doi:10.3390/nano10081596.
- [47] H. Chen, Y. Mu, S. Xu, S. Xu, C. Hardacre, X. Fan, Recent advances in non-thermal plasma (NTP) catalysis towards C1 chemistry, *Chinese J. Chem. Eng.* 28 (2020) 2010–2021. doi:10.1016/j.cjche.2020.05.027.
- [48] A. Lebouvier, S.A. Iwarere, P. D’Argenlieu, D. Ramjugernath, L. Fulcheri, Assessment of carbon dioxide dissociation as a new route for syngas production: A comparative review and potential of plasma-based technologies, *Energy and Fuels*. 27 (2013) 2712–2722. doi:10.1021/ef301991d.
- [49] P. Chen, J. Shen, T. Ran, T. Yang, Y. Yin, Investigation of operating parameters on CO₂ splitting by dielectric barrier discharge plasma, *Plasma Sci. Technol.* 19 (2017). doi:10.1088/2058-6272/aa8903.
- [50] A.H. Khoja, M. Tahir, N.A.S. Amin, Recent developments in non-thermal catalytic DBD plasma reactor for dry reforming of methane, *Energy Convers. Manag.* 183 (2019) 529–560. doi:10.1016/j.enconman.2018.12.112.
- [51] J.A. Andersen, J.M. Christensen, M. Østberg, A. Bogaerts, A.D. Jensen, Plasma-catalytic dry reforming of methane: Screening of catalytic materials in a coaxial packed-bed DBD reactor, *Chem. Eng. J.* 397 (2020) 125519. doi:10.1016/j.cej.2020.125519.
- [52] W.C. Chung, M.B. Chang, CO₂ Reforming with CH₄ via Plasma Catalysis System, in: *Carbon Dioxide Chem. Capture Oil Recover.*, InTech, 2018. doi:10.5772/intechopen.73579.
- [53] D. Li, V. Rohani, F. Fabry, A. Parakkulam Ramaswamy, M. Sennour, L. Fulcheri, Direct conversion of CO₂ and CH₄ into liquid chemicals by plasma-catalysis, *Appl. Catal. B Environ.* 261 (2020) 2–9. doi:10.1016/j.apcatb.2019.118228.
- [54] R. Snoeckx, W. Wang, X. Zhang, M.S. Cha, A. Bogaerts, Plasma-based multi-reforming for Gas-To-Liquid: tuning the plasma chemistry towards methanol, *Sci. Rep.* 8 (2018) 15929. doi:10.1038/s41598-018-34359-x.
- [55] L. Wang, Y. Yi, H. Guo, X. Tu, Atmospheric Pressure and Room Temperature Synthesis of Methanol through Plasma-Catalytic Hydrogenation of CO₂, *ACS Catal.* 8 (2018) 90–100. doi:10.1021/acscatal.7b02733.
- [56] B. Zhao, Y. Liu, Z. Zhu, H. Guo, X. Ma, Highly selective conversion of CO₂ into ethanol on Cu/ZnO/Al₂O₃ catalyst with the assistance of plasma, *J. CO₂ Util.* 24 (2018) 34–39. doi:10.1016/j.jcou.2017.10.013.
- [57] P. Chawdhury, D. Kumar, C. Subrahmanyam, NTP reactor for a single stage methane conversion to methanol: Influence of catalyst addition and effect of promoters, *Chem. Eng. J.* 372 (2019) 638–647. doi:10.1016/j.cej.2019.04.172.
- [58] R. Dębek, F. Azzolina-Jury, A. Travert, F. Maugé, A review on plasma-catalytic methanation of carbon dioxide – Looking for an efficient catalyst, *Renew. Sustain. Energy Rev.* 116 (2019). doi:10.1016/j.rser.2019.109427.
- [59] E. Jwa, S.B. Lee, H.W. Lee, Y.S. Mok, Plasma-assisted catalytic methanation of CO and CO₂ over Ni-zeolite catalysts, *Fuel Process. Technol.* 108 (2013) 89–93. doi:10.1016/j.fuproc.2012.03.008.

- [60] E.Y. Mora, A. Sarmiento, E. Vera, Alumina and quartz as dielectrics in a dielectric barrier discharges DBD system for CO₂ hydrogenation, *J. Phys. Conf. Ser.* 687 (2016) 012020. doi:10.1088/1742-6596/687/1/012020.
- [61] M. Nizio, A. Albarazi, S. Cavadias, J. Amouroux, M.E. Galvez, P. Da Costa, Hybrid plasma-catalytic methanation of CO₂ at low temperature over ceria zirconia supported Ni catalysts, *Int. J. Hydrogen Energy.* 41 (2016) 11584–11592. doi:10.1016/j.ijhydene.2016.02.020.
- [62] R. Benrabbah, C. Cavaniol, H. Liu, S. Ognier, S. Cavadias, M.E. Gálvez, P. Da Costa, Plasma DBD activated ceria-zirconia-promoted Ni-catalysts for plasma catalytic CO₂ hydrogenation at low temperature, *Catal. Commun.* 89 (2017) 73–76. doi:10.1016/j.catcom.2016.10.028.
- [63] M. Mikhail, B. Wang, R. Jalain, S. Cavadias, M. Tatoulian, S. Ognier, M.E. Gálvez, P. Da Costa, Plasma-catalytic hybrid process for CO₂ methanation: optimization of operation parameters, *React. Kinet. Mech. Catal.* 8247 (2018). doi:10.1007/s11144-018-1508-8.
- [64] R. Dębek, F. Azzolina-Jury, A. Travert, F. Maugé, F. Thibault-Starzyk, Low-pressure glow discharge plasma-assisted catalytic CO₂ hydrogenation—The effect of metal oxide support on the performance of the Ni-based catalyst, *Catal. Today.* (2019) 1–13. doi:10.1016/j.cattod.2019.03.039.
- [65] W.F.L.M. Hoeben, E.J.M. van Heesch, F.J.C.M. Beckers, W. Boekhoven, A.J.M. Pemen, Plasma-Driven Water Assisted CO₂ Methanation, *IEEE Trans. Plasma Sci.* 43 (2015) 1954–1958. doi:10.1109/TPS.2015.2429316.
- [66] W. XU, X. ZHANG, M. DONG, J. ZHAO, L. DI, Plasma-assisted Ru/Zr-MOF catalyst for hydrogenation of CO₂ to methane, *Plasma Sci. Technol.* 21 (2019) 044004. doi:10.1088/2058-6272/aaf9d2.
- [67] M. Nizio, R. Benrabbah, M. Krzak, R. Debek, M. Motak, S. Cavadias, M.E. Gálvez, P. Da Costa, Low temperature hybrid plasma-catalytic methanation over Ni-Ce-Zr hydrotalcite-derived catalysts, *Catal. Commun.* 83 (2016) 14–17. doi:10.1016/j.catcom.2016.04.023.
- [68] Y. Zeng, X. Tu, S. Member, Plasma-Catalytic CO₂ Hydrogenation at Low Temperatures, 44 (2015) 1–7.

Chapter 2

DBD reactor setup and experimental methodology

This chapter has been mainly written for the thesis, which also includes a summary of “Experimental and methodology” sections of the paper published during the thesis.

2.1 Introduction

In this chapter, the experimental setup, methodology and the catalyst synthesis are exposed. In **section 2.2**, a general overview of the experimental setup is shown. The different parts are further explained in next sections. DBD reactor geometry and the different reactor configurations used during the thesis are explained in **section 2.3**. A summary of the different reactor configurations used during the thesis can be found in the last **section 2.8**. Information regarding the electrical system (plasma generation and characterization) is explained in **section 2.4**. The analytical system used to quantify the conversion and selectivity is shown in **section 2.5**. The figures of merit used during this thesis (energy cost, energy efficiency, etc.) are defined in **section 2.6**. Finally, in **section 2.7**, the synthesis method of the used catalyst is described.

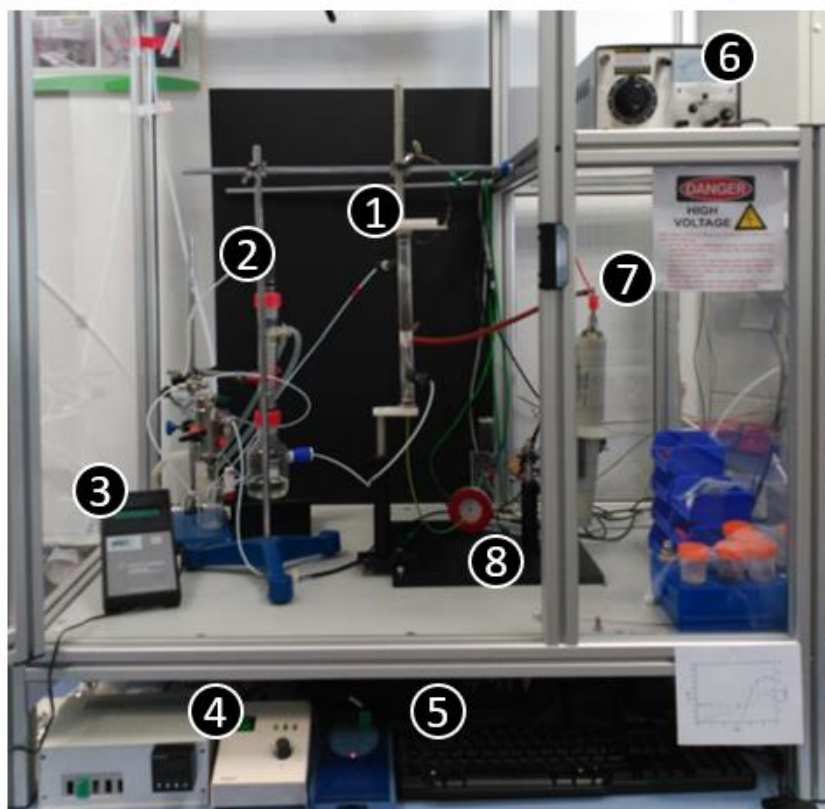
In addition, other equipments and characterization techniques were used during the thesis. Catalysts were analyzed by N₂ adsorption (BET surface area), CO₂ adsorption, X-ray diffraction (XRD), transmission electron microscopy (TEM), hydrogen temperature programmed reduction (H₂-TPR), thermogravimetric analysis (TGA-DSC), plasma elemental analysis (ICP) and Diffuse reflectance infrared Fourier transform spectroscopy (DRIFTS). The additional information of the equipment and characterization techniques are explained in **Appendix A.1**.

2.2 Experimental setup overview

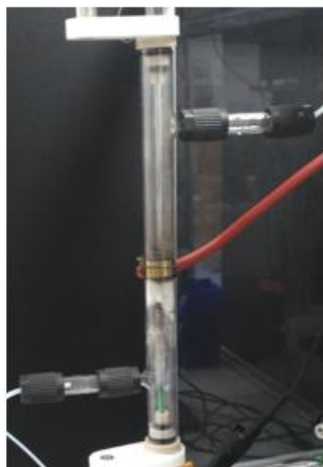
Plasma methanation setup was built for the purpose of this thesis in the framework of COSIN project (COMRD15-1-0037-01). A picture of the laboratory setup is shown in **Figure 2.1**. The setup is divided into 4 sections: DBD reactor, electrical system (power supply, oscilloscope, and probes), analytical system (gas chromatography) and other auxiliaries (gas bottle, mass flow controllers, flow meters, water condenser and heating system), illustrated in a general scheme in **Figure 2.2**.

The DBD-catalytic reactor is a coaxial packed-bed reactor made of quartz with a total length of 250 mm and effective plasma working region of 10 mm (**section 2.3**). The reactor was fed with different gases employing mass flow controllers (Bronkhorst). For the methanation experiment, a stoichiometric mixture of H₂/CO₂ = 4:1 was used. Different reactor configurations were used during the thesis (**section 2.3.1**). Plasma was generated with a high voltage power source, with an applied voltage between 4 and 10 kV_{pk} at 52 kHz (**section 2.4.1**). Plasma discharge was monitored in-situ, following the three main signals: applied voltage, current and transferred charge (**section 2.4.2**). The electrical system allowed to measure the plasma power and the energy efficiency. At the output of the reactor, once water was condensed using a gas-liquid separation process, the gases were analyzed with a gas micro chromatography to obtain the conversion and reaction selectivity (**section 2.5**). All the systems were put inside an enclosure to isolate HV components and gas extraction to avoid the concentration of an explosive atmosphere.

a)



b)



c)



Figure 2.1. a) General DBD plasma-catalytic setup: (1) DBD-catalytic reactor (2) Water condenser (3) Flowmeter (4) Temperature control and measurement (5) Oscilloscope and PC (6) Power supply (7) High voltage probe (8) Current probe. b) DBD-catalytic reactor. c) Plasma and catalyst bed.

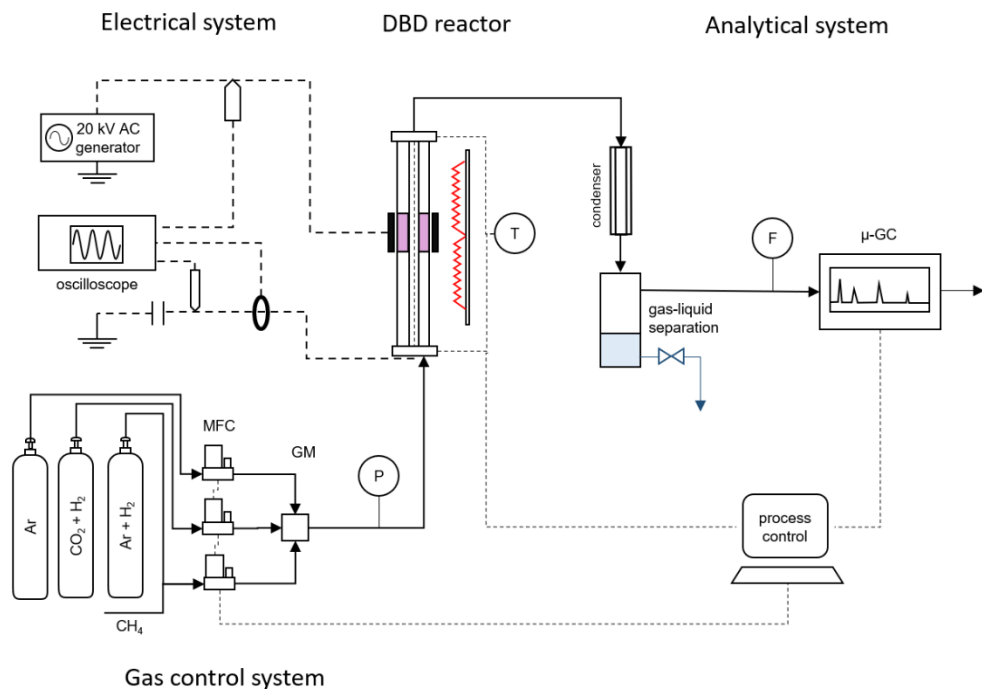


Figure 2.2. Scheme of the DBD plasma-catalytic setup.

2.3 DBD-catalytic reactor

For the construction of the DBD-catalytic reactor, a coaxial geometry was chosen due to its advantages in terms of ease of manufacture, assembly and ease to achieve good airtightness. **Figure 2.3** shows a general scheme of the DBD reactor. In this configuration, the reactor was made of two dielectric tubes with different diameters, while the electrodes were located around the outer tube and inside the inner tube. In that way, the plasma was generated in the space between the two tubes.

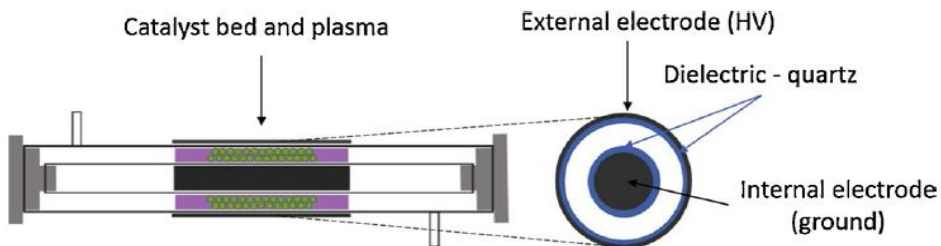


Figure 2.3. General scheme of the DBD reactor.

Regarding the dielectric material, quartz tubes with a thickness of one millimetre were selected. The dielectric strength of quartz and the selected thickness are enough to

withstand the electric field needed to produce the plasma ($25\text{-}40\text{ kV}\cdot\text{mm}^{-1}$). Thus, the outer tube diameter was fixed to 20 mm, while different tubes with diameters of 14, 15 and 16 mm were used for the inner tube. With these configurations, the GAP distance was 1, 1.5 or 2 mm, respectively (**Appendix A.2**).

Concerning the electrodes, initial tests were performed with different configurations, varying the length and shape of the electrode (**Figure 2.4**). In the final design, the electrode was made of rolled sheets of copper (**chapter 3** and **4**) and stainless-steel mesh (**chapter 5** and **6**) with a length of 10 mm. Finally, the catalyst is placed in the space between the electrodes and supported by quartz wool. In general, a total amount of 0.3 g of catalyst was used in the plasma zone. Only in **chapter 6**, a second catalytic bed of 0.6 g was added, which will be discussed in that chapter.

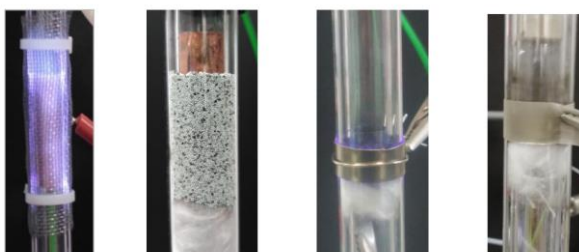


Figure 2.4. Different electrode configurations.

2.3.1 DBD reactor configuration: thermal, pseudo-adiabatic and adiabatic

All the methanation experiments performed during the thesis were done with three different reactor configurations, based on the DBD reactor explained in the previous section.

First, the DBD reactor was used for the conventional thermal methanation experiments to study the thermal activity of the catalyst (**Figure 2.5a**). For this configuration, the reactor was heated with an electrical heat rope, controlled with PID system, while the electrodes for the plasma generation were taken out. The temperature was measured at the catalytic bed with a thermocouple.

The two other configurations were used for plasma experiments, working with two different thermal management approaches (**Figure 2.5b** and **Figure 2.5c**). In these setups, no additional external heating was used. These types of DBD reactors without external heating were previously named adiabatic [1]. The reactor temperature was achieved due to the reaction and plasma heat without any external heating/cooling system, in a similar way that adiabatic reactors work in thermal methanation [2]. Despite this, previous works were unclear or did not distinguish if the reactor was thermally insulated or not. In order to differentiate, we defined pseudo-adiabatic configuration, where reactor is open to atmosphere and not thermally isolated (**Figure 2.5b** and **e**), while in adiabatic conditions, reactor is fully thermally insulated (**Figure**

2.5c and **f**). In the adiabatic configuration, the reactor is placed inside a metal box filled with granular insulator spheres (Liapor, expanded clay). In both configurations, the temperature was monitored with a thermocouple placed inside the reactor near the plasma zone (at <10 mm) or/and in contact with the external electrode.

Pseudo-adiabatic configuration was used for **chapters 3** and **4**, which are focused on catalyst optimization. The adiabatic configuration is presented in **chapters 5** and **6**, which are focused on reactor optimization.

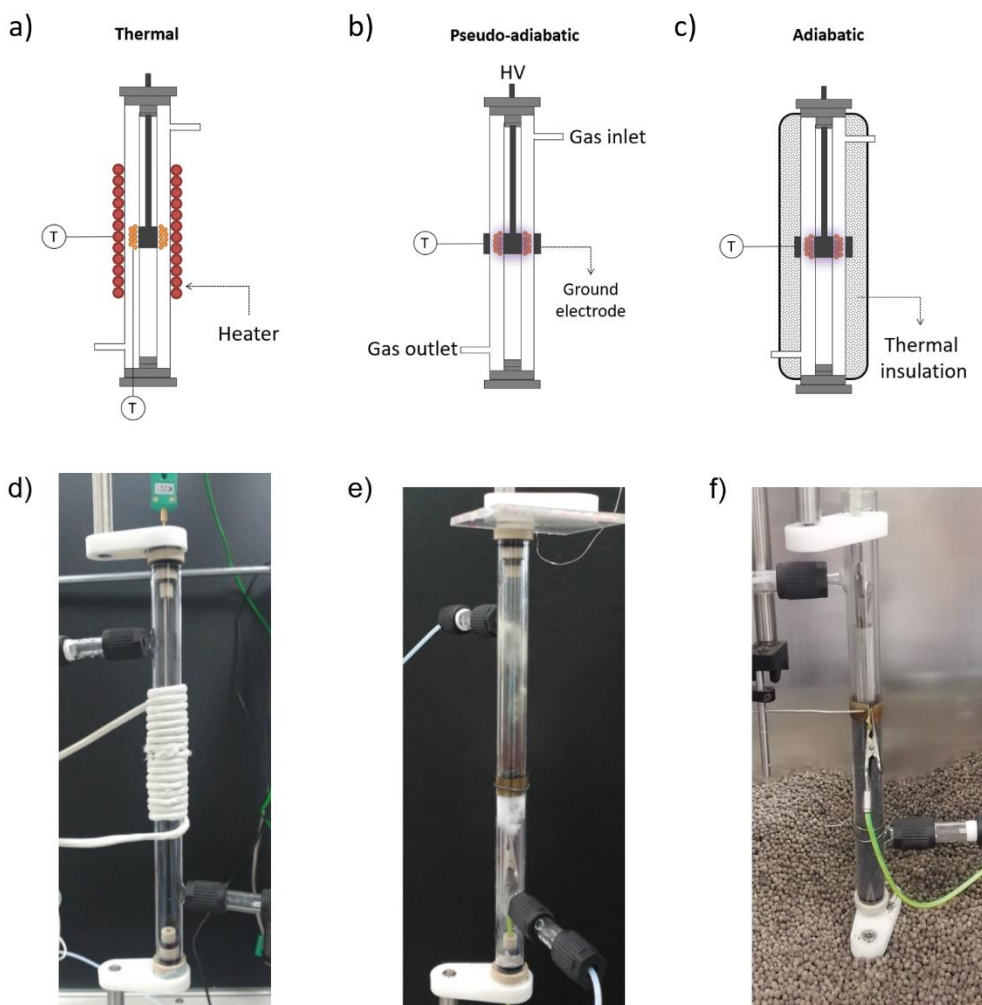


Figure 2.5. The three main reactor configurations. **a-d)** Thermal reactor **b-e)** Pseudo-adiabatic reactor **c-d)** Adiabatic reactor (reactor in the enclosure, being filled with insulating spheres).

2.4 Electrical system

2.4.1 Plasma power supply

The plasma generator consists in a high voltage power supply capable of generating an alternating current signal of the order of kilovolts. The breakdown voltage was expected to be around 4-6 kV. In terms of power, it was planned to work with powers lower than 100 W. The selected high voltage power supply (PVM500, Info Unlimited, U.S) to generate the plasma had the following characteristics:

- Maximum voltage: 15-30 kV_{pk-pk}
- Frequency: 20 kHz to 70 kHz
- Maximum power: 300 W

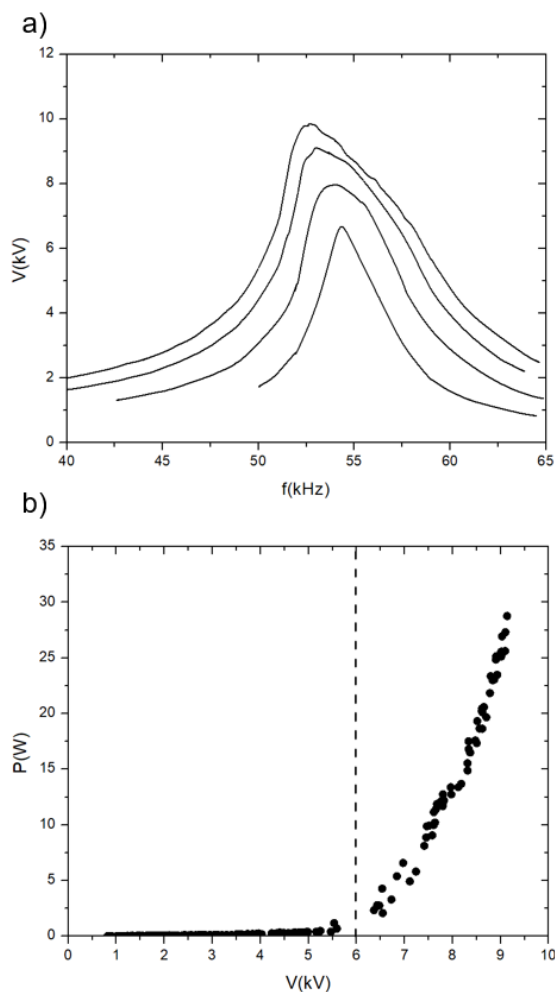


Figure 2.6. Voltage, frequency and power measurement in a DBD with CO₂/H₂ flow. **a)** Resonance frequency: voltages versus frequency. **b)** Breakdown voltage: power vs voltage ($V_b \sim 6$ kV_{pk}).

Although the power supply can generate HV signals with different frequencies, the power supply works at a constant frequency when operating with complex loads, as DBD. For complex load, the PVM500 should tune the applied frequency to the resonance point to obtain the maximum power source. At this point, the inductive reactance of the secondary coil of the power source is equal to the capacitive reactance of the reactor. Then, the power can be transferred efficiently to the resistive part of the load (plasma).

The resonance frequency depends on both the impedance of the DBD reactor and that of the generator. In our case, the resonance frequency was found to be between 52 and 54 kHz (**Figure 2.6a**). Near the resonance frequency, the voltage can easily increase up to the breakdown voltage where the plasma is ignited. As seen in **Figure 2.6b**, V_b is found near the 6 kV_{pk} in our configuration for CO₂/H₂ flow. Once the plasma is ignited, the applied voltage ranged between 6 kV_{pk} and 9 kV_{pk} for power between 1 and 30 W.

2.4.2 Electrical characterization

The electrical system consists of an oscilloscope and several electrical probes to measure in-situ all the electrical signals. The three main signals monitored for the full characterization were the applied high voltage, the current and the charge transferred (for the power measurement). The signals were measured simultaneously using a four-channel oscilloscope (PicoScope 5444A) with a sufficiently high bandwidth (200 MHz).

The scheme of the electrical system is shown in **Figure 2.7**. For the voltage measurement, it is required a probe capable of measuring a voltage of the order of kV and operating at high frequencies (kHz).

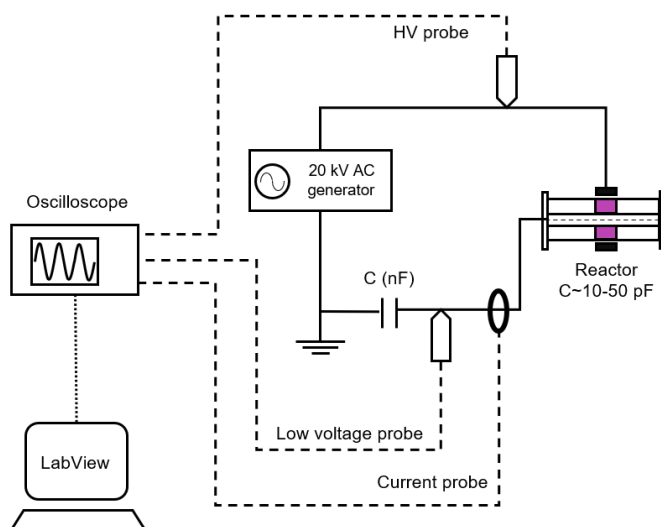


Figure 2.7. Electric scheme.

The instantaneous current was measured with a Rogowski coil probe. Rogowski probes usually have a limited bandwidth, which can have certain drawbacks. On the one hand, the probe will not be able to measure electrical micro-discharges correctly (in the order of 100 ns - GHz) if the upper limit is not high enough, and the micro-discharges will be attenuated and distorted. On the other hand, the lower limit may affect low-frequency components. In any case, these probes are sufficient to monitor the current signal qualitatively. The selected probe was CT-E1.02 Magnelab with has a bandwidth 200Hz and 500 MHz @ -3db.

Finally, the charge transferred was measured with an additional capacitor connected in series with the reactor. The charge transferred was used to measure the power with the Lissajous method.

Figure 2.8 shows the three signals measured for an applied AC voltage of 7 kV_{pk} and 52 kHz. In the instantaneous current signal, it can be observed the several spikes corresponding to the plasma micro-discharges.

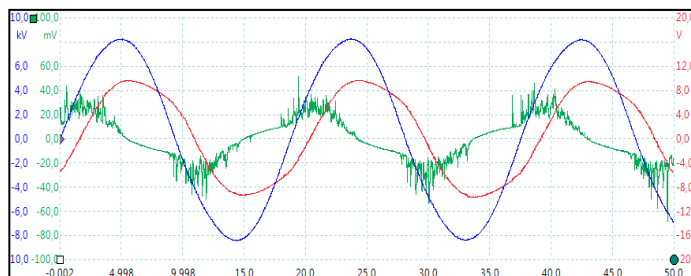


Figure 2.8. Example of signal (7 kV_{pk}): applied high voltage (blue), current (green) and the voltage across the monitoring capacitor (red).

2.4.3 Power measurement

In general applications, the power is measured using the momentary applied voltage and current signal (Eq. 2.1). However, in DBD this approach is not the preferred one, due to the current waveform. As seen in **Figure 2.8**, the current waveform is characterized by several spikes caused by the plasma micro-discharges. The plasma micro-discharges are generated in the range of ns. Thus, it is difficult to acquire the current signal with sufficient accuracy to measure the power. Even high-bandwidth and high-speed equipment have limitations to measure the power with the needed accuracy [3,4].

$$P_a = \frac{1}{T} \int_0^T V(t) \cdot I(t) \cdot dt \quad (2.1)$$

The alternative is the well-known Lissajous method, proposed by Manley in 1943 [5]. The Lissajous method consists of measuring the charge with an additional capacitor in series with the DBD reactor (red line in **Figure 2.8**). As the capacitor is positioned

in series, the current through the capacitor would be the same as the current through the DBD. The advantage of this method is that it is not necessary to use probes and oscilloscopes with large bandwidths, as the current can be measured by the charge stored in the capacitor (**Eq. 2.2**) with a low voltage probe. The value of the capacitor was chosen considering the theoretical value of the reactor's capacity (theoretically around 4-15 pF), so that it does not influence the generation of the plasma and without losing resolution (too large values).

$$Q(t) = C \cdot V_c(t) \quad (2.2)$$

The charge measured with the capacitor (**Eq. 2.2**) and the applied voltage is plot in the Q-V Lissajous plots (**Figure 2.9**). One can observe that the area from the Q-V Lissajous figure corresponds to the plasma power (**Eq. 2.3**).

Moreover, additional information could be obtained from the Q-V Lissajous figure, such as the reactor capacitance (C_d), the dielectric capacitance (C_r), the gap capacitance and the burning voltage [6]. The shape of the Q-V figure can also give additional information [7].

$$P_a = \frac{1}{T} \int_0^T V(t) \cdot I(t) \cdot dt = \frac{1}{T} \int_0^T V(t) \cdot dQ(t) \quad (2.3)$$

In order to measure in situ the power with the Lissajous method, we implemented a LabView program (**Appendix A.3**).

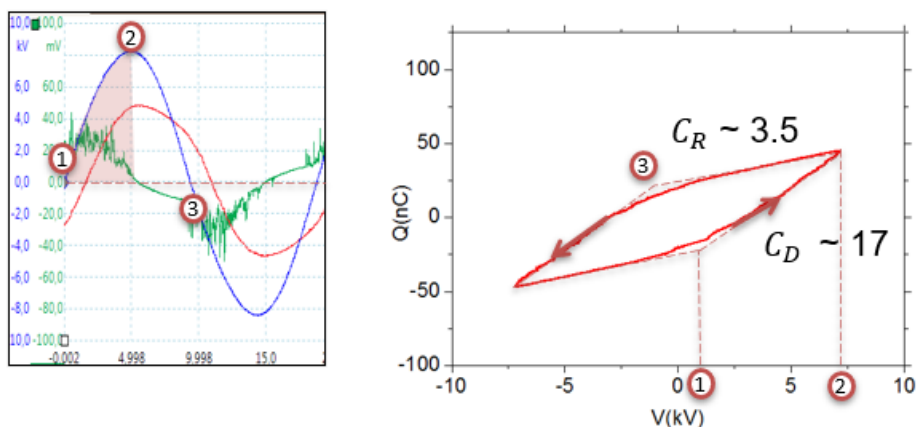


Figure 2.9. Lissajous figure (right):1-2 correspond to the discharge phase. 2-3 corresponds to the non-discharge phase.

2.5 Analytical system

In order to know the conversions and selectivity during the methanation experiments, the gas composition was analyzed at the output of the reactor. The gas analytical system consists of a micro gas chromatograph (uGC), Varian 490, equipped with 3

columns, each with a thermal conductivity detector (TCD). This system is able to quantify the concentration of H₂, CO₂, CO, CH₄, C₂H₄ and C₂H₆. The three columns configuration is:

- MolSieve 5A with backflush and argon as carrier gas. This configuration allows to quantify the concentration of H₂. In addition to detecting other gases such as CO and CH₄. The column oven is set to 80 °C and the injector temperature to 100 °C.
- MolSieve 5A with backflush and helium as carrier gas. This channel is specifically configured to quantify CO and CH₄. The column oven is set to 70 °C and the injector temperature to 100 °C.
- PoraPLOT Q with backflush and helium as carrier gas. It is configured to quantify CO₂, C₂H₄ and C₄H₆. The column oven is set to 60 °C and the injector temperature to 100 °C.

Each column was calibrated using several bottles of calibration mixtures in order to be able to work throughout all the concentrations range.

CO₂ conversion (X_{CO_2}), CH₄ selectivity (S_{CH_4}) and CH₄ yield (Y_{CH_4}) were calculated using the following equations:

$$X_{CO_2} = \frac{n_{CO_2 \text{ in}} - n_{CO_2 \text{ out}}}{n_{CO_2 \text{ in}}} \cdot 100 = \frac{Q_{in} \cdot [CO_2]_{in} - Q_{out} \cdot [CO_2]_{out}}{Q_{in} \cdot [CO_2]_{in}} \cdot 100 \quad (2.4)$$

$$S_{CH_4} = \frac{n_{CH_4 \text{ out}}}{n_{CH_4 \text{ out}} + n_{CO \text{ out}}} \cdot 100 = \frac{[CH_4]_{out}}{[CH_4]_{out} + [CO]_{out}} \cdot 100 \quad (2.5)$$

$$Y_{CH_4} = X_{CO_2} \cdot S_{CH_4} \quad (2.6)$$

where n_z is the number of mols for a given z gas, $[z]$ is the gas concentration, and Q is the gas flow. The gas flow at the output was measured with a volumetric flowmeter (ADM1000, Agilent) after water condensation.

2.6 Figures of merit

In plasma technologies, other key parameters apart from power are typically useful to compare different setups and technologies. Herein, three figures of merit have been considered: the specific energy input (SEI), the energy cost (EC) and the energy efficiency of the methanation reaction (η).

The SEI is defined as the plasma power (P) per inlet molar flow of the reactant mixture (F_{in}), in our case, the inlet CO₂/H₂ flow. Thus, the SEI can be calculated with **Eq. 2.7**.

$$SEI(kJ \cdot mol^{-1}) = \frac{P(kJ \cdot s^{-1})}{F_{in}(mol \cdot s^{-1})} \quad (2.7)$$

The EC is defined as the energy spent to produce one mole of CH₄ (n_{CH_4}), was calculated using the following equation (Eq. 2.8):

$$\text{EC (kJ} \cdot \text{mol}^{-1}) = \frac{E(\text{kJ})}{n_{\text{CH}_4}(\text{mol})} = \frac{P(\text{kJ} \cdot \text{s}^{-1})}{F_{\text{out}}(\text{mol} \cdot \text{s}^{-1}) \cdot [\text{CH}_4]_{\text{out}}} \quad (2.8)$$

where F_{out} is the total molar flow at the reactor output and $[\text{CH}_4]_{\text{out}}$ is the methane concentration.

The energy efficiency of the methanation reaction (η) was calculated as the ratio between the outlet energy in the form of methane and the overall energy input. The outlet energy was estimated only based on the low heating value (LHV) of produced methane ($801 \text{ kJ} \cdot \text{mol}^{-1}$) without considering the unreacted hydrogen at the outlet. As for the energy input, both the EC and the LHV of the converted hydrogen ($242 \text{ kJ} \cdot \text{mol}^{-1}$) were used.

$$\eta(\%) = \frac{E_{\text{out}}}{E_{\text{in}}} = \frac{\text{LHV}_{\text{CH}_4}(\text{kJ} \cdot \text{mol}^{-1}) \cdot n_{\text{CH}_4}}{\text{LHV}_{\text{H}_2}(\text{kJ} \cdot \text{mol}^{-1}) \cdot n_{\text{H}_2 \text{ conv}} + \text{EC}(\text{kJ} \cdot \text{mol}^{-1}) \cdot n_{\text{CH}_4}} \quad (2.9)$$

As it can be noticed, conservative assumptions were considered. In this sense, it was assumed that the heat available from methane as a fuel does not consider water condensation of the formed water, as this heat usually is not recovered. Besides, the highest η value that can be potentially achieved is lower than 100% in all exothermic reactions, because of the energy loss by the release of heat. Accordingly, the theoretical maximum efficiency of the methanation reaction was 83% when the power applied to the system is zero ($\text{EC} = 0$).

For comparison purposes, the maximum theoretical energy efficiency was calculated considering the minimum theoretical EC at each applied SEI:

$$\eta_{\text{max}}(\%) = \frac{E_{\text{out}}}{E_{\text{in}}} = \frac{\text{LHV}_{\text{CH}_4} \cdot n_{\text{CH}_4}}{\text{LHV}_{\text{H}_2} \cdot n_{\text{H}_2 \text{ conv}} + \text{EC}_{\text{min}} \cdot n_{\text{CH}_4}} \quad (2.10)$$

The minimum EC per mol of methane is obtained at the maximum methane yield (all CO₂ converted to CH₄):

$$\text{EC}_{\text{min}}(\text{kJ} \cdot \text{mol}^{-1}) = \frac{P(\text{kJ} \cdot \text{s}^{-1})}{n_{\text{CH}_4}^{\text{max}}} = \frac{P(\text{kJ} \cdot \text{s}^{-1})}{F_{\text{in}}(\text{mol} \cdot \text{s}^{-1}) \cdot [\text{CO}_2]_{\text{in}}} \quad (2.11)$$

2.7 Catalyst synthesis

Three different syntheses were used during the thesis to fabricate the catalysts for the CO₂ methanation. Ni was selected as the active material, as it has shown high activity and low price (see **chapter 1, section 1.4**), while Ce was chosen as the main promotor. The active material and promotor were impregnated into different support or synthesized together with the support. The syntheses used were:

- Ni-based catalyst impregnated in zeolite, used in **chapter 3**.
- Ni-Ce-Al synthesized with one-pot synthesis method, used in **chapter 4**.
- Ni-Ce impregnated on mesoporous alumina, used in **chapters 5 and 6**.

Before the experiments, catalysts were ex-situ reduced at 450 °C for 3 h under 5% H₂-Ar atmosphere (150 mL·min⁻¹).

2.7.1 Ni catalyst supported in zeolites

Ni supported on zeolite was prepared in the University of Lisbon by M.C. Bacariza. For this synthesis, commercial zeolite with different Si/Al ratios was used. The USY(3) zeolite was provided by Grace Davison and subsequently modified using an ion-exchange method (NH₄NO₃) to obtain H-USY(3) support. The H-USY(38) support was directly provided by Zeolyst. Both zeolites were ion-exchanged with a CsNO₃ solution obtaining the Cs-USY(3) and Cs-USY(38) zeolite support (**Table 2.1**).

Nickel, as the active element, was incorporated in the zeolites by using an incipient wetness impregnation method. The catalyst was dried at 80 °C overnight and calcinated at 500 °C for 6 h. In addition, Ni-Ce catalyst was obtained by co-impregnating 15 wt.% Ni and 20 wt.% Ce (**Table 2.1**).

Table 2.1. Summary of zeolites and impregnated catalyst.

Zeolites	Cs-USY(3) Cs-USY(38)
Impregnated catalysts	Ni/Cs-USY(3) Ni/Cs-USY(38) Ce-Ni/Cs-USY(38)

2.7.2 One-pot synthesis of Ni-Ce catalyst

Ni-Ce based catalysts on mesoporous alumina support (Ni-CeO₂/Al₂O₃) were synthesized by one-pot evaporation-induced self-assembly (EISA) method, following a similar procedure reported by other groups [8,9]. In the present case, both Ni and Ce were introduced together with alumina precursor. In all samples, Ni content was fixed at 15 wt.% while CeO₂ content was varied between 0 and 50 wt.% (0, 2, 10, 20, 30, 40, 50 wt.%).

A scheme of the EISA synthesis method is shown in **Figure 2.10**. In a typical synthesis, 1 g of (EO)₂₀(PO)₇₀(EO)₂₀ triblock copolymer (Pluronic P123, Sigma Aldrich) was dissolved in 20 mL of ethanol (Panreac, 96% v/v). Then, 3 mL of nitric acid (Labkem, 65%); and aluminium isopropoxide (Sigma Aldrich, 98%), nickel nitrate hexahydrate (Sigma Aldrich, 99%) and cerium nitrate hexahydrate (Merk, 99%) precursors were incorporated into the solution. The amount of precursor moles was adjusted to obtain the desired composition (as detailed in **Table 2.2**). The solution was stirred for 7 h and the solvents were slowly evaporated using a water-bath device at 60 °C for 48 h. The resulting green xerogel was air calcined at 450 °C for 5 h with a heating ramp of 0.5 °C·min⁻¹. The calcination temperature was initially optimized, trying different temperatures between 450 °C and 600 °C.

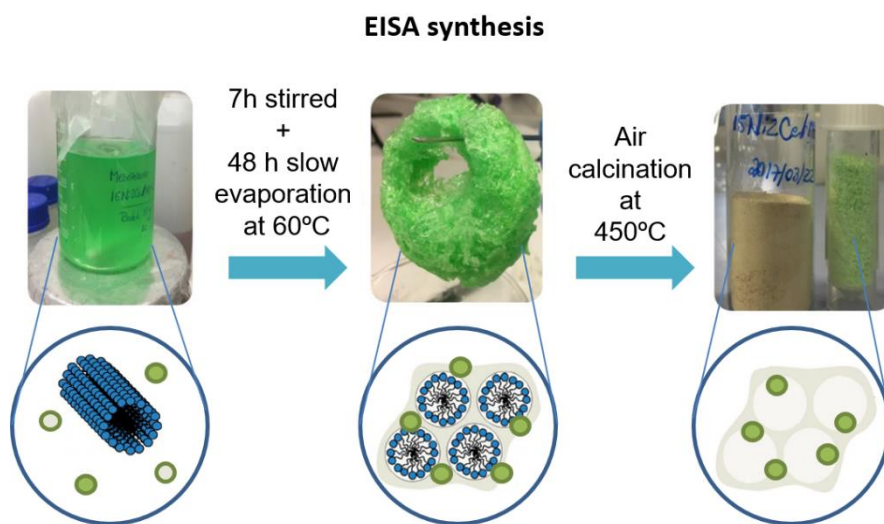


Figure 2.10. Main steps of EISA synthesis.

Table 2.2. Table of mmol used to synthesize the different catalysts with the EISA method.

Sample	Ni (wt.%)	Ni (mmol)	CeO ₂ (wt.%)	CeO ₂ (mmol)	Al ₂ O ₃ (wt.%)	Al ₂ O ₃ (mmol)
15Ni	15	2.56	0	0	85	8.34
2Ce-Ni	15	2.56	2	0.12	83	8.14
10Ce-Ni	15	2.56	10	0.58	75	7.36
20Ce-Ni	15	2.56	20	1.16	65	6.38
30Ce-Ni	15	2.56	30	1.74	55	5.39
40Ce-Ni	15	2.56	40	2.32	45	4.41
50Ce-Ni	15	2.56	50	2.90	35	3.43

2.7.3 Wet impregnation of Ni-Ce on commercial mesoporous alumina

Ni-CeO₂/Al₂O₃ catalyst was prepared by wet impregnation method of Ni-Ce in commercial mesoporous alumina support (Accu@spheres, Saint-Gobain Norpro, 400-500 μm).

In a typical synthesis, the γ-Al₂O₃ support was dried at 150 °C overnight to remove water. The Ni-Ce precursor solution was prepared, containing nickel nitrate hexahydrate (98% Alfa Aesar), cerium nitrate hexahydrate (99% Fluka) and water with a H₂O/Al₂O₃ ratio of 3. The γ-Al₂O₃ support was mixed with the precursor solution in a rotatory vacuum evaporator at 25 rpm and 25 °C for 1 h and slowly evaporated at 25 rpm, 80 °C and 0.8 bar for 6 h. Finally, the impregnated alumina was dried at 105 °C overnight and calcinated at 450 °C for 30 min with a 1 °C·min⁻¹ ramp. **Figure 2.11** shows a schematic of the wet impregnation synthesis.

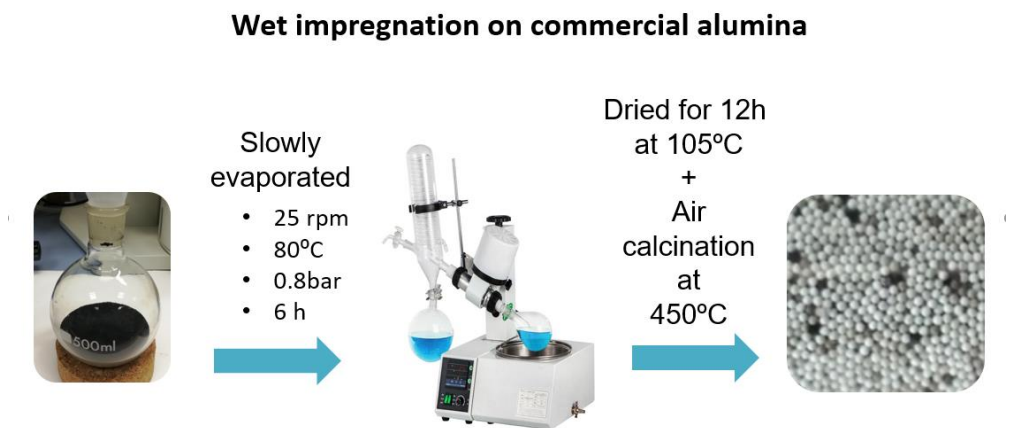


Figure 2.11. Main steps of impregnation on mesoporous alumina synthesis.

2.8 Summary

In this chapter, we have exposed the plasma DBD-catalytic reactor setup built during the thesis, and the methodology followed for the catalyst synthesis has been explained. The different reactor configurations, pseudo-adiabatic and adiabatic, have been defined.

In summary, **Table 2.3** shows the reactor configuration, electrode, GAP and catalyst used during the thesis. Chapters 3 and 4 are focused on the study of different catalysts (Ni-Ce Zeolite and Ni-Ce EISA). In these chapters, pseudo-adiabatic reactor with copper foil and 1.5 mm of GAP were used. Finally, the last two chapters (5 and 6) are focused on reactor optimization where adiabatic reactor is presented. In chapter 5 compares the adiabatic reactor with pseudo-adiabatic, while chapter 6 focuses on a novel use of DBD-plasma in an adiabatic configuration. Moreover, electrodes were changed to stainless steel (SS) mesh and GAP was increased up to 2 mm. The change in GAP was done during the thesis as reactor geometry optimization. The results of GAP optimization are found in **Appendix A.2**.

Table 2.3. Summary of experimental configurations used in the different chapters.

	Chapter 3	Chapter 4	Chapter 5	Chapter 6
Configuration	Pseudo-adiabatic	Pseudo-adiabatic	Pseudo and Adiabatic	Hybrid Adiabatic
Electrode	Copper foil	Copper foil	SS mesh	SS mesh
GAP	1.5	1.5	2.0	2.0
Catalyst	NiCe zeolites	NiCe EISA	NiCe WET	NiCe WET
g of catalyst	0.3 g	0.3 g	0.3g	0.3g+0.6g

2.9 References

- [1] M. Nizio, R. Benrabbah, M. Krzak, R. Debek, M. Motak, S. Cavadias, M.E. Gálvez, P. Da Costa, Low temperature hybrid plasma-catalytic methanation over Ni-Ce-Zr hydrotalcite-derived catalysts, *Catal. Commun.* 83 (2016) 14–17. doi:10.1016/j.catcom.2016.04.023.
- [2] S. Rönsch, J. Schneider, S. Matthischke, M. Schlüter, M. Götz, J. Lefebvre, P. Prabhakaran, S. Bajohr, Review on methanation – From fundamentals to current projects, *Fuel*. 166 (2016) 276–296. doi:10.1016/j.fuel.2015.10.111.
- [3] D. Ashpis, M. Laun, E. Griebeler, Progress toward Accurate Measurements of Power Consumption of DBD Plasma Actuators, in: 50th AIAA Aerosp. Sci. Meet. Incl. New Horizons Forum Aerosp. Expo., American Institute of Aeronautics and Astronautics, Reston, Virginia, 2012: pp. 1–24. doi:10.2514/6.2012-823.
- [4] M. Holub, On the measurement of plasma power in atmospheric pressure DBD plasma reactors, *Int. J. Appl. Electromagn. Mech.* 39 (2012) 81–87. doi:10.3233/JAE-2012-1446.
- [5] T.C. Manley, The Electric Characteristics of the Ozonator Discharge, *Trans. Electrochem. Soc.* 84 (1943) 83. doi:10.1149/1.3071556.
- [6] T. Butterworth, R. Elder, R. Allen, Effects of particle size on CO₂ reduction and discharge characteristics in a packed bed plasma reactor, *Chem. Eng. J.* 293 (2016) 55–67. doi:10.1016/j.cej.2016.02.047.
- [7] I. Biganzoli, R. Barni, a Gurioli, R. Pertile, C. Riccardi, Experimental investigation of Lissajous figure shapes in planar and surface dielectric barrier discharges, *J. Phys. Conf. Ser.* 550 (2014) 012039. doi:10.1088/1742-6596/550/1/012039.
- [8] L. Xu, H. Zhao, H. Song, L. Chou, Ordered mesoporous alumina supported nickel based catalysts for carbon dioxide reforming of methane, *Int. J. Hydrogen Energy*. 37 (2012) 7497–7511. doi:10.1016/j.ijhydene.2012.01.105.
- [9] K. Jabbour, P. Massiani, A. Davidson, S. Casale, N. El Hassan, Ordered mesoporous “one-pot” synthesized Ni-Mg(Ca)-Al₂O₃ as effective and remarkably stable catalysts for combined steam and dry reforming of methane (CSDRM), *Appl. Catal. B Environ.* 201 (2017) 527–542. doi:10.1016/j.apcatb.2016.08.009.

Part I.

Catalyst for plasma

CO₂ methanation

Chapter 3

Ni-Ce zeolite based catalyst

The results presented in chapter 3 have been mainly published in Journal of CO₂ Utilization as “*DBD plasma-assisted CO₂ methanation using zeolite-based catalysts: Structure composition-reactivity approach and effect of Ce as promoter*” by M.C. Bacariza¹, M. Biset-Peiró¹, I. Graça, J. Guilera, J. Morante, JM Lopes, T. Andreu, C. Henriques (J. CO₂ Util. 26, 202-211 (2018)). The published text and figures have been rewritten and edited for this chapter. More specifically, the results have been reordered and additional discussion and analyses have been added for the sake of clarity. As a remark, the thermal experiments showed in this chapter were done at IREC using the experimental setup shown in chapter 2, whereas the ones of the publication were done at IST (Instituto Superior Técnico) Universidade de Lisboa.

¹*These authors contributed equally to the manuscript.*

3.1 Introduction

This chapter is focused on the validation of the DBD reactor and the study of different catalysts for plasma methanation. All plasma experiments were done in pseudo-adiabatic conditions, without external heating or thermal insulation, as explained in **chapter 2**.

Two different sets of catalysts were used in this chapter: commercial catalyst and Ni based zeolite catalyst. The physicochemical characterization of the zeolite catalyst is shown in **section 3.2**.

Afterwards, the catalysts were tested in the DBD plasma reactor for the methanation reaction. First, the DBD plasma reactor was validated employing the commercial catalyst based on Ni-alumina (**section 3.3**). In addition, the effect of plasma in CO₂/H₂ gas mixtures with and without catalyst and catalyst performance was analyzed.

Once the reactor was validated, Ni-based zeolite catalysts were studied under plasma and thermal conditions (**section 3.4**). Zeolite based catalysts were previously studied by other groups [1–3]. Jwa et al. studied Ni-zeolite catalyst in plasma DBD reactor. The conversions were enhanced when plasma was used in a temperature range between 180-260 °C. The effect of plasma in the rate-determining step due to the reactive species was evaluated [1]. Azzolina-Jury and Thibault-Starzyk also studied Ni-zeolite under glow discharge plasma, proposing a mechanism for plasma CO₂ methanation in this system [2]. None of the previous publications studied the effect of zeolite structural composition. Thus, the present chapter explores the effect of zeolite structural composition under plasma. The effect of the Si/Al ratio in zeolite Ni-based catalyst was evaluated. In addition, the incorporation of Ce as a promotor was studied. Finally, the different factors that could significantly enhance the catalytic activity in thermal and plasma conditions were discussed in **section 3.5**.

In summary, the main objectives of this chapter are:

- Validate the effect of DBD plasma with and without catalyst.
- Determine the role of Si/Al ratio in Zeolite catalysts.
- Evaluate the incorporation of Ce as promotor in zeolite catalyst.
- Determine the key factors that determine the methanation reaction activated by plasma.

3.2 Catalyst for CO₂ methanation

Two different sets of catalysts were used in this chapter: commercial catalyst and Ni based zeolite. The commercial catalyst was provided by IBERCAT and was based on Ni/ γ -Al₂O₃.

Ni based zeolite catalysts were prepared at the University of Lisbon by M.C. Bacariza. Herein, the objective was to study the effect of Si/Al ratio and the Ce addition under plasma methanation. Two zeolites with a Si/Al ratio of 3 and 38 were used as catalyst support. Ni as the active element was incorporated in the zeolite by using an incipient wetness impregnation method (15 wt.% Ni). In addition, Ni-Ce catalyst was obtained by co-impregnating 15 wt.% of Ni and 20 wt.% of Ce. Additional information about catalyst synthesis has been explained in **chapter 2**. **Table 3.1** shows a summary of all zeolite catalysts used in this chapter.

Table 3.1. Summary of zeolite catalyst composition determined by ICP: Si/Al ratio and metal content.

Sample	Si/Al global	Si/Al framework	wt.%Ni	wt.%Ce	wt.%Cs
Cs-USY(3)	3	4	-	-	14
Ni/Cs-USY(3)	3	4	15	-	12
Cs-USY(38)	38	40	-	-	1.5
Ni/Cs-USY(38)	38	40	15	-	1.3
Ce-Ni/Cs-USY(38)	38	40	15	20	1

3.2.1 Physicochemical characterization

The physical and chemical properties of the zeolite catalysts were analyzed by BET, H₂-TPR, water affinity (h index), CO₂ adsorption, XRD and TEM.

The XRD results are shown in **Figure 3.1a**. Several peaks corresponding to zeolites could be observed for USY(38) and USY(3) with no remarkable differences. The diffraction patterns of impregnated Ni samples present peaks at 37, 43 and 63°, corresponding to NiO phase. Ce-Ni samples present NiO peaks together with CeO₂. In this case, a decrease of FAU (Faujasite) zeolite peaks was observed. This effect could be attributed to the high adsorption coefficient of X-Ray radiation, a dilution effect due to the higher amount of metals or partial structural damage [4–6].

CO₂ affinity was measured by CO₂ adsorption. The CO₂ isotherm could give information about solids microporosity and material affinity to CO₂. As the supports had similar microporosity and micropores volume, the results were a direct indicator of the interaction between CO₂ and the catalyst. **Figure 3.1b** shows the CO₂ isotherms for Ni/Cs-USY(3) and Ni/Cs-USY(38). The sample with a lower Si/Al ratio presents a higher affinity to CO₂. The different basicity of the substrates could be the cause of the higher affinity for low Si/Al ratio. The interaction between CO₂ and the compensating cation through the framework oxygens [7], whose basicity is affected by the Si/Al ratio, being zeolites with lower Si/Al ratio more basic.

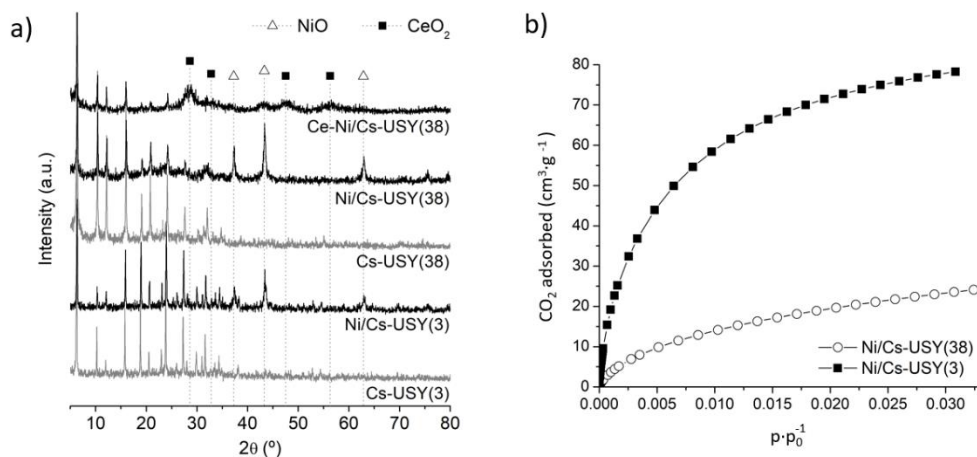


Figure 3.1. **a)** XRD pattern for Ni/Ce containing samples and zeolite substrate. **b)** CO₂ adsorption isotherm for Ni/Cs-USY(38) and Ni/Cs-USY(3).

Textural properties were analyzed by N₂ adsorption. The two types of zeolites presented slightly different properties (**Table 3.2**). Specifically, USY(38) samples have higher mesoporous volume, which is related to the preparation method [8]. The incorporation of Ni in both substrates cause a reduction of the pore volumes and external surface, as a direct effect of the presents of Ni inside and outside the pores (blockage N₂) [7,9]. This effect is boosted with the addition of Ce, due to the same cause, the presents of Ce inside the pores. Thus, Ce promoted catalyst presents the lower V_{meso} and BET surface area.

Regarding the H₂-TPR characterization, the profiles show two main peaks related to the reduction of NiO to metallic species (see **Figure 3.2**). The different peaks depend on the position of Ni in the catalyst. The peak at the lower temperature is related to the Ni located at the external surface of the zeolite [10,11], being easy to reduce. By contrast, the peak at higher temperature (<450 °C) is related to the Ni inside the structure, on the mesopores [9,12,13]. In fact, in previous studies, the reduction peak happening above 450 °C was attributed to the reduction of NiO or Ni²⁺ species inside the zeolite cavities [9,10,14]. This second peak was much higher in the samples with a higher Si/Al ratio, indicating that Ni was preferentially placed inside the structure. This is in agreement with the greater V_{meso} measured for USY(38) samples, allowing higher amount of Ni to be in a more stable position. However, for the Ni/Cs-USY(38), the Al content was relatively low, which makes the possibility of having Ni as compensating cation in the structure negligible. In summary, the results show that USY(3) would be easily reducible than USY(38) samples. When Ce was incorporated into the catalyst, a displacement of the NiO reduction peak to lower temperature was observed. The results were in concordance with the literature where Ce has been found to be able to enhance the Ni reducibility [4,13].

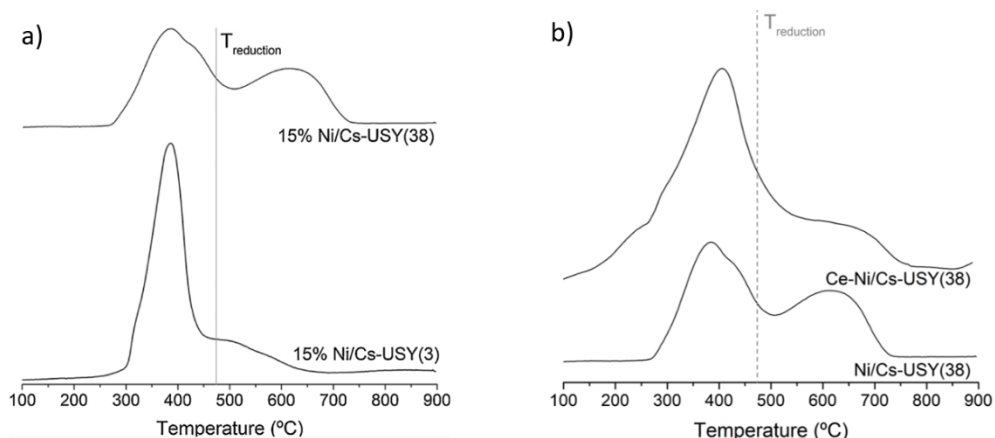


Figure 3.2. H₂-TPR results. **a)** Ni/Cs-USY(38) and Ni/Cs-USY(3) samples. **b)** Ni/Cs-USY(38) and Ce- Ni/Cs-USY(38) samples.

Hydrophobicity index was measured following a method proposed by Anderson et al. [15]. In general terms, the hydrophobicity index was obtained from the mass losses between 150 and 400 °C of samples previously saturated with water (TGA-DSC measurement). As seen in **Table 3.2**, the higher Al content is related to a higher h index. The h index agrees with the reported results indicating that water molecules adsorbed preferably in zeolite locations with charge separation, and these sites increase with the Al content.

Finally, the average size of Ni particle was estimated by TEM analysis. Samples were pre-reduced previously to convert NiO to metallic Ni. The average size was 19 nm ± 6 for Ni/Cs-USY(3) and 22 nm ± 10 for Ni/Cs-USY(38). Thus, particle size seems not to be affected by the ratio of Si/Al.

A summary of the main characteristics and properties can be found in **Table 3.2**.

Table 3.2. Overview of physical and chemical characterization.

Sample code	h index	V _{micro} (cm ³ ·g ⁻¹)	V _{meso} (cm ³ ·g ⁻¹)	S _{ext} (m ² ·g ⁻¹)	Ni size (nm)
Cs-USY(3)	-	0.22	0.07	84	-
Ni/Cs-USY(3)	0.60	0.19	0.04	22	19
Cs-USY(38)	-	0.19	0.30	319	-
Ni/Cs-USY(38)	0.87	0.16	0.20	165	22
Ce-Ni/Cs-USY(38)	0.76	0.09	0.19	162	-

3.3 DBD plasma reactor validation

The first experiments were done with a commercial catalyst (Ni/ γ -Al₂O₃, IBERCAT) to validate the reactor setup and determine the main parameters involved in the plasma-catalysis process. Plasma experiments were performed at 200 mL·min⁻¹ of CO₂/H₂ with 0.3 g of catalyst (GHSV of 40,000 mL·g⁻¹·h⁻¹) and plasma power was switched from 10 to 35 W, corresponding to a SEI between 73 and 256 kJ·mol⁻¹.

The CO₂ conversion and selectivity to methane obtained as a function of the applied power are shown in **Figure 3.3**. When the reactor was fed with a CO₂/H₂ gas mixture (1:4 ratio), experiments without catalyst showed low CO₂ conversion values, between 2 and 5%. CH₄ was not detected, being CO the main product (S_{CO} = 100%), generated mainly by electron impact dissociation. As soon as the catalyst was used, conversion increased up to 64 % at 35 W, while selectivity shifted to methane with values between 80 and 90%. Both conversion and selectivity increased with the plasma power. Thus, it was clearly seen that the catalyst is required to produce methane. With the use of Ni-based catalyst, conversion was boosted by one order of magnitude and selectivity was shifted from CO to CH₄.

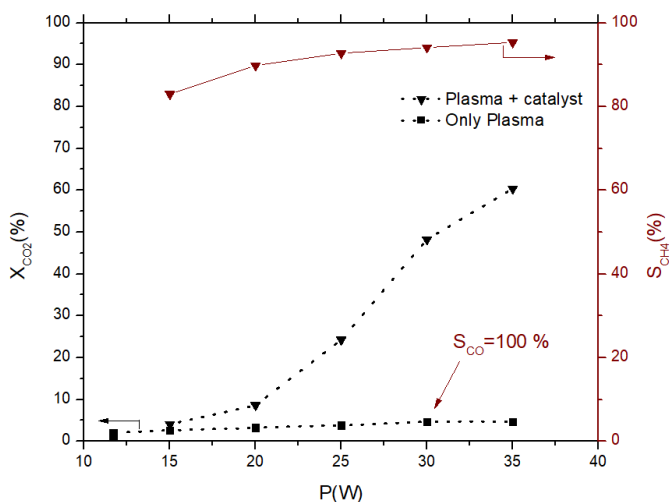


Figure 3.3. CO₂ conversion and CH₄ selectivity as a function of plasma power with and without the presence of the commercial catalyst.

Regarding the reactor temperature, it was measured a temperature between 100 °C and 170 °C in the catalyst bed during operation. The experiments were done at pseudo-adiabatic conditions (see **chapter 2**) without any heating. Thus, the reactor was initially at room temperature, and it warmed up as the applied plasma power was raised. The temperature values were caused by the heat released from the plasma, as well as the heat released by the exothermic methanation reaction [16–18]. A more extensive study of the generated heat will be discussed in **chapters 5** and **6**.

Finally, we compared the results obtained under plasma with the conventional thermal methanation (**Figure 3.4**). It was found that DBD plasma-catalyst showed a similar level of conversion at a much lower temperature, allowing CO₂ to be converted into methane under mild conditions. In this sense, 62% of X_{CO₂} and 95% of S_{CH₄} was obtained at temperatures as low as 150 °C, in agreement with reported results based on other catalysis formulation [19,20]. On the contrary, that level of conversion and selectivity was only obtained by thermal-catalysis at values higher than 350 °C. Therefore, plasma operation mode was able to work at a much lower temperature. These findings also imply that CO₂ methanation reaction was produced mainly due to the plasma activation rather than thermal activation due to bed heating.

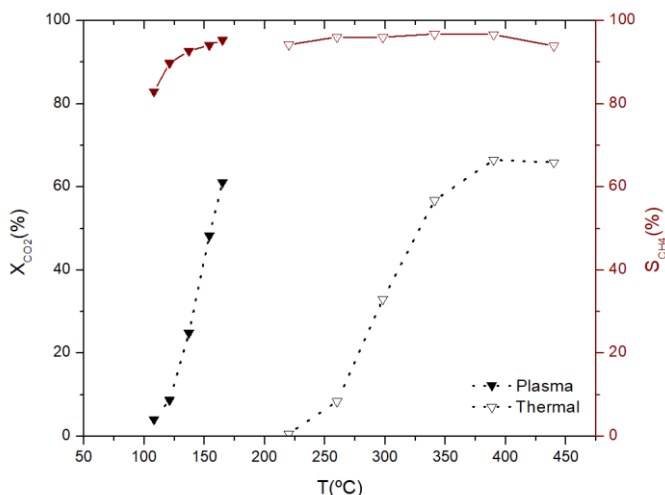


Figure 3.4. CO₂ conversion and CH₄ selectivity as a function of reactor bed temperature. Comparison of DBD-plasma and thermal activated catalytic methanation with commercial catalyst.

3.4 Catalytic results of Ni-Ce zeolite

In this section, Ni-based zeolite results are exposed. The effect of Si/Al ratio and the Ce addition in Ni-based zeolite was studied under plasma. Catalysts were tested in thermal catalysis (**Figure 3.5**) and plasma catalysis (**Figure 3.6**).

In thermal catalysis, Ni-based catalyst showed activity starting at a temperature around 250 °C with 5 to 10 % of CO₂ conversion. Thermodynamic equilibrium was reached at temperatures near 350-400 °C with a maximum conversion of around 70%. Regarding the Si/Al ratio effect, the higher ratio showed better performance in terms of conversion and selectivity to CH₄. The main differences in the catalytic performances of both catalysts were verified at 250–350 °C. Specifically, 30% more conversion and 10% increment in selectivity were observed for Ni/Cs-USY(38) catalyst. In addition, at a lower temperature, a limitation in the hydrogenation to CH₄ was observed, decreasing the selectivity. The reduction of the CH₄ selectivity verified at 300–350 °C for both samples could be explained taking into account the

mechanistic studies reported in previous studies [21]. Indeed, it was observed that between 300 and 350 °C, the dissociation and hydrogenation of CO into CH₄ was limited, being verified at these temperatures the highest CO selectivity [21]. Also, when increasing the reaction temperature, CO methanation was found to be favoured, being observed a significant increase of the CH₄ selectivity as also verified in our present results.

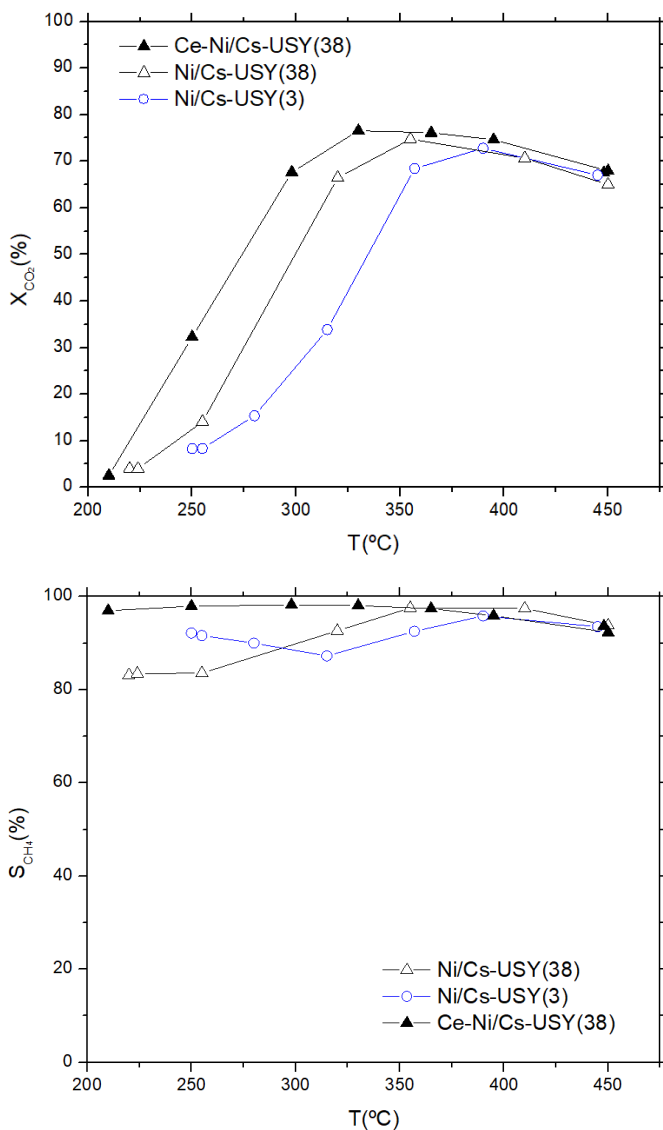


Figure 3.5. Thermal catalytic results. CO₂ conversion and CH₄ selectivity under thermal methanation.

Finally, the incorporation of Ce in Ni/Cs-USY(38) enhanced both CO₂ conversion and CH₄ selectivity in thermal catalysis. The higher yield could be related to the effect of Ce on the Ni species reducibility and the favoured CO₂ activation on cerium oxide species [4,22–25].

In the case of plasma methanation, **Figure 3.6** shows the performance for the Ni/Cs-USY, the Ce promoter catalyst and the Cs-USY(38) support. The reaction took place at a lower temperature (70-170°C) compared with thermal methanation. Conversion and selectivity increased as a function of the applied power. In general, methane yield values were lower than those obtained in thermal operation (at the highest temperature); only the Ce-Ni/Cs-USY(38) catalyst presented similar values.

If we focus on the Si/Al ratio, the difference in the activity followed a similar trend to the result obtained in thermal catalysis; the catalyst with the highest Si/Al showed the best performance. However, lower conversion values were obtained compared with thermal catalyst, and the differences between each catalyst were more significant than the thermal methanation. Especially at higher power, with a 50 % of difference in conversion values and 10% of difference in the selectivity between the catalyst.

On the other hand, lower CH₄ selectivity was observed, especially at low supplied power. This could be related to a higher contribution of the CO₂ conversion into CO due to the plasma. As seen in **section 3.3**, the use of plasma without catalyst converted 5% of CO₂ into CO. In addition, the conversion to CO was further increased when reactor was packed with the zeolite support (**Figure 3.6**), doubling the conversion to CO (10% at 30 W). In both cases, CO was generated due to electron impact dissociation of CO₂. When using Ni catalyst, it seems that at those lower power, the contribution of the CO₂ dissociation into CO due to electron collisions will be higher, so that the observed CH₄ selectivity is lower. When increasing the supplied power, this effect is decreased, improving methane selectivity. We could also consider that the total amount of CO generated by the plasma at a specific power could be extrapolated for the USY(3) support results (2.4 mL of CO at 25 W). Then, comparing with the Ni-based catalyst at the same conditions, lower absolute amount of CO was detected (0.7 mL of CO). From these results, we can deduce that part of the CO generated by the plasma reacted with the catalyst.

In a similar way, the incorporation of Ce as a promoter benefits the catalytic performance in plasma methanation. The conversions were displaced to lower power, with a maximum value of 78% and selectivity of 98%. It can be highlighted that the improvement in performance was more important in plasma, where catalytic activity increased from 8% to near 66% at power values as low as 20 W (**Figure 3.6**). This enhancement could be attributed to several simultaneous and probably synergetic effects, as will be discussed in the next section.

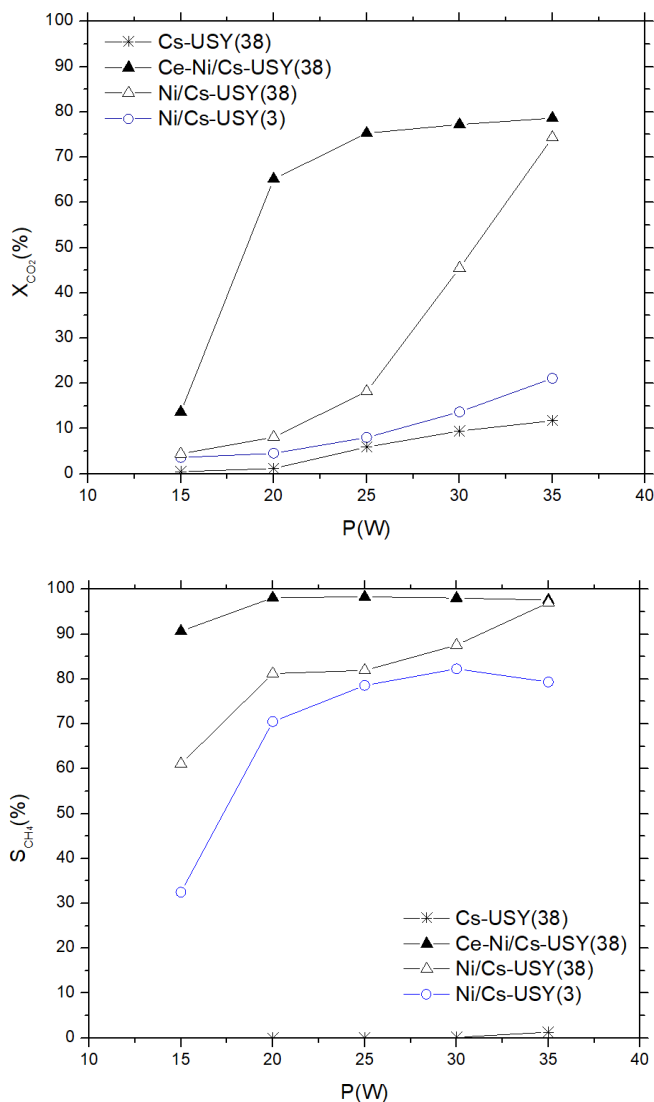


Figure 3.6. Plasma catalytic results. CO₂ conversion and CH₄ selectivity under plasma conditions.

In general, the catalytic performance under plasma and thermal conditions revealed that catalyst followed a similar trend than in thermal conditions. However, under plasma, the differences were more pronounced than in thermal catalysis. That effect could be observed if we focused on the methane yield at similar working points (**Figure 3.7**). For the different Si/Al ratio, at the highest applied power, the Ni/Cs-USY(38) yield reached similar values to the obtained in thermal catalysis. However, the Ni/Cs-USY(3) reached only 20% methane yield compared with the 70% obtained in thermal operation in the same conditions (**Figure 3.7a**). In a similar way, the different in yield values for the Ce promoted catalyst was enhanced in plasma (**Figure 3.7b**).

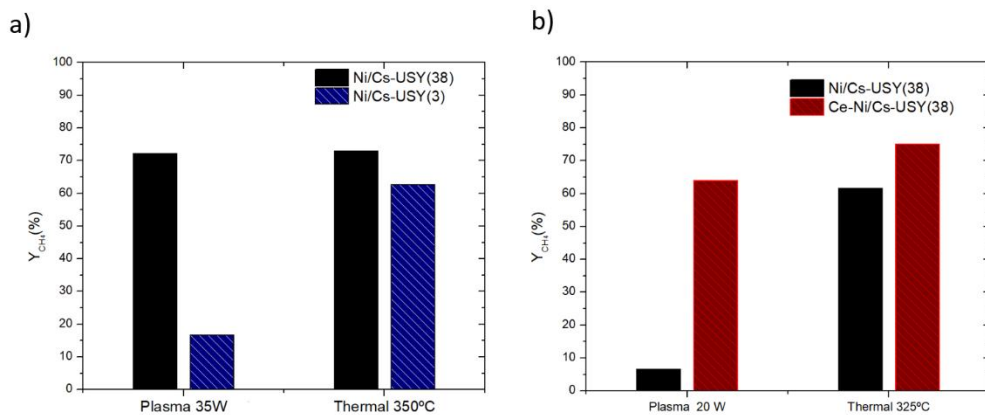


Figure 3.7. Comparison of the methane yield in plasma and thermal conditions under similar working conditions indicated in the figure **a)** effect of Si/Al ratio **b)** effect of Ce.

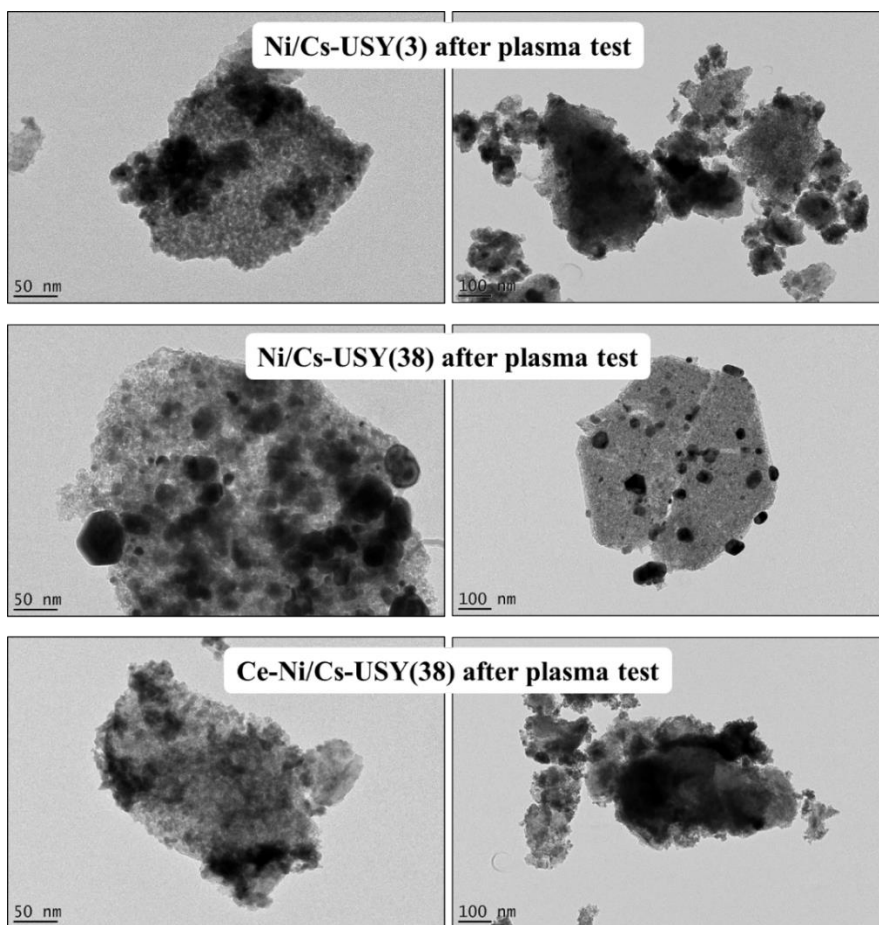


Figure 3.8. TEM micrographs obtained for the Ni/Cs-USY(3), Ni/Cs-USY(38) and Ce-Ni/Cs-USY(38) samples after plasma tests.

Finally, after plasma tests, samples were characterized by TEM and TGA-DSC (under airflow) in order to verify the presence of carbon. As seen in TEM micrographs (**Figure 3.8**) and TGA results (**Appendix B**), no carbon deposition was found. Indeed, by TEM no indication about the presence of carbon filaments was verified while the TGA-DSC profiles were not significantly different from the obtained for the pre-reduced samples.

3.5 Discussion

In agreement with the literature for CO₂ methanation, several factors such as a good metallic dispersion, the presence of activation sites for CO₂, the hydrophobicity of the supports or the dielectric properties could be responsible for significant enhancements on the catalytic performances towards CO₂ methanation [26–29]. The zeolite-based catalyst used in this chapter presented differences in terms of basicity/affinity to CO₂, hydrophobicity, dielectric constant, and metallic dispersion. In this regard, the different factors that could enhance the activity will be discussed in this section.

1. Hydrophobicity

The first parameter is the hydrophobicity of the catalyst. Water presents an inhibitory effect on the CO₂ methanation reaction, according to the literature [9,30–32]. Indeed, H₂O molecules will occupy the active sites where CO₂ could be adsorbed [33]. Additionally, and being CO₂ methanation a reversible reaction ($\text{CO}_2 + 4 \text{H}_2 \rightleftharpoons \text{CH}_4 + 2 \text{H}_2\text{O}$), a higher amount of water molecules adsorbed close to the Ni⁰ active sites will favour the reverse reaction [9,30–32,34–36]. In addition, the effective water removal from the catalyst surface is an additional effect of the plasma catalysis when applied to the CO₂ methanation reaction [2,3,37]. In the present work, it was found that zeolites with higher Si/Al ratios do not strongly interact with water (high hydrophobicity index (h)). This has a direct effect on the different Si/Al ratio in thermal catalysis.

Consequently, with the catalyst with a higher Si/Al ratio and lower affinity to water, the inhibitory role of H₂O molecules in the reaction will be lower, and the effect of plasma can be more effective. Indeed, plasma could be mainly responsible for the activation of the catalyst active sites rather than the removal of the water molecules from the sample's surface.

2. Dielectric properties

As commented at the beginning of this section, dielectric properties are an important factor in plasma process. Zhang et al. [28] reported that the dielectric properties of the catalysts could be responsible for modifications in the electric field distribution near the catalyst surface. Indeed, it was indicated that the electric field could be enhanced due to the polarization effect and the charge accumulation on the dielectric surface, modifying the electron impact reaction rates and, thus, changing the chemical composition of plasma. The composition is directly related to the presence of reactive species, which are indeed reaching the catalyst's surface and leading to changes in the catalytic

activity [28]. As a result, a catalyst with a higher dielectric constant could be responsible for better catalytic performances under plasma conditions [28]. Additionally, several authors have studied the dielectric properties of Y zeolite [38,39], being reported that they may arise from the mobility of the compensating cations in the zeolites lattice. It was observed that a lower Si/Al leads to better dielectric properties (higher dielectric constant and more effective propagation of plasma in the sample), since the number of cations in the framework is higher due to the presence of more AlO_4^- tetrahedral, and thus, more negative charges to be compensated [38,40]. Thus, as the zeolites studied in the present work have the same compensating cation, the dielectric properties of the Ni/Cs-USY(38) would be expected to be less beneficial for the plasma catalysis than those of the Ni/Cs-USY(3) sample, since a lower content of cations are present in the sample with higher Si/Al ratio (**Table 1**). However, in the present work, the increase in the dielectric constant seems not to be the critical factor responsible for an enhancement of the catalytic performances in the different ratio Si/Al zeolites.

In the case of Ce promoted catalyst, the higher dielectric constant of CeO_2 ($\epsilon_r=24$ for CeO_2 versus $\epsilon_r=1.5-5$ for zeolites) could be responsible for an enhancement of the catalytic performances [28]. In the same line, Al_2O_3 presents a dielectric constant of 8–10, so that the dielectric properties of the alumina-based sample will be less favourable for the application under non-thermal plasma conditions when compared with a sample containing CeO_2 .

3. Additional consideration

As seen in **section 3.2**, catalyst presents slightly different structural properties. First, the BET surface area and V_{meso} shows higher values for the Cs-USY(38) compared with Cs-USY(3). Despite this, the average Ni° size was not significantly different between the Ni/USY sample. In the presence of Ce, the dispersion of Ni° particles will be expectably higher. The higher dispersion could improve the activity on Ce promoted catalyst.

On the other hand, the different species generated by the plasma, such as radicals, excited species and ions, are the main pieces to role the activity in plasma conditions. All these species contribute to the overall conversion by gas-phase and plasma-assisted surface reaction. The use of catalysts shifted the selectivity and boosted the conversion by increasing the consumption of active species in plasma-enhanced surface reactions. As seen in **section 3.3.2**, CO generated by the plasma was converted to CH_4 when Ni-based catalysts were used. In addition, other species such as excited molecules, ions and radicals would also be adsorbed on the catalyst and contribute to the conversion towards CH_4 . Thus, it is important to consider the different activation pathways that plasma generates and how this could change the catalyst activity.

Taking into account the results of plasma-assisted CO₂ methanation tests followed the order: Ce-Ni/Cs-USY(38) > Ni/Cs-USY(38) > Ni/Cs-USY(3). The commented properties would moderate the different catalyst activity. From the main properties exposed in the previous paragraph, one could try to identify the most relevant characteristics affecting the catalyst performance. In order to facilitate the comparison, **Table 3.3** summarizes the main properties.

Table 3.3 Summary of the main properties of the zeolite-based catalyst.

	Ce-Ni/Cs-USY(38)	Ni/Cs-USY(38)	Ni/Cs-USY(3)
Hydrophobicity	↑	↑↑	↓
CO ₂ affinity	↑	↓	↑
Ni ⁰ dispersion	↑	↓	↓
Dielectric properties	↑↑	↓	↑
Textural properties	↑↑	↑	↓

The data obtained for the Ni/Cs-USY(38) sample point out that the hydrophobic properties of the materials and the better textural properties play the most relevant role in the observed results in both thermal and plasma activation. In fact, lower CH₄ yields were obtained for the Ni/Cs-USY(3), even though it has better CO₂ affinity and dielectric properties that could affect the plasma performance.

On the other hand, when comparing the Ni/Cs-USY(38) with the Ce-Ni/Cs-USY(38) catalyst, being the hydrophobic character similar in both samples, the presence of additional activation sites for CO₂, the better dielectric properties and the higher dispersion could be identified as responsible for the higher CH₄ yield obtained in the bimetallic sample. To sum up, the use of hydrophobic zeolites containing additional active sites for CO₂ adsorption/activation and presenting good dielectric properties and metallic dispersion will be the most promising route for the achievement of active and selective zeolite-based catalysts for CO₂ methanation under non-thermal DBD plasma conditions.

3.6 Conclusions

In this chapter, we have validated the DBD plasma reactor, built at the beginning of this thesis. The DBD reactor worked under pseudo-adiabatic conditions, without any external heater. A commercial catalyst was used for this purpose. The catalytic performances were compared in conventional thermal catalysis and in plasma catalysis. A 60% CO₂ conversion and CH₄ selectivity of around 80% were obtained in plasma methanation. Reactor temperature reached 100 to 170 °C, due to the heat generated by the methanation reaction and the plasma. The DBD was able to activate the reaction at low temperatures obtaining similar results to thermal catalysis.

After the validation, we focused on the study of different Ni-based zeolites catalysts, investigating the role of the zeolite structure composition (Si/Al ratio) and the incorporation of Ce as a promotor. We found that plasma enhances the difference between the catalyst. The incorporation of Ce into the catalyst was even more pronounced in plasma catalysis. In this regard, the results show that the use of Ce in Ni-based catalyst for plasma methanation could boost the conversion and reduce the applied power.

The different catalyst properties and the relation with the activity in plasma and thermal methanation have been discussed. We have concluded that one of the main properties of Ni-based zeolite catalyst was the hydrophobicity and the better textural properties. In the case of Ce promoted catalyst in plasma methanation, the dielectric properties of Ce, the additional active sites related with CO₂ and the higher dispersion were the key parameters that boost the methane yield. Finally, other factors as the different reactive species generated by the plasma could cause some differences in plasma reaction. In particular, we found important the different reaction paths caused by the species generated by the plasma, such as CO (5-10%).

Comparing all the catalysts, it is clear that Ni catalyst promoted with Ce presented the best results in plasma methanation. Further improvement in CO₂ conversion can be expected optimizing the Ce content.

3.7 References

- [1] E. Jwa, S.B. Lee, H.W. Lee, Y.S. Mok, Plasma-assisted catalytic methanation of CO and CO₂ over Ni-zeolite catalysts, *Fuel Process. Technol.* 108 (2013) 89–93. doi:10.1016/j.fuproc.2012.03.008.
- [2] F. Azzolina-Jury, F. Thibault-Starzyk, Mechanism of Low Pressure Plasma-Assisted CO₂ Hydrogenation Over Ni-USY by Microsecond Time-resolved FTIR Spectroscopy, *Top. Catal.* 60 (2017) 1709–1721. doi:10.1007/s11244-017-0849-2.
- [3] F. Azzolina-Jury, D. Bento, C. Henriques, F. Thibault-Starzyk, Chemical engineering aspects of plasma-assisted CO₂ hydrogenation over nickel zeolites under partial vacuum, *J. CO₂ Util.* 22 (2017) 97–109. doi:10.1016/j.jcou.2017.09.017.
- [4] M.C. Bacariza, I. Graça, J.M. Lopes, C. Henriques, Ni-Ce/Zeolites for CO₂ Hydrogenation to CH₄: Effect of the Metal Incorporation Order, *ChemCatChem.* 10 (2018) 2773–2781. doi:10.1002/cctc.201800204.
- [5] I. Graça, L.V. González, M.C. Bacariza, A. Fernandes, C. Henriques, J.M. Lopes, M.F. Ribeiro, CO₂ hydrogenation into CH₄ on NiHNaUSY zeolites, *Appl. Catal. B Environ.* 147 (2014) 101–110. doi:10.1016/j.apcatb.2013.08.010.
- [6] C.R. Moreira, M.M. Pereira, X. Alcobé, N. Homs, J. Llorca, J.L.G. Fierro, P. Ramírez de la Piscina, Nature and location of cerium in Ce-loaded Y zeolites as revealed by HRTEM and spectroscopic techniques, *Microporous Mesoporous Mater.* 100 (2007) 276–286. doi:10.1016/j.micromeso.2006.11.019.
- [7] M.C. Bacariza, R. Bértolo, I. Graça, J.M. Lopes, C. Henriques, The effect of the compensating cation on the catalytic performances of Ni/USY zeolites towards CO₂ methanation, *J. CO₂ Util.* 21 (2017) 280–291. doi:10.1016/j.jcou.2017.07.020.
- [8] P. Levecque, D.W. Gammon, P. Jacobs, D. De Vos, B. Sels, The use of ultrastable Y zeolites in the Ferrier rearrangement of acetylated and benzylated glycals, *Green Chem.* 12 (2010) 828. doi:10.1039/b921051b.
- [9] M.C. Bacariza, I. Graça, J.M. Lopes, C. Henriques, Enhanced activity of CO₂ hydrogenation to CH₄ over Ni based zeolites through the optimization of the Si/Al ratio, *Microporous Mesoporous Mater.* 267 (2018) 9–19. doi:10.1016/j.micromeso.2018.03.010.
- [10] M.C. Bacariza, I. Graça, A. Westermann, M.F. Ribeiro, J.M. Lopes, C. Henriques, CO₂ Hydrogenation Over Ni-Based Zeolites: Effect of Catalysts Preparation and Pre-reduction Conditions on Methanation Performance, *Top. Catal.* 59 (2016) 314–325. doi:10.1007/s11244-015-0435-4.
- [11] E. Sahle-Demessie, V.G. Devulapelli, A.A. Hassan, Hydrogenation of Anthracene in Supercritical Carbon Dioxide Solvent Using Ni Supported on H β -Zeolite Catalyst, *Catalysts.* 2 (2012) 85–100. doi:10.3390/catal2010085.
- [12] M. Tao, X. Meng, Y. Lv, Z. Bian, Z. Xin, Effect of impregnation solvent on Ni dispersion and catalytic properties of Ni/SBA-15 for CO methanation reaction, *Fuel.* 165 (2016) 289–297. doi:10.1016/j.fuel.2015.10.023.
- [13] M.C. Bacariza, I. Graça, S.S. Bebiano, J.M. Lopes, C. Henriques, Micro- and mesoporous supports for CO₂ methanation catalysts: A comparison between SBA-15, MCM-41 and USY zeolite, *Chem. Eng. Sci.* 175 (2018) 72–83. doi:10.1016/j.ces.2017.09.027.
- [14] G. Alonso, F. Keshavarz, P. Gamallo, Nous mètodes de captura i separació de CO₂ aplicables a processos industrials, *Rev. La Soc. Catalana Química.* 0 (2016) 21–30. doi:10.2436/20.2003.01.71.
- [15] M.W. Anderson, J. Klinowski, Zeolites treated with silicon tetrachloride vapour. Part 1.—Preparation and characterisation, *J. Chem. Soc. Faraday Trans. 1 Phys. Chem. Condens. Phases.* 82 (1986) 1449. doi:10.1039/f19868201449.

- [16] A. Parastaev, W.F.L.M. Hoeben, B.E.J.M. van Heesch, N. Kosinov, E.J.M. Hensen, Temperature-programmed plasma surface reaction: An approach to determine plasma-catalytic performance, *Appl. Catal. B Environ.* 239 (2018) 168–177. doi:10.1016/j.apcatb.2018.08.011.
- [17] T. Nozaki, K. Okazaki, Non-thermal plasma catalysis of methane: Principles, energy efficiency, and applications, *Catal. Today.* 211 (2013) 29–38. doi:10.1016/j.cattod.2013.04.002.
- [18] E.K. Gibson, C.E. Stere, B. Curran-McAteer, W. Jones, G. Cibin, D. Gianolio, A. Goguet, P.P. Wells, C.R.A. Catlow, P. Collier, P. Hinde, C. Hardacre, Probing the Role of a Non-Thermal Plasma (NTP) in the Hybrid NTP Catalytic Oxidation of Methane, *Angew. Chemie Int. Ed.* 56 (2017) 9351–9355. doi:10.1002/anie.201703550.
- [19] M. Nizio, A. Albarazi, S. Cavadias, J. Amouroux, M.E. Galvez, P. Da Costa, Hybrid plasma-catalytic methanation of CO₂ at low temperature over ceria zirconia supported Ni catalysts, *Int. J. Hydrogen Energy.* 41 (2016) 11584–11592. doi:10.1016/j.ijhydene.2016.02.020.
- [20] M. Nizio, R. Benrabbah, M. Krzak, R. Debek, M. Motak, S. Cavadias, M.E. Gálvez, P. Da Costa, Low temperature hybrid plasma-catalytic methanation over Ni-Ce-Zr hydrotalcite-derived catalysts, *Catal. Commun.* 83 (2016) 14–17. doi:10.1016/j.catcom.2016.04.023.
- [21] A. Westermann, B. Azambre, M.C. Bacariza, I. Graça, M.F. Ribeiro, J.M. Lopes, C. Henriques, Insight into CO₂ methanation mechanism over NiUSY zeolites: An operando IR study, *Appl. Catal. B Environ.* 174–175 (2015) 120–125. doi:10.1016/j.apcatb.2015.02.026.
- [22] Y. Fu, Y. Wu, W. Cai, B. Yue, H. He, Promotional effect of cerium on nickel-containing mesoporous silica for carbon dioxide reforming of methane, *Sci. China Chem.* 58 (2015) 148–155. doi:10.1007/s11426-014-5251-3.
- [23] G. Zhou, H. Liu, K. Cui, A. Jia, G. Hu, Z. Jiao, Y. Liu, X. Zhang, Role of surface Ni and Ce species of Ni/CeO₂ catalyst in CO₂ methanation, *Appl. Surf. Sci.* 383 (2016) 248–252. doi:10.1016/j.apsusc.2016.04.180.
- [24] S. Tada, T. Shimizu, H. Kameyama, T. Haneda, R. Kikuchi, Ni/CeO₂ catalysts with high CO₂ methanation activity and high CH₄ selectivity at low temperatures, *Int. J. Hydrogen Energy.* 37 (2012) 5527–5531. doi:10.1016/j.ijhydene.2011.12.122.
- [25] A. Westermann, B. Azambre, M.C. Bacariza, I. Graça, M.F. Ribeiro, J.M. Lopes, C. Henriques, The promoting effect of Ce in the CO₂ methanation performances on NiUSY zeolite: A FTIR In Situ/Operando study, *Catal. Today.* 283 (2017) 74–81. doi:10.1016/j.cattod.2016.02.031.
- [26] P. Frontera, A. Macario, M. Ferraro, P. Antonucci, Supported Catalysts for CO₂ Methanation: A Review, *Catalysts.* 7 (2017) 59. doi:10.3390/catal7020059.
- [27] K. Ghaib, K. Nitz, F.-Z. Ben-Fares, Chemical Methanation of CO₂: A Review, *ChemBioEng Rev.* 3 (2016) 266–275. doi:10.1002/cben.201600022.
- [28] Y.-R. Zhang, E.C. Neyts, A. Bogaerts, Influence of the Material Dielectric Constant on Plasma Generation inside Catalyst Pores, *J. Phys. Chem. C.* 120 (2016) 25923–25934. doi:10.1021/acs.jpcc.6b09038.
- [29] H.H. Kim, Y. Teramoto, N. Negishi, A. Ogata, A multidisciplinary approach to understand the interactions of nonthermal plasma and catalyst: A review, *Catal. Today.* 256 (2015) 13–22. doi:10.1016/j.cattod.2015.04.009.
- [30] A. Borgschulte, N. Gallandat, B. Probst, R. Suter, E. Callini, D. Ferri, Y. Arroyo, R. Erni, H. Geerlings, A. Züttel, Sorption enhanced CO₂ methanation, *Phys. Chem. Chem. Phys.* 15 (2013) 9620. doi:10.1039/c3cp51408k.
- [31] S. Walspurger, G.D. Elzinga, J.W. Dijkstra, M. Sarić, W.G. Haije, Sorption enhanced methanation for substitute natural gas production: Experimental results and thermodynamic considerations, *Chem. Eng. J.* 242 (2014) 379–386. doi:10.1016/j.cej.2013.12.045.

- [32] M.A.A. Aziz, A.A. Jalil, S. Triwahyono, M.W.A. Saad, CO₂ methanation over Ni-promoted mesostructured silica nanoparticles: Influence of Ni loading and water vapor on activity and response surface methodology studies, *Chem. Eng. J.* 260 (2015) 757–764. doi:10.1016/j.cej.2014.09.031.
- [33] C.M. Mfoumou, S. Mignard, T. Belin, The preferential adsorption sites of H₂O on adsorption sites of CO₂ at low temperature onto NaX and BaX zeolites, *Adsorpt. Sci. Technol.* 36 (2018) 1246–1259. doi:10.1177/0263617418762494.
- [34] F. Ocampo, Développement de catalyseurs pour la réaction de méthanation du dioxyde de carbone, 2011.
- [35] A. Borgschulte, E. Callini, N. Stadie, Y. Arroyo, M.D. Rossell, R. Erni, H. Geerlings, A. Züttel, D. Ferri, Manipulating the reaction path of the CO₂ hydrogenation reaction in molecular sieves, *Catal. Sci. Technol.* 5 (2015) 4613–4621. doi:10.1039/C5CY00528K.
- [36] H.. Yang, Q.. Dong, X.. Hu, X.. Ai, S.. Li, Preparation and characterization of LiNiO₂ synthesized from Ni(OH)₂ and LiOH·H₂O, *J. Power Sources.* 79 (1999) 256–261. doi:10.1016/S0378-7753(99)00158-5.
- [37] J. Amouroux, S. Cavadias, Electrocatalytic reduction of carbon dioxide under plasma DBD process, *J. Phys. D: Appl. Phys.* 50 (2017) 465501. doi:10.1088/1361-6463/aa8b56.
- [38] R. Schoonheydt, J.B. Uytterhoeven, Electrical conductivity study on synthetic faujasites type X and Y, *Clay Miner.* 8 (1969) 71–85. doi:10.1180/claymin.1969.008.1.08.
- [39] E. İzci, A. İzci, Dielectric behavior of the catalyst zeolite NaY, *Turk. J. Chem.* 31 (2007) 523–630.
- [40] H.-H. Kim, Y. Teramoto, T. Sano, N. Negishi, A. Ogata, Effects of Si/Al ratio on the interaction of nonthermal plasma and Ag/HY catalysts, *Appl. Catal. B Environ.* 166–167 (2015) 9–17. doi:10.1016/j.apcatb.2014.11.008.

Chapter 4

On the role of Ce in Ni-Ce/Al₂O₃ catalyst

The results presented in chapter 4 have been mainly published in Applied Catalysis A, General Journal as "*On the role of ceria in Ni-Al₂O₃ catalyst for CO₂ plasma methanation*" by M. Biset-Peiró, J. Guilera, T. Zhang, J. Arbiol, T. Andreu (Appl. Catal. A Gen. 575 (2019) 223-229). The published text and figures have been edited for this chapter. Some parts have been omitted, as have been shown in chapter 2 and chapter 3. Additional information and discussion have been added not included in the article.

4.1 Introduction

In view of the results obtained in **chapter 3**, the promotion of catalyst with Ce shows an extraordinary improvement in plasma methanation. The additional active sites and higher dielectric constant are good intrinsic properties of Ceria that could improve the methanation in plasma. Moreover, Ni-Ce catalysts can be further optimised for plasma CO₂ methanation.

In this chapter, we focused on the role of Ce in Ni/Al₂O₃ catalyst under plasma methanation. Catalysts with different Ce content over Ni-Alumina were studied. Although low alumina content presented a better performance in zeolite-based catalyst (**chapter 3, section 3.4**), we decided to move to an easy one-pot synthesis. Catalysts were prepared by one-pot evaporation-induced self-assembly (EISA). The synthesis process has been explained in **chapter 2 (section 2.7.2)**.

The obtained catalysts were physical and chemical characterized (**section 4.2**). The catalysts were evaluated under plasma and thermal conditions (**section 4.3.1**). On the other hand, we studied the key factors that govern plasma-catalysis. In this regard, the effect of CO generated by the plasma in the different catalysts was evaluated with CO methanation experiments (**section 4.3.2**). The main properties of Ni-Ce catalyst were discussed, and different catalytic mechanisms were proposed in plasma and thermal activation (**section 4.4**).

Finally, the energy efficiency of the catalysts synthesized in **chapter 3** and **chapter 4** was analyzed and compared with the most relevant results in the literature (**section 4.5**)

In summary, the objectives of this chapter are:

- Synthesis of Ni/Ce catalyst by EISA method.
- Optimize the Ce concentration in Ni catalyst supported on alumina.
- Determine the role of Ce in Ni-based catalyst.
- Study the energy efficiency and energy cost of the plasma methanation reaction.
- Comparison with the most relevant results in the literature (2017-2021).

4.2 Catalyst

Ni-Ce based catalysts supported on mesoporous alumina (Ce-Ni/Al₂O₃) were synthesized by EISA method. The synthesis method has been explained in **chapter 2**. In all samples, Ni content was fixed at 15 wt.%, as shown good performance for Ni-zeolite catalyst (**chapter 3**). The Ce content was varied between 0 and 50 wt.% (0, 2, 10, 20, 30, 40, 50 wt.%). A summary of catalysts composition obtained by ICP is shown in **Table 4.1**. The chemical composition agreed with the expected nominal values.

Table 4.1. Summary of Ce-Ni catalyst samples and metal content determined by ICP.

Sample name	ICP	
	wt.% Ni	wt.% Ce
Al ₂ O ₃	0.0	0.0
15Ni	15.0	0.0
2Ce-Ni	15.2	2.1
10Ce-Ni	15.1	10.2
20Ce-Ni	15.5	18.9
30Ce-Ni	15.2	26.3
40Ce-Ni	15.3	38.2
50Ce-Ni	15.0	48.3

4.2.1 Physicochemical characterization

The catalysts were initially physical and chemical characterized by N₂-pysisorption, H₂-TPR, XRD and TEM. A summary of the main results obtained by BET and H₂-TPR can be found in **Table 4.2**. BET analysis showed that the surface area of the blank sample was relatively high of 164 m²·g⁻¹. The mean pore size of the blank was 11 nm, within the mesoporous range. N₂-pysisorption isotherms presented an IV-type pattern in all samples (**Appendix C.1, Figure C.1**), typical of mesoporous materials.

Table 4.2. Summary of the main physicochemical characterization.

Sample	BET		H ₂ -TPR	
	Surface area (m ² ·g ⁻¹)	Pore size (nm)	T _{red} (°C)	H ₂ consumption (mol H ₂ ·mol _{Ni} ⁻¹)
Al ₂ O ₃	164	11	-	-
15Ni	81	5.4	500	0.95
2Ce-Ni	53	8.3	504	0.89
10Ce-Ni	77	4.6	430	0.94
20Ce-Ni	71	5.0	424	0.74
30Ce-Ni	42	4.3	426	0.62
40Ce-Ni	67	4.4	365	0.72
50Ce-Ni	32	3.7	383	0.69

BET measurements revealed a significant decrease in the surface area after Ni incorporation. In this sense, unpromoted 15Ni catalyst presented half of the surface

area compared with the blank sample (Al₂O₃), although 85% of the sample still consisted of Al₂O₃. The drastic reduction of surface area, together with the decrease of mean pore size (from 11 to 5 nm), suggests that the reduction of porosity by Ni incorporation is caused by pore blocking. In contrast, the incorporation of Ce led to minor modifications on the textural properties than Ni. For instance, the introduction of 10-20 wt. % of Ce only reduced 10% of the surface area in comparison to the unpromoted 15Ni sample. Nevertheless, the surface area was really affected at a high Ce loading, confirming that the sample porosity was mainly induced by Al₂O₃.

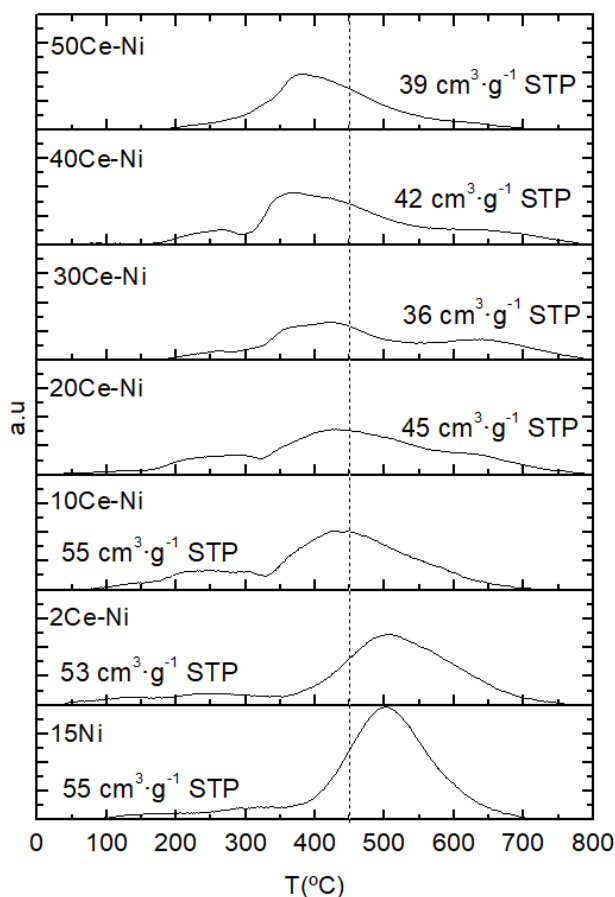


Figure 4.1. H₂-TPR profile of the Ce-Ni/Al₂O₃ catalysts.

The catalyst reducibility was studied by H₂-TPR measurement (**Table 4.2** and **Figure 4.1**). The unpromoted catalyst (15Ni) showed a reduction peak located at 450-500 °C related to the reduction of NiO species. The addition of Ce shifted the mean H₂ uptake peak to lower values (360-430 °C). Therefore, it was confirmed that the sample reducibility was highly improved by the incorporation of Ce. The hydrogen consumption is mainly attributed to the reduction of NiO species, while the reduction of superficial Ce is not relevant (2.8 cm³·g⁻¹ STP vs 35-55 cm³·g⁻¹ STP. **Appendix C.1, Figure C.2**). However, the total H₂ consumption initially decreases from 0.95 to

0.74 mol H₂·mol_{Ni}⁻¹, and it is maintained constant close to 0.7 at higher Ce loadings, suggesting that part of the Ni remains as Ni²⁺ in the structure [1].

XRD spectra are illustrated in **Figure 4.2**. In general, samples presented low crystallinity. No crystal peaks were detected at low Ce content. Different peaks appeared at high Ce loadings (>20 wt% of CeO₂). Peaks were related to CeO₂ phase (JCPDS 81-0792) and NiO phase (JCPDS 47-1049). CeAlO₃ phase (JCPDS 28-0260) was only detected at high Ce loading, namely 50Ce-Ni catalyst. The low calcination temperature (450 °C) was responsible for the poor crystallinity of the materials. Note that higher Al₂O₃ crystallinity was observed in trial samples that were prepared at higher temperatures (600-800 °C). However, it has been reported that catalyst performance decrease at high calcination temperatures as a result of lower Ni dispersion and emergence of the inactive NiAl₂O₄ phase [2].

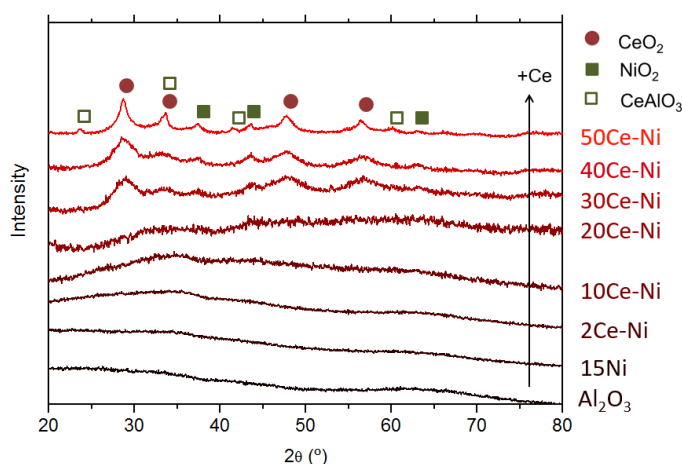


Figure 4.2. XRD pattern of samples.

BF TEM and HRTEM micrographs (**Figure 4.3**) revealed the structural and morphological information for the different reduced catalysts. An ordered mesoporous structure was observed for the 15Ni catalyst. The mesoporosity of the samples was induced by the presence of Pluronic P123 on the EISA synthesis. The ordered mesoporous structure disappeared when Ce was incorporated into the catalyst. Thus, the catalyst with higher Ce content is composed of different nanoparticles with irregular shapes. Ni nanoparticles could be observed in the BF TEM, HRTEM (**Figure 4.3**, dark spots), HAADF and EELS chemical composition maps (**Appendix C.1**, **Figures C.4**, **C.5** and **C.6**). The size distribution changes with the catalyst composition. The formation of bigger particles and clusters was induced as the Ce is incorporated, increasing the particle diameter from 3-4 nm to 10 nm for 15Ni and 30Ce-Ni (Ni and Ce). In addition, the EELS chemical compositions maps show that Ni, Ce and Al were distributed homogeneously, indicating a strong interaction between the elements. Finally, according to the HRTEM images, the catalysts with

low Ce content shows low crystallinity, in agreement with XRD results. At higher Ce content, CeO₂ crystalline particles were observed (**Appendix C.1, Figure C.7**).

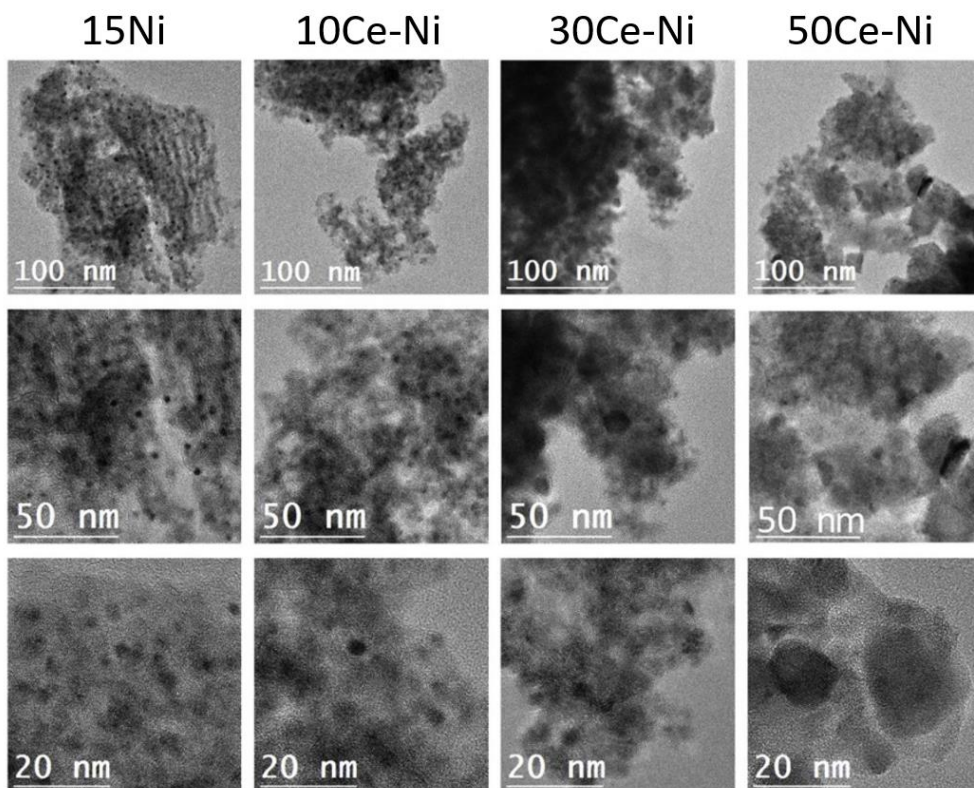


Figure 4.3. BF TEM micrographs (first and second row) and HRTEM micrographs (last row) of the different Ce-Ni/Al₂O₃ catalyst (15Ni, 10Ce-Ni, 30Ce-Ni and 50Ce-Ni).

4.3 Catalytic results of Ni-Ce/Al₂O₃

4.3.1 Effect of Ce

The effect of Ce on plasma-catalysis was studied by varying Ce content of Ce-Ni/Al₂O₃ samples between 0-50 wt.%. For comparison, the evaluation of the materials was performed on both thermal and DBD plasma-catalysis. All experiments were done with 200 mL·min⁻¹ of CO₂/H₂ and 0.3 g of catalyst (GHSV of 40,000 mL·g⁻¹·h⁻¹). For plasma experiments, the pseudo-adiabatic configuration was used. The catalytic performance on CO₂ methanation reaction is shown in **Figure 4.4** in thermal-mode and **Figure 4.5** under plasma conditions.

In thermal-catalysis experiments, conversion and selectivity rose with temperature up to reaching composition close to equilibrium. Conversion values between 70 and 80% with CH₄ selectivity from 85 to 97% were obtained (**Figure 4.4a** and **Figure 4.4b**, respectively). At a given temperature, CO₂ conversion was highly increased with the

incorporation of Ce into the Ni/Al₂O₃ materials. The synergic effects of Ce-Ni on thermal catalysis have been reported by other works. [1,3,4]. Ce promotes the reducibility of Ni active phase, as seen in H₂-TPR experiments, and it introduces basic sites to the catalyst surface; in this line, Aldana et al. proposed that CO₂ is firstly adsorbed on Ce sites, adsorbed CO₂ forms carbonates, and then, carbonates are hydrogenated to CH₄ [4]. The thermal-catalysis mechanism implies that CO₂ methanation does not go through CO formation as reaction intermediate. In our case, the formation of formates as intermediates in Ce-Ni/Al₂O₃ catalysts was corroborated by DRIFTS experiments (**Appendix C.1, Figures C.8 and C.9**) [5].

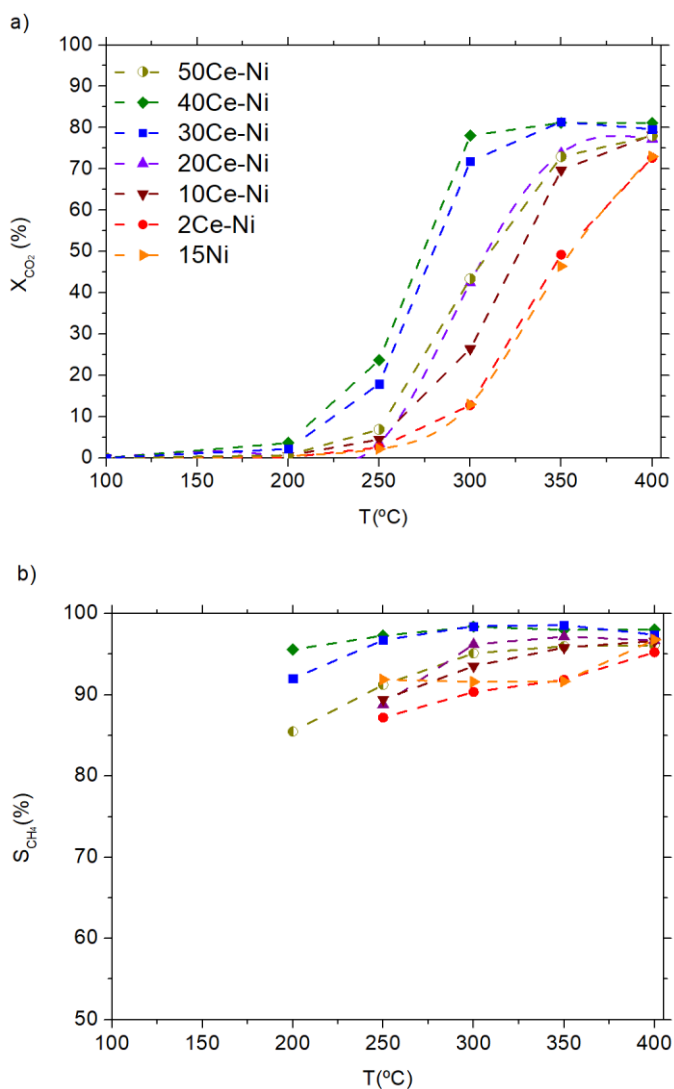


Figure 4.4. Thermal catalytic results. **a)** CO₂ conversion as a function of the temperature. **b)** CH₄ selectivity as a function of the applied power.

In plasma-catalysis experiments, the reactor was kept in pseudo-adiabatic conditions as in **chapter 3**. The plasma power was varied between 15-45 W, corresponding to SEI values between 110 and 330 kJ·mol⁻¹.

CO₂ conversion was increased over the power, at least within the 15 to 45 W range (**Figure 4.5a**). At higher power, similar values than thermal methanation were achieved (70-80%). In general, selectivity ranged from 85 to 98 % and only for a few conditions (catalyst with low activity at low power), selectivity was lower than 85% (**Figure 4.5b**). As seen in the previous chapter, temperatures increased due to the plasma and the methanation reaction, reaching temperatures between 150 and 180

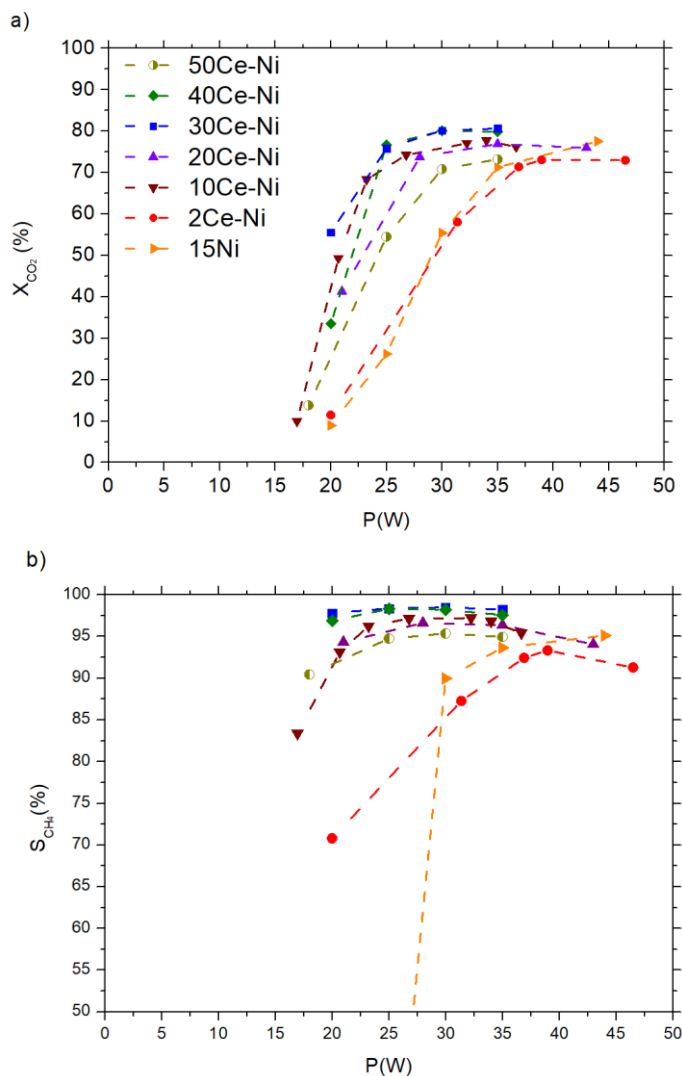


Figure 4.5. Plasma catalytic results. **a)** CO₂ conversion as a function of the temperature. **b)** CH₄ selectivity as a function of the applied power.

°C. The catalyst was tested for more than 9 hours without observing any deactivation (**Appendix C.1, Figure C.10**).

The incorporation of Ce on the catalyst led to higher conversions at similar power, analogously as the temperature effect in thermal-catalysis runs. Thus, plasma-catalyst activity was increased by the incorporation of Ce on Ni/Al₂O₃ based materials. The promoted effect was especially pronounced at low power and low Ce content. Likewise, the power demand was cut in half when Ce loadings were 10-40 wt.%. On the contrary, activity decreased by 50Ce-Ni sample both in thermal and plasma-catalysis runs. Finally, the use of Ce/Al₂O₃, without Ni, did not convert the CO₂ to CH₄ (**Appendix C.1, Figure C.11**), following the same trend as observed in chapter 3. It only increases the conversion to CO, as CO is generated from the dissociation of CO₂ produced by electron collision.

In general, thermal and plasma results showed similar features, the increase of activity due to the Ce incorporation. However, these benefits of Ce on the methanation reaction revealed some divergences for both modes, which can be clearly seen in **Figure 4.6**. A different optimum CeO₂ was revealed as a function of the operational mode. The activity enhancement on thermal-catalysis was more gradually with respect to the CeO₂ content (**Figure 4.6a**). As a representative example, the methane yields at 300 °C were doubled when the Ce content was also doubled (from 20 to 40 wt. %). On the contrary, the promoting effect of Ce on plasma-catalysts experiments was more abruptly at low loading levels (**Figure 4.6b**). In particular, similar yield values were achieved at a loading level range of 10-40 wt.%, showing a yield plateau pattern at intermediate Ce loading levels. Accordingly, it was revealed that less amount of Ce was necessary to improve CH₄ yield compared with thermal catalysis. These findings suggest that the optimal catalyst formulation shifted from thermal to plasma-catalyst.

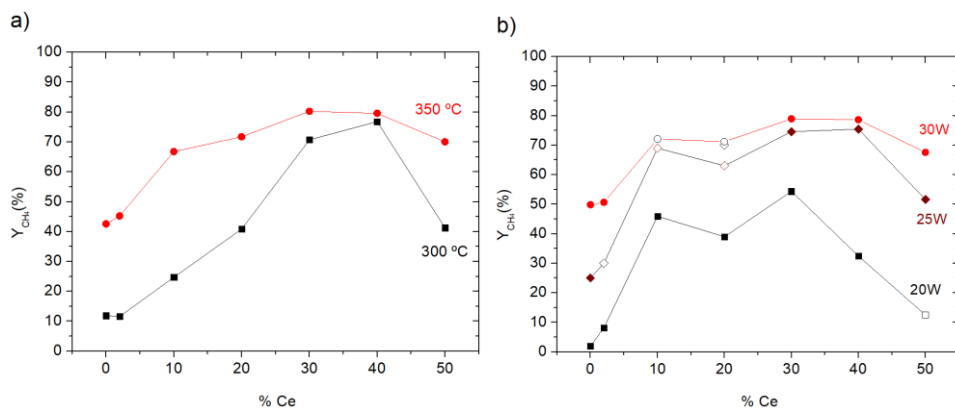


Figure 4.6. a) Thermal experiments. CH₄ yield as a function of the % Ce at constant temperature. b) Plasma experiments. CH₄ yield as a function of the % Ce at constant power.

4.3.2 CO methanation

In view of the results observed in previous sections, the role of CO generated by the plasma was further investigated. In plasma methanation, as soon as the plasma is generated in the reactor, several different types of radicals, ions and molecules are created, being the most abundant CO molecule and H radical [6]. Without any catalyst, plasma only forms CO, as it was shown in the previous result sections; in **chapter 3** (5-10%) and for the Ce-Ni/Al₂O₃ catalyst (**Appendix C.1, Figure C.11**). Thus, the evolution of the CO formed during plasma would play a role in the CO₂ methanation paths.

In order to determine the activity of CO, we performed thermal methanation of CO with the objective to study the evolution of the CO generated by the plasma at different Ce loading levels (2-30 wt.%). Information about the CO methanation setup can be found in **Appendix C.2**. **Figure 4.7** displays the effect of Ce on CO methanation at 300-400 °C. Methane yields increased over the temperature for all catalysts. The maximum methane yield was obtained at 10 wt.% loading level. Further addition of Ce was not beneficial for the conversion of CO to CH₄. A plausible explanation is that at higher Ce loading, the adverse textural effects were more relevant (i.e. surface area, pore size reduction and acid-base properties).

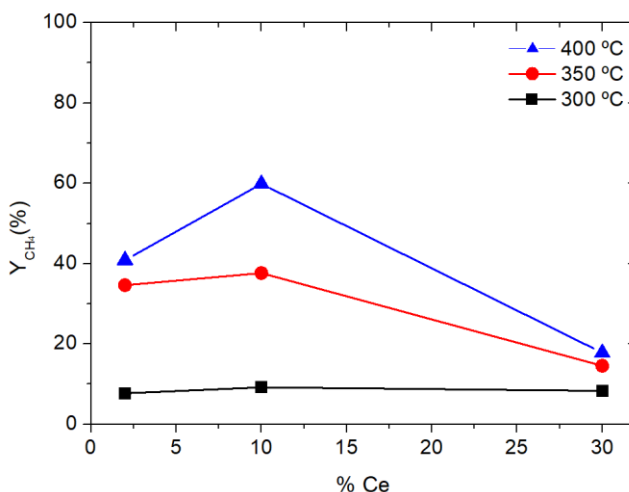


Figure 4.7. Catalytic results for CO methanation. CH₄ yield vs % Ce at a constant temperature (300, 350 and 400 °C).

4.4 Discussion: difference in activation path

The main catalyst properties are summarised in **Table 4.3**. For both reaction activation pathways (plasma and thermal), the incorporation of Ce plays the most relevant role, compared to the Ni dispersion and textural properties. In addition, the higher dielectric properties of Ce can enhance the plasma methanation reactions at higher Ce loadings (as has been discussed in **chapter 3**).

Table 4.3. Summary of the main properties.

	2Ce-Ni	10Ce-Ni	30Ce-Ni
Ce loading	↑	↑	↑↑↑
Dielectric properties*	↑	↑	↑↑↑
Ni ⁰ dispersion	↑	↑	↓
Textural properties	↑↑	↑	↓
CO ₂ methanation	↓	↑	↑↑
CO methanation*	↑	↑	↓

* The dielectric properties and CO methanation activity will only affect the CO₂ methanation experiments when the reaction is activated by plasma.

However, the experiments performed on CO₂ plasma-methanation revealed some differences with respect to thermal activation. The optimum Ce content was shifted to lower loadings in plasma experiments. These differences are associated to the CO₂ activation mechanism in thermal and plasma-catalysis. On thermal runs, the activation is carried out on the catalyst surface by thermal energy to overcome the energy barrier of the process. On plasma runs, CO₂ is already activated to CO at the gas phase by electric discharges, together with other reactive intermediates from CO₂ and H₂ (radicals, ions and molecules). Afterwards, the different species are adsorbed in the catalyst and converted into CH₄ (surface reactions).

The incorporation of Ce in Ni/Al₂O₃ catalyst plays a role in the CO₂ interaction. The main reaction mechanism can be affected as CO₂ methanation can go via CO or carbonates/formates depending on the catalyst composition, explaining the plateau observed. Thus, the study of the possible reactions paths for the different intermediates is required to understand the differences between thermal and plasma modes.

In this regard, the experiments on CO methanation revealed some information. The results showed that the methanation of CO is more active at low Ce content (**Figure 4.8**), probably due to better reducibility of Ni compared to non-containing Ce catalyst (H₂ consumption in H₂-TPR), and the activity decreases at higher Ce loading since the interaction with the basic CO molecule is not favourable.

In plasma mode, the boost in the catalyst's reactivity with lower Ce can be related to the CH₄ methanation coming from the generated CO by electric discharge, which is non-existing in thermal catalysis, together with the expected reaction pathway through CO₂ hydrogenation. The effect of the CO path will decrease when the Ce content increase, as this catalyst has shown less CO conversion in **Figure 4.8**. However, the

overall activity is kept high since it is compensated by the increase on the activity of the CO₂ methanation path, following the thermal results.

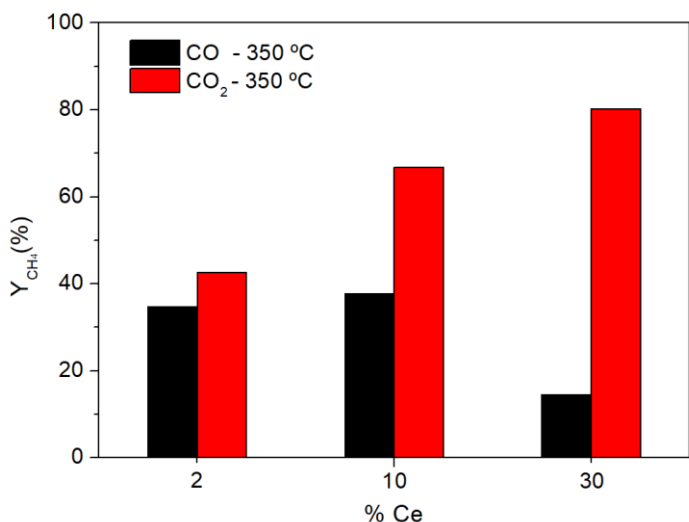


Figure 4.8. Comparison of methane yield for CO and CO₂ methanation as a function of % wt. Ce at 350 °C.

In view of these findings, two main reaction paths on Ni-Ce based catalysts are proposed in **Figure 4.9**. At high Ce content, the reaction is carried out mainly through activated species of CO₂ on the catalytic substrate, and they reacted with H₂ on Ni active site. This second mechanism is analogous to the conventional thermal-catalysis on Ni-Ce containing catalysts (**Figure 4.9b**). Thus, CO₂ is adsorbed through carbonates, forming formates as intermediates and converted to CH₄. However, under plasma activation, the same mechanism occurs at much lower temperatures due to the activation of CO₂ to CO₂*. In contrast, at low Ce content, CO₂ methanation through CO as reaction intermediate is enhanced [7]. The preferential methanation of CO on low Ce content catalysts, which exhibited more interesting textural properties, is presented as the main reason for the better performance of low Ce (10 wt.%) catalysts in plasma experiments.

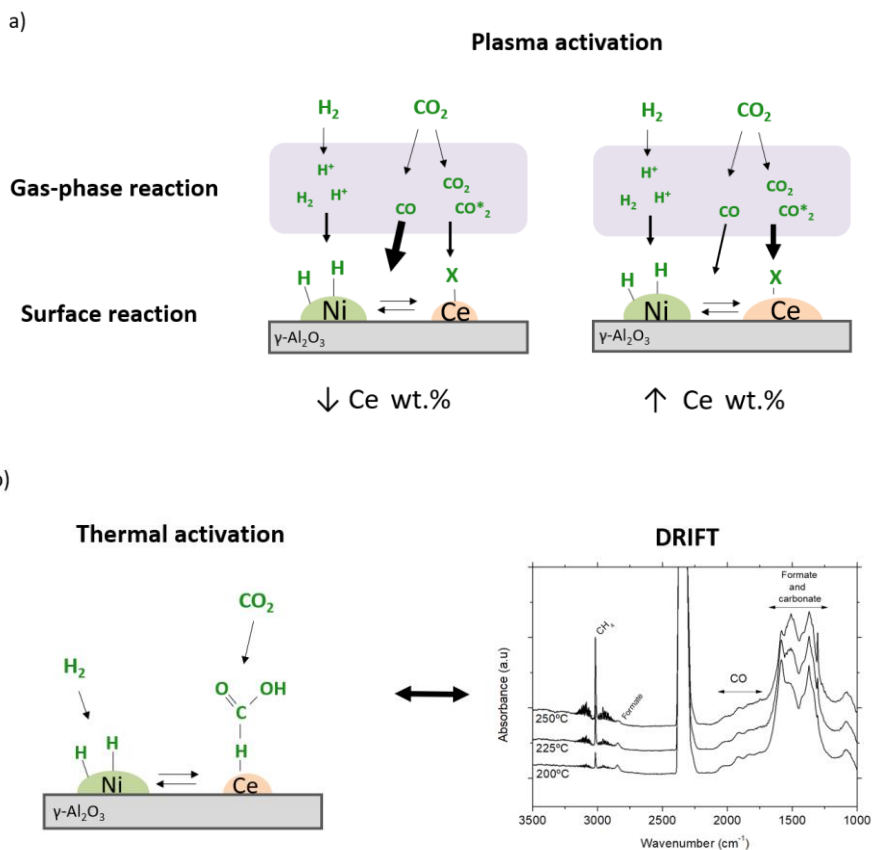


Figure 4.9. Proposed reaction mechanism. **a)** plasma methanation: low Ce content and high Ce content catalyst. **b)** methanation of CO_2 by thermal activation in Ce-Ni/ Al_2O_3 catalyst.

4.5 Energy efficiency and comparison with literature

In this last section, it is discussed the energy efficiency of the catalysts fabricated in **chapters 3** and **4** (Ce-Ni/ Al_2O_3 and Ce-Ni/Cs-USY). In addition, the results are compared with similar works in literature.

Figure 4.10 shows the energy efficiency of Ni and Ni-Ce catalyst for both sets of catalysts. As the results have shown, the optimization of the catalyst results in a reduction of the applied power, reducing the SEI and the energy cost. Therefore, the efficiency increased from 29 % to 40 % with the incorporation of Ce in the catalyst (Ni/ Al_2O_3), as a direct consequence of the higher conversion at lower applied power.

Comparing the Ce promoted catalyst of **chapters 3** and **4**, similar efficiencies were obtained, as catalytical results were similar. Highlight that the optimum load of Ce in chapter 4 was similar to the Ce load of Zeolite catalyst (30 % vs 20 %). In this regard, it seems that the promotion effect of Ce had more importance or produced a higher

effect than the different types of support (alumina vs zeolite). In both cases, the incorporation of Ce increased the activity at low power supplied, increasing the energy efficiency.

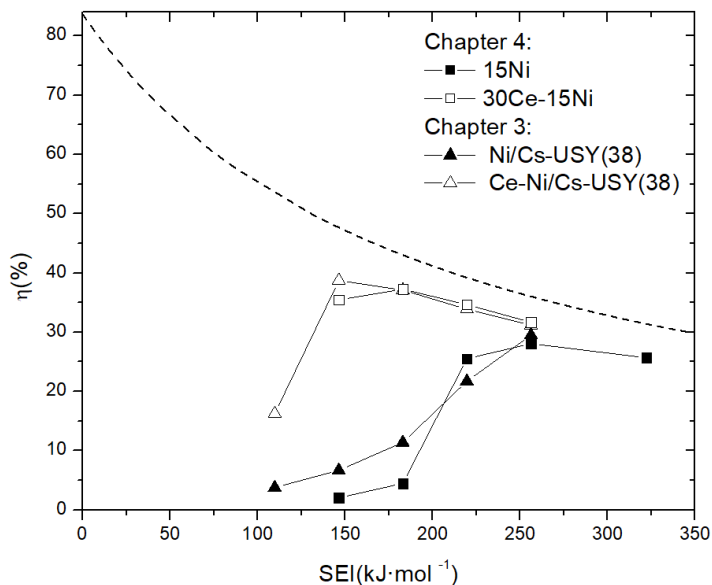


Figure 4.10. Energy efficiency as a function of SEI.

Considering the obtained results, the next objectives will be to further improve energy efficiency. We can see that the maximum theoretical efficiency at each applied SEI (**Figure 4.10**, dotted line) increased rapidly with the reduction of the SEI. Therefore, in order to obtain higher efficiencies, it is essential to maintain higher conversion while the SEI is reduced. The SEI values can be reduced by decreasing the applied power or increasing the flow at constant power. Both aspects will be studied in next chapters.

Finally, the results obtained for Ce-Ni/Al₂O₃ catalyst (**chapter 4**) and Ni-based zeolite (**chapter 3**) were compared with the most relevant results reported in the literature for plasma CO₂ methanation with Ni-based catalyst (**Table 4.3**). Similar reactor parameters and conditions are reported in terms of voltage, frequency and GHSV. In terms of the catalytic performance, the best samples obtained in this thesis are comparable to those reported in the literature (70-80%). Regarding the energy efficiency, higher values are reported (50-70%) as a direct cause of lower applied power [8–11]. Differences in reactor geometry and reactor configurations/setup can have a role in this aspect.

Table 4.3. Comparison with reported results in literature for plasma CO₂ methanation with Ni-based catalyst.

Catalyst	IBERCAT	Ce-Ni /Cs-USY	Ce-Ni /Al₂O₃	Ni /CeZr	Ni /CeZr	Ni /CeZr	Ni /BEA
V (kV _{pk})	4-9	4-9	4-9	6-9	6-9	6-9	18
f (kHz)	41-43	41-43	41-43	40-43	40-43	40-41	1
P (W)	15-35	15-35	15-35	3-16	3-9	12	n.a
X _{CO2} (%)	60	70	75-80	73	80	71	90
S _{CH4} (%)	95	95	97-98	95	98	100	n.a
T (°C)	70-170	70-170	130-190	120-170	110-270	270	180-260
SEI (kJ·mol ⁻¹)	100-250	100-250	100-250	29	21-65	87	n.a
EC (kJ·mol ⁻¹)	2200	1144	1200	211	140	618	n.a
η (%)	4-25	16-38	35-37	69	58-70	51	n.a
Ref.	Chap. 3	Chap. 3	Chap. 4	[8]	[9-10]	[11]	[12]

4.6 Conclusions

The benefits of plasma-methanation on Ni-Ce/Al₂O₃ are presented in this chapter. Ni-Ce/Al₂O₃ catalysts were synthesized by one-pot synthesis procedure. Following the same trend that in chapter 3, similar level of CO₂ conversion was achieved at much lower temperature by plasma-catalysis. The results observed in chapters 3 and 4 revealed that CO₂ methanation reaction was produced due to plasma activation, with a reduction of 200 °C respect to the thermal methanation experiments.

The role of Ce in Ni/Al₂O₃ catalyst was investigated. The presence of Ce on the catalyst was beneficial for plasma methanation. Unlike what is expected, the optimum composition of the catalyst might not be the same as for thermal-catalysis due to the presence of CO. Specifically, the amount of Ce can be reduced up to 10 wt.% Ce, with similar catalytic performance values between 10 and 40 wt. %. These results represent an important reduction on the optimum promoter content compared to thermal-catalysis, where the highest conversions at the lowest temperature are obtained at 40 wt. % of Ce.

The results showed that a lower amount of Ce is required in plasma methanation, as consequence of a change in the rate-determining steps. The different activation mechanisms have been proposed to be the cause of the differences between thermal and plasma activity. The direct dissociation under plasma of CO₂ to CO could increase the conversion rate of those catalysts with higher CO methanation activity.

In summary, CO₂ plasma methanation process is able to work over a catalyst with a lower Ce quantity, reducing the final catalyst cost and thus facilitating the implementation. These results prove the possibility to design catalysts taking advantage of the different rate-determining steps and the importance to analyse the different intermediate generated by the plasma.

In addition, the catalyst optimization improved the energy efficiency, boosting the efficiency from 29% to 40% for the optimum Ce composition (30Ce-15Ni). In this aspect, there is room to improve the CO₂ plasma methanation by keep exploring catalysts able to work at lower SEI values or optimizing the plasma reactor design, for example, by optimizing the geometry or the control of the generated heat.

4.7 References

- [1] F. Ocampo, B. Louis, L. Kiwi-Minsker, A.-C. Roger, Effect of Ce/Zr composition and noble metal promotion on nickel based Ce_xZr_{1-x}O₂ catalysts for carbon dioxide methanation, *Appl. Catal. A Gen.* 392 (2011) 36–44. doi:10.1016/j.apcata.2010.10.025.
- [2] S. Rahmani, M. Rezaei, F. Meshkani, Preparation of highly active nickel catalysts supported on mesoporous nanocrystalline γ -Al₂O₃ for CO₂ methanation, *J. Ind. Eng. Chem.* 20 (2014) 1346–1352. doi:10.1016/j.jiec.2013.07.017.
- [3] S. Tada, T. Shimizu, H. Kameyama, T. Haneda, R. Kikuchi, Ni/CeO₂ catalysts with high CO₂ methanation activity and high CH₄ selectivity at low temperatures, *Int. J. Hydrogen Energy.* 37 (2012) 5527–5531. doi:10.1016/j.ijhydene.2011.12.122.
- [4] P.A.U. Aldana, F. Ocampo, K. Kobl, B. Louis, F. Thibault-Starzyk, M. Daturi, P. Bazin, S. Thomas, A.C. Roger, Catalytic CO₂ valorization into CH₄ on Ni-based ceria-zirconia. Reaction mechanism by operando IR spectroscopy, *Catal. Today.* 215 (2013) 201–207. doi:10.1016/j.cattod.2013.02.019.
- [5] F. Wang, S. He, H. Chen, B. Wang, L. Zheng, M. Wei, D.G. Evans, X. Duan, Active Site Dependent Reaction Mechanism over Ru/CeO₂ Catalyst toward CO₂ Methanation, *J. Am. Chem. Soc.* 138 (2016) 6298–6305. doi:10.1021/jacs.6b02762.
- [6] C. De Bie, J. van Dijk, A. Bogaerts, CO₂ Hydrogenation in a Dielectric Barrier Discharge Plasma Revealed, *J. Phys. Chem. C.* 120 (2016) 25210–25224. doi:10.1021/acs.jpcc.6b07639.
- [7] F. Azzolina-Jury, F. Thibault-Starzyk, Mechanism of Low Pressure Plasma-Assisted CO₂ Hydrogenation Over Ni-USY by Microsecond Time-resolved FTIR Spectroscopy, *Top. Catal.* 60 (2017) 1709–1721. doi:10.1007/s11244-017-0849-2.
- [8] R. Benrabbah, C. Cavaniol, H. Liu, S. Ognier, S. Cavadias, M.E. Gálvez, P. Da Costa, Plasma DBD activated ceria-zirconia-promoted Ni-catalysts for plasma catalytic CO₂ hydrogenation at low temperature, *Catal. Commun.* 89 (2017) 73–76. doi:10.1016/j.catcom.2016.10.028.
- [9] M. Nizio, R. Benrabbah, M. Krzak, R. Debek, M. Motak, S. Cavadias, M.E. Gálvez, P. Da Costa, Low temperature hybrid plasma-catalytic methanation over Ni-Ce-Zr hydrotalcite-derived catalysts, *Catal. Commun.* 83 (2016) 14–17. doi:10.1016/j.catcom.2016.04.023.
- [10] M. Nizio, A. Albarazi, S. Cavadias, J. Amouroux, M.E. Galvez, P. Da Costa, Hybrid plasma-catalytic methanation of CO₂ at low temperature over ceria zirconia supported Ni catalysts, *Int. J. Hydrogen Energy.* 41 (2016) 11584–11592. doi:10.1016/j.ijhydene.2016.02.020.
- [11] M. Mikhail, B. Wang, R. Jalain, S. Cavadias, M. Tatoulian, S. Ognier, M.E. Gálvez, P. Da Costa, Plasma-catalytic hybrid process for CO₂ methanation: optimization of operation parameters, *React. Kinet. Mech. Catal.* 8247 (2018). doi:10.1007/s11144-018-1508-8.
- [12] E. Jwa, S.B. Lee, H.W. Lee, Y.S. Mok, Plasma-assisted catalytic methanation of CO and CO₂ over Ni-zeolite catalysts, *Fuel Process. Technol.* 108 (2013) 89–93. doi:10.1016/j.fuproc.2012.03.008.

Part II.

DBD reactor optimization

Chapter 5

Adiabatic DBD plasma reactor

The results presented in chapter 5 have been published in Chemical Engineering Journal as “*Adiabatic plasma-catalytic reactor configuration: Energy efficiency enhancement by plasma and thermal synergies on CO₂ methanation*” by M.Biset-Peiró, R.Mey, J.Guilera and T.Andreu (Chem. Eng. J. 393-124786 (2020)). The published text and figures have been marginally edited for this chapter. More specifically, the structure and have been modified compared with the article. Additional figures from the Supporting Info have been included in the chapter.

5.1 Introduction

This chapter is focused on the development and optimization of adiabatic plasma reactor in order to control the released heat, which has a positive economic impact as power application can be minimized. As observed in **chapters 3** and **4**, reactor temperature increased due to the heat released by the methanation reaction and the plasma heat losses. In **chapters 3** and **4**, the reactor worked in pseudo-adiabatic conditions, without thermal insulation and any external heating. Therefore, there was a significant amount of heat exchanged through the reactor wall and the surroundings. In addition, the energy efficiency values can be improved by reducing the SEI values. Owing to the fact that an excess of temperature is not beneficial for the methanation reaction, in favor to the RWGS reaction, a proper balance between reactor design (isolation) and reaction conditions (gas flowrate) should be found.

Herein, it is presented an adiabatic plasma-catalytic configuration by thermally insulating the reactor (**section 5.2**). The adiabatic configuration is compared with the pseudo-adiabatic reactor (**section 5.3**). The contribution of methanation and plasma to the reactor temperature in both adiabatic and pseudo-adiabatic is analyzed. In addition, the temperature dependence on the gas flow rate is further studied. Finally, the energy efficiency of the different configurations is analyzed and compared with the literature works (**section 5.4**)

For this study, optimum Ni-Ce composition was selected based on the results obtained in **chapters 3** and **4**. The catalyst was fabricated by wet impregnation (**chapter 2, section 2.7.3**).

In summary, the main objectives of this chapter are:

- Proof-of-concept of the adiabatic plasma configuration: synergy between plasma and thermal catalysis.
- Discern and report the heat contribution of methanation and plasma.
- Determine the influence of GHSV in pseudo-adiabatic and adiabatic reactor.
- Optimize the adiabatic reactor configuration in terms of energy efficiency.

5.2 Experimental setup: reactor and catalyst

The experiments performed in this chapter were done in pseudo-adiabatic (without thermal insulation) and adiabatic conditions (thermally insulated). **Figure 5.1** presents a scheme of the two configurations. As explained in **chapter 2, section 2.3**, the reactor was thermally insulated with expanded insulating spheres to work in adiabatic conditions.

In addition, reactor geometry was modified compared with the reactor used in chapters 3 and 4. The GAP was increased up to 2 mm. The diameter changes were done during an optimization study. The gap optimization experiments and the results obtained can be found in **Appendix A.2**.

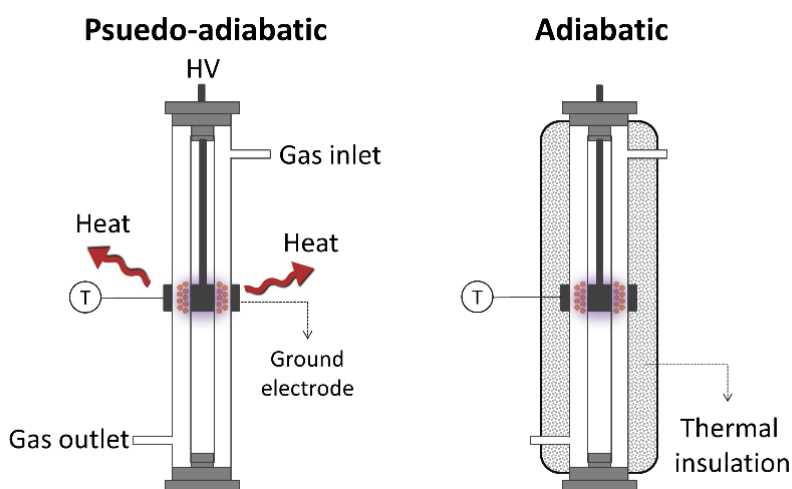


Figure 5.1. Reactor scheme of pseudo-adiabatic and adiabatic configuration.

Regarding the catalyst, Ni-Ce/Al₂O₃ catalyst was prepared by wet impregnation method using commercial mesoporous alumina support (Accu@spheres, Saint-Gobain Norpro, 500 μm), following the procedure explained in **chapter 2**. Metal loading of the catalyst (15 wt% Ni, 30 wt% Ce) was optimized in previous chapters. A basic characterization and catalyst comparison (30Ce-15Ni WET vs 30Ce-15Ni EISA) can be found in **Appendix D.1**.

5.3 Results

5.3.1 Adiabatic and pseudo-adiabatic reactor

Adiabatic and pseudo-adiabatic reactor was first studied at a GHSV of $40,000 \text{ mL}\cdot\text{h}^{-1}\cdot\text{g}^{-1}$ ($200 \text{ mL}\cdot\text{min}^{-1}$). **Figure 5.2** shows the registered temperature as a function of the applied power for both DBD plasma reactor configurations. Note that in neither case, external heating was used. The temperature clearly rose with the plasma power in all the experiments ($50\text{--}350 \text{ }^\circ\text{C}$). As first aspect to be considered, the increase of temperature can be led by the plasma heating losses, including de-excitation of molecules, ion neutralization, electron elastic collision, recombination, and dielectric heating [1–3]. The other contribution to the rise in temperature of the reactor is the heat produced by the methanation reaction.

To discern the effect of exothermic reaction in the temperature rise, experiments were performed using pure CO_2 or CO_2/H_2 mix in the pseudo-adiabatic configuration. In the case of pure CO_2 , as seen in **Figure 5.2** (pseudo-adiabatic CO_2), temperature was increased with the applied power, from $50 \text{ }^\circ\text{C}$ to $140 \text{ }^\circ\text{C}$. CO_2 conversions were kept below 5%, mainly due to CO formation by plasma CO_2 electron impact dissociation [4]. Thus, plasma was the main contributor to the increase in temperature. The application of plasma up to 25 W increased the reactor temperature by more than $100 \text{ }^\circ\text{C}$, even without insulation, only led by the heat generated by discharges.

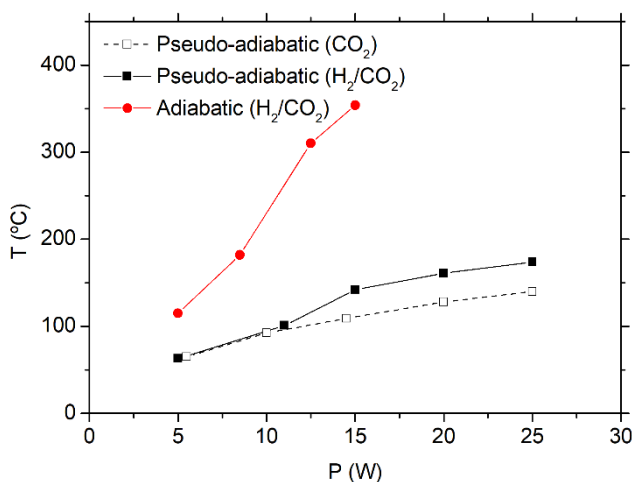


Figure 5.2. Temperature as a function of plasma power in adiabatic and pseudo-adiabatic configurations. GHSV of $40,000 \text{ mL}\cdot\text{h}^{-1}\cdot\text{g}^{-1}$.

A different behaviour was observed once H_2 was introduced in the feed (**Figure 5.2**, pseudo-adiabatic CO_2/H_2). At low power ($< 10 \text{ W}$), methanation reaction did not take place; thus, temperature was similar to using pure CO_2 . In contrast, the temperature was further increased at higher power. This pattern is a result of the exothermicity of the conversion of CO_2 to CH_4 . Besides the heat generated by plasma discharges, the contribution of the heat released by the reaction raised the temperature by $30 \text{ }^\circ\text{C}$

(140–175 °C) using a space velocity of 40,000 mL·h⁻¹·g⁻¹, which will be later discussed in **section 5.3.2**.

As soon as the reactor was thermally insulated to work under adiabatic conditions, the temperature was sharply increased (**Figure 5.2**, Adiabatic H₂/CO₂). In particular, the temperature raised from 100 °C to 200 °C at 10 W and up to 350 °C at 15 W. Therefore, the isolation of the reactor exhibited a strong impact on the reaction temperature.

The conversion values are reported in **Figure 5.3**. The conversion of CO₂ started to take place over 5 W in adiabatic configuration and over 10 W in pseudo-adiabatic configuration. The results are in agreement with the aforementioned increase in temperature produced by the CO₂ conversion. Selectivity values were kept close to 100% (**Appendix D.2, Figure D.4**). In the pseudo-adiabatic configuration, the maximum conversion (70–80%) was obtained at higher power (20–25 W). Interestingly, similar conversions were obtained at much lower power in adiabatic conditions. In a comparable working point (conversion and temperature), the highest conversion was displaced from 20 W (150 °C) in pseudo-adiabatic configuration to 8.5 W (180 °C) in adiabatic configuration. The highest conversion was obtained at 12.5 W in adiabatic conditions, power value that is much lower than in pseudo-adiabatic conditions (25 W). Accordingly, the increase in the reactor temperature by the isolation of the reactor positively reduced the required power input to obtain similar conversion values.

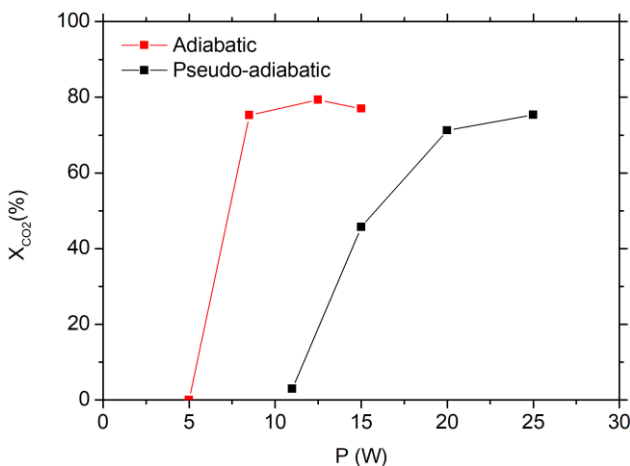


Figure 5.3. CO₂ conversion as a function of plasma power in adiabatic and pseudo-adiabatic configurations. GHSV of 40,000 mL·h⁻¹·g⁻¹.

In agreement with literature values [5,6], relatively high conversions were obtained in pseudo-adiabatic conditions at temperatures as low as 150–180 °C, without any external heating. In **Figure 5.4**, conversion versus temperature is shown for plasma experiments compared to the thermal methanation activity of NiCe catalyst. In neither of the two configurations, the initial temperature (150–180 °C) was not enough to

activate the reaction only by thermal-catalysis. Therefore, CO_2 and H_2 were successfully initially converted to CH_4 due to the synergic activation by both methods, plasma and thermally, with a threshold temperature near $150\text{ }^\circ\text{C}$.

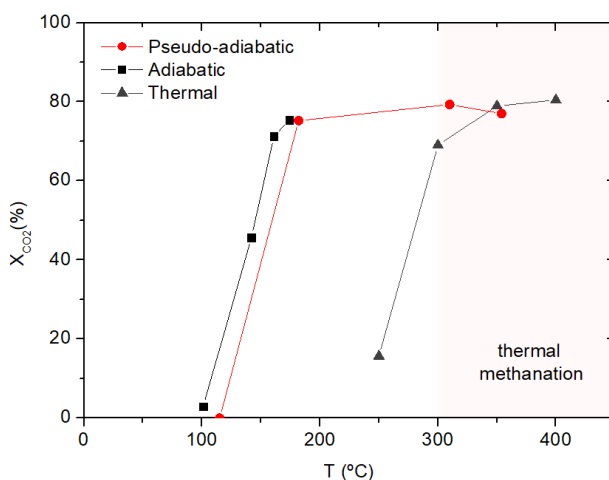


Figure 5.4. Conversion vs power for adiabatic, pseudo-adiabatic and thermal methanation at GHSV of $40,000\text{ mL}\cdot\text{h}^{-1}\cdot\text{g}^{-1}$.

However, the role of temperature gained importance in adiabatic conditions as the reaction was activated by both methods: thermal and plasma activation. The role of plasma would be the activation of CO_2 to energetically active species, such as excited species (electronic and vibrational), radicals (H , CHO , C , etc.), ions (CO_2^+ , etc.) and other subproducts as CO (from CO_2 electron impact dissociation) [7]. These species would enhance the activity by lowering the energy barrier allowing to work at lower temperatures, as proposed by J. Kim et al. [8] for CH_4 activation. In our case, the different excited CO_2 molecules would react with the Ni-Ce catalyst and, in adiabatic conditions, the reaction would take place at lower power, where the CO_2 is already activated, reducing the energy barrier that could be overcome by the thermal activation. On the other hand, at higher power in adiabatic, temperature was enough to activate the reaction by thermal mechanism.

In addition to the increase of surface reactivity due to the lower energy barrier, the other effect that could improve the activity is the modification of the plasma characteristics due to the higher temperature attained. Under adiabatic conditions, the required applied voltage (V_{pk}) decreased and the discharge transfer per half cycle increased (**Appendix D.2, Figure D.5**) compared to pseudo-adiabatic configuration, meaning that the amount of high energetic electrons increased together with the number of ionized CO_2 molecules. Thus, the plasma characteristics have a direct impact on the conversion of CO_2 .

5.3.2 Gas flowrate effect

In the previous section, it was revealed that power can be reduced in adiabatic configuration due to synergy between plasma and thermal activation. Higher conversion was obtained at low power, caused by the higher reactor temperature in adiabatic configuration.

In view of these results, heat management can improve the energy efficiency by reducing the applied power. Thus, another way to control the heat released is by adjusting the amount of moles introduced into the reactor. In a first step, the influence of GHSV in pseudo-adiabatic reactor was explored by varying the inlet flowrate.

Figure 5.5 displays the temperature obtained as function of the applied power at different GHSVs in pseudo-adiabatic configuration. The temperature pattern showed two regions in all CO_2/H_2 conditions. At low power (< 10 W), temperatures were independent of the flow rate since the heat released was mainly caused by the plasma discharges. The temperature pattern was altered at higher power (> 10 W) due to the additional heat released by the exothermic reaction (as seen in previous sections). The temperature reached at medium to high power was noticeably dependent on the GHSV. In a way that the temperature was increased from 140 °C to 225 °C at 25 W once the flow was 5-fold increased ($40,000$ to $140,000$ $\text{mL}\cdot\text{h}^{-1}\cdot\text{g}^{-1}$). The dependence of the temperature on the GHSV was a direct consequence of the higher number of CO_2 moles converted to methane (-165 $\text{kJ}\cdot\text{mol}^{-1}$ CO_2).

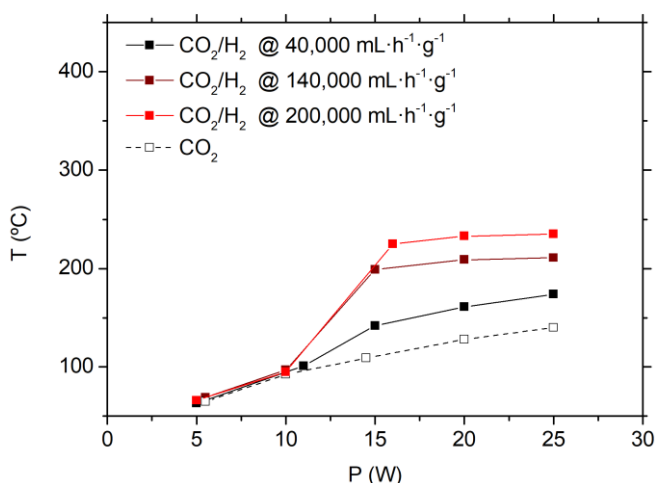


Figure 5.5. Temperature versus power using different CO_2/H_2 flows in pseudo-adiabatic configuration.

Regarding the catalytic performance, the conversion as function of the GHSV was analyzed at two constant plasma power (**Figure 5.6**). The selected power corresponds with two opposite conditions; the ignition point (15 W), where the reaction arises, and the maximum conversion point (25 W). At 25 W, the conversions tended to decrease as a function of the flow, from 74.4% at $40,000$ $\text{mL}\cdot\text{h}^{-1}\cdot\text{g}^{-1}$ to 64.8% at

140,000 mL·h⁻¹·g⁻¹. Conversely, the absolute number of CO₂ converted was increased from 0.5 mol·h⁻¹ to 1.7 mol·h⁻¹. As consequence, the released heat from the reaction was increased from 12.4 kJ·h⁻¹ (3.6 W) to 39.6 kJ·h⁻¹ (11 W), increasing the temperature (as seen in **Figure 5.5**). In overall, the reaction has a higher methane productivity rate at higher GHSV and temperatures, although there is a 10% of conversion drop.

A different conversion pattern was observed at 15 W. Conversion sharply increased from 30% at 40,000 mL·h⁻¹·g⁻¹ to 72.5% at 140,000 mL·h⁻¹·g⁻¹; and beyond this point, conversion started to decrease with the GHSV. The initial rise in the activity was a direct consequence of the higher temperature reached in the catalytic bed when the amount of reactants increased. In a similar way to previous results in adiabatic configuration, conversion increased due to the synergic between plasma and thermal activation. In the case of 25 W, conversion could not be improved as the maximum conversion for the given working conditions was already reached.

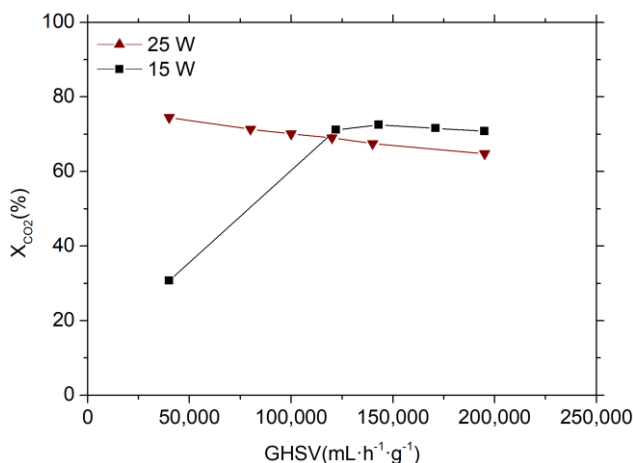


Figure 5.6. CO₂ conversions versus GHSV at constant applied power in pseudo-adiabatic configuration.

5.3.3 Adiabatic configuration at high GHSV

In view of the previous results, adiabatic experiments were performed at the optimum GHSV of 140,000 mL·h⁻¹·g⁻¹, which corresponds to 700 mL·min⁻¹ of CO₂/H₂. At a GHSV of 200,000 mL·h⁻¹·g⁻¹, the temperature under adiabatic conditions rises above 400 °C and it was not considered due to their low conversion rate and selectivity.

In **Figure 5.7**, the temperature obtained in the adiabatic conditions is compared with pseudo-adiabatic operation. A remarkable sharp increase of temperature was observed between 8 and 9 W, at the highest GHSV, which was much higher than the one obtained in the previous conditions. In a way that the temperature increased by 2-fold, from 150 °C to 365 °C. This substantial increase in temperature displaced the

desired conversions to much lower power. The consequences of this temperature rise are shown in **Figure 5.8**. Conversion reached 70% at a power input as low as 8.5 W. Unfortunately, the conversion value was slightly lower than the one obtained in pseudo-adiabatic conditions. In this condition, the excess in temperature started to play an important role in the conversion, related to the selectivity (**Figure 5.9**). A significant decrease in the selectivity was observed at high power, as secondary reactions (namely CO formation by RWGS) were favoured at higher temperatures. In view of these results, a suitable control of temperature seems mandatory to obtain the optimum conditions at the lowest power. In principle, adiabatic configuration improved

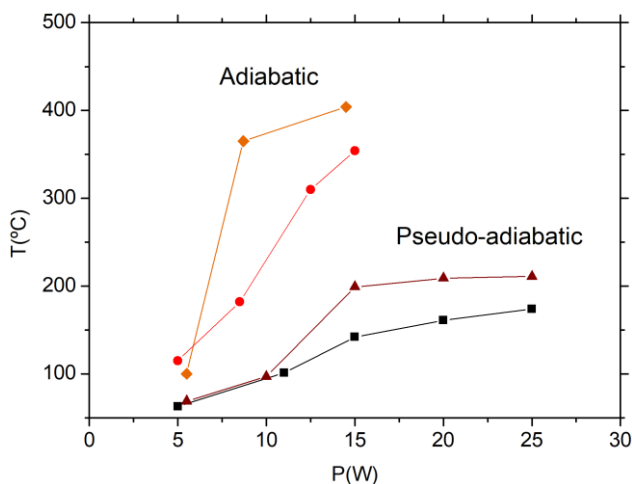


Figure 5.7. Temperature versus power using different CO_2/H_2 flows in adiabatic DBD. (▲) Pseudo-adiabatic @ $140,000 \text{ mL}\cdot\text{h}^{-1}\cdot\text{g}^{-1}$, (■) Pseudo-adiabatic @ $40,000 \text{ mL}\cdot\text{h}^{-1}\cdot\text{g}^{-1}$, (♦) Adiabatic @ $140,000 \text{ mL}\cdot\text{h}^{-1}\cdot\text{g}^{-1}$ and (●) Adiabatic @ $40,000 \text{ mL}\cdot\text{h}^{-1}\cdot\text{g}^{-1}$.

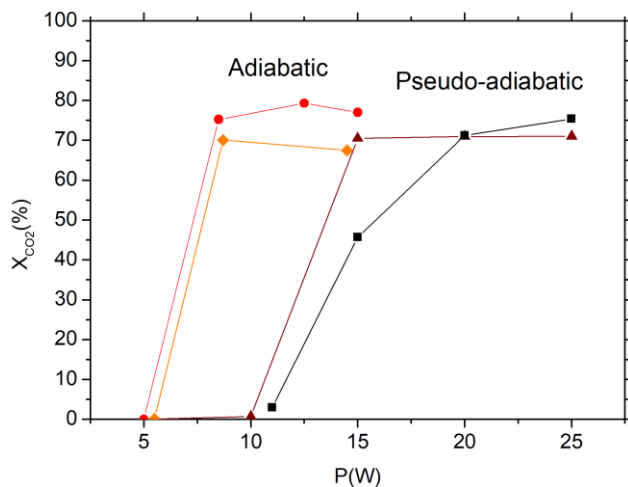


Figure 5.8. CO_2 conversion versus power (▲) Pseudo-adiabatic @ $140,000 \text{ mL}\cdot\text{h}^{-1}\cdot\text{g}^{-1}$, (■) Pseudo-adiabatic @ $40,000 \text{ mL}\cdot\text{h}^{-1}\cdot\text{g}^{-1}$, (♦) Adiabatic @ $140,000 \text{ mL}\cdot\text{h}^{-1}\cdot\text{g}^{-1}$ and (●) Adiabatic @ $40,000 \text{ mL}\cdot\text{h}^{-1}\cdot\text{g}^{-1}$.

the efficiency of the process. Nonetheless, uncontrolled high temperatures can also cutback the conversion and displace the selectivity to CO.

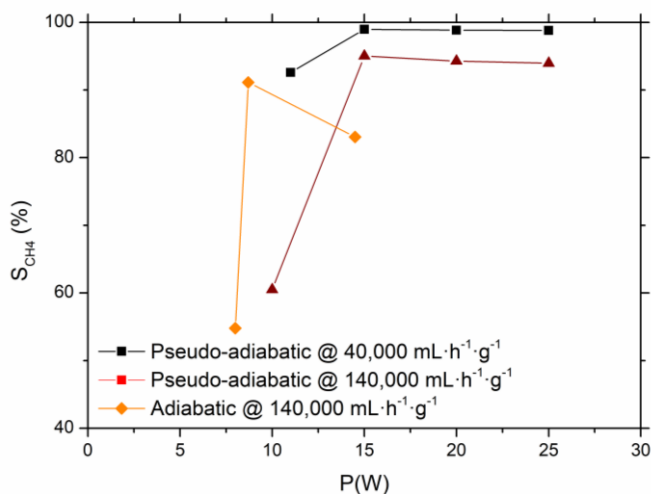


Figure 5.9. CH₄ selectivity vs power for adiabatic and pseudo-adiabatic at different GHSV.

5.4 Energy efficiency

In this last section, the energy efficiency of all configurations studied in the previous sections are compared in **Figure 5.10**. Different effects and improvements can be observed.

First, comparing the results done at low GHSV (40,000 mL·h⁻¹·g⁻¹), the maximum efficiency was increased by 20% (40 to 60%) using an adiabatic DBD plasma reactor compared with pseudo-adiabatic configuration (**section 5.3.1**, pseudo vs adiabatic). The effect was caused by the lower power requirements in comparison with the pseudo-adiabatic DBD reactor. None of the configurations reached the theoretical maximum efficiency at each SEI (**Figure 5.10**, dotted line), as conversion values were maintained below 80%. In this sense, the highest efficiency obtained in adiabatic was 58% (at 62 kJ·mol⁻¹) with a conversion value of 75%.

Second, comparing the results obtained in pseudo-adiabatic configuration with different GHSV (**section 5.3.2**), an improvement in the efficiency was obtained at higher GHSV. Thus, the increase in the GHSV boosted the efficiency to a relevant 67%, in comparison with the 40% at low GHSV values. The higher energy efficiency was the result of the reduction in SEI values, which was led by two factors. On the one hand, the displacement of the optimal conversion to lower power, as seen in **section 5.3.1**. On the other hand, the increase of GHSV led to a reduction of SEI values as the applied power remained constant while the flow rate was increased.

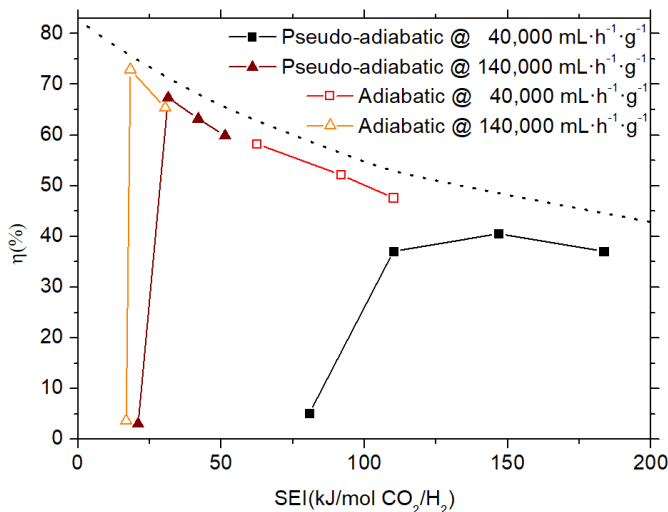


Figure 5.10. Energy efficiency comparison between the different configurations as function of SEI, dotted line corresponds to 100% CO₂ conversion.

Finally, the highest energy efficiency was obtained in adiabatic configuration at the highest GHSV (**section 5.3.3**), with an energy efficiency of 73%. Therefore, the efficiency of the process was almost doubled by adjusting gas flow rates and reactor configuration (adiabatic). This result represents a significant improvement compared with the conventional pseudo-adiabatic conditions (40% of efficiency).

A summary of all conditions can be found in **Table 5.1**, together with the results obtained by other groups. The energy efficiency from other publications has been calculated using the reported data (conversion, applied power, and space velocity). In the pseudo-adiabatic configuration used in **chapter 3**, the maximum efficiency obtained was below 40%. As seen in **chapter 4**, the optimization of the catalyst positively influenced the energy efficiency. The development of more active catalysts boosted the energy efficiency from 27 to 36%. Thus, the use of different catalysts should be considered in order to compare the different approaches. Recent work by M. Mikhail et al. [9] showed a similar trend; they obtained 51% of energy efficiency working at pseudo-adiabatic conditions (270 °C) on a 15 wt% Ni-Ce_{0.58}Zr_{0.42}O₂ catalyst. R. Benrabbah et al. [6] used the same catalyst formulation and they presented interesting efficiency values. They achieved 69% of energy efficiency in apparently pseudo-adiabatic conditions (120 °C). The high-efficiency values derive from the exceptional low plasma power (4 W). The different plasma setup configurations could be the cause of the less power demand. Therefore, there is room for plasma reactor improvement; signal frequency, electrode material, space between electrodes [1,10], as well as catalyst material development for CO₂ plasma-catalysis application.

In addition, following the strategy proposed in this chapter, the efficiency of the plasma catalytic reactor could be compared with the thermal methanation setup. The estimated power consumption in a similar thermal reactor would be 4–15 W,

depending on the GHSV, considering that the gas should be heated up to temperatures where the catalyst is active (350 °C for Ni-Ce catalyst). The theoretical power required to heat the gases can be calculated considering similar conditions (GHSV) and the efficiency of the reactor heater (the details of the calculation can be found in **Appendix D.3**). In this sense, the plasma methanation could be competitive and the application of adiabatic setups could lower the energy demand, increasing the efficiency.

In this chapter, we have demonstrated that the heat management of the plasma reactor is crucial for the viability of the CO₂ methanation by plasma technology. Besides, an accurate control of the temperature seems mandatory to work at the optimum conditions that can be achieved by adjusting the GHSV parameter, rather than using an external heater. Using our approach, it was possible to propose a highly intensive process able to work at a high yield ($\sim 800 \text{ mmol}_{\text{CH}_4} \cdot \text{h}^{-1} \cdot \text{g}^{-1}$) with the lowest energy cost reported.

Table 5.1. Summary of results for adiabatic and pseudo-adiabatic and similar reactor configurations from literature.

	GHSV ($\text{mL} \cdot \text{h}^{-1} \cdot \text{g}^{-1}$)	η (%)	X (%)	r_{CH_4} ($\text{mmol} \cdot \text{h}^{-1} \cdot \text{g}^{-1}$)	SEI ($\text{kJ} \cdot \text{mol}^{-1}$)	EC ($\text{kJ} \cdot \text{mol}^{-1}$)	T (°C)	Ref.	
Pseudo-adiabatic	40,000	40	71	233	146	1031	161	Chap. 5	
	140,000	67	70	808	31	234	200		
Adiabatic	40,000	58	75	246	62	413	182		
	140,000	73	70	802	18	130	365		
Pseudo-adiabatic	40,000	37	75	246	183	1220	150		Chap. 3
	40,000	51	71	232	87	618	270		[9]
	40,000	69	73	238	29	200	120	[6]	

5.5 Conclusions

Hybrid plasma-catalytic CO₂ methanation was evaluated on two reactor approaches employing a Ni-Ce catalyst supported on alumina. Pseudo-adiabatic and adiabatic configurations were studied without any type of external heating. It was observed that plasma discharge and methanation reaction acts as heating sources that increase the reactor temperature up to 150 °C in conventional pseudo-adiabatic conditions. By thermally insulating the reactor, the temperature was sharply increased up to 350 °C as adiabatic conditions were reached. The plasma power in adiabatic reactor configuration was reduced by 10 W to get similar conversion values. CO₂ was successfully converted to CH₄ in these conditions, as the reaction was activated by both methods; plasma and thermal. The lower power consumption under adiabatic conditions increased the energy efficiency by 20% due to the synergy effects.

Additionally, it has been demonstrated that the heat released by the methanation reaction can be controlled by varying the GHSV. In this way, reactor temperature increases at higher GHSV and reduces the power consumption. The optimum GHSV was studied in adiabatic conditions. The temperature increased up to 350 °C while the power was reduced up to 8.5 W (SEI reduced to 18 kJ·mol⁻¹ compared with 146 kJ·mol⁻¹ used in the pseudo-adiabatic conditions at low GHSV), reaching an energy efficiency of 73%.

In summary, working at adiabatic conditions was found to be energetically less demanding due to synergetic effects between plasma and thermal activation. The precise control of the heat has been found to be mandatory in hybrid plasma catalytic CO₂ methanation to maximize the energy efficiency of the overall process.

5.6 References

- [1] N. Jidenko, E. Bourgeois, J.-P. Borra, Temperature profiles in filamentary dielectric barrier discharges at atmospheric pressure, *J. Phys. D. Appl. Phys.* 43 (2010) 295203. doi:10.1088/0022-3727/43/29/295203.
- [2] T.H. T. Kappes, W. Schiene, Energy balance of a dielectric barrier discharge reactor for hydrocarbon steam reforming, in: 8th Int. Symp. High Press. Low Temp. Plasma Chemistry Proceedings, HAKONE, 2002: p. 5.
- [3] T. Hammer, T. Kappes, M. Baldauf, Plasma catalytic hybrid processes: gas discharge initiation and plasma activation of catalytic processes, *Catal. Today*. 89 (2004) 5–14. doi:10.1016/j.cattod.2003.11.001.
- [4] M. Alliat, D. Mei, X. Tu, Plasma activation of CO₂ in a dielectric barrier discharge: A chemical kinetic model from the microdischarge to the reactor scales, *J. CO₂ Util.* 27 (2018) 308–319. doi:10.1016/j.jcou.2018.07.018.
- [5] M. Nizio, R. Benrabbah, M. Krzak, R. Debek, M. Motak, S. Cavadias, M.E. Gálvez, P. Da Costa, Low temperature hybrid plasma-catalytic methanation over Ni-Ce-Zr hydrotalcite-derived catalysts, *Catal. Commun.* 83 (2016) 14–17. doi:10.1016/j.catcom.2016.04.023.
- [6] R. Benrabbah, C. Cavaniol, H. Liu, S. Ognier, S. Cavadias, M.E. Gálvez, P. Da Costa, Plasma DBD activated ceria-zirconia-promoted Ni-catalysts for plasma catalytic CO₂ hydrogenation at low temperature, *Catal. Commun.* 89 (2017) 73–76. doi:10.1016/j.catcom.2016.10.028.
- [7] C. De Bie, J. van Dijk, A. Bogaerts, CO₂ Hydrogenation in a Dielectric Barrier Discharge Plasma Revealed, *J. Phys. Chem. C*. 120 (2016) 25210–25224. doi:10.1021/acs.jpcc.6b07639.
- [8] J. Kim, D.B. Go, J.C. Hicks, Synergistic effects of plasma–catalyst interactions for CH₄ activation, *Phys. Chem. Chem. Phys.* 19 (2017) 13010–13021. doi:10.1039/C7CP01322A.
- [9] M. Mikhail, B. Wang, R. Jalain, S. Cavadias, M. Tatoulian, S. Ognier, M.E. Gálvez, P. Da Costa, Plasma-catalytic hybrid process for CO₂ methanation: optimization of operation parameters, *React. Kinet. Mech. Catal.* 126 (2019) 629–643. doi:10.1007/s11144-018-1508-8.
- [10] A. Ozkan, T. Dufour, T. Silva, N. Britun, R. Snyders, A. Bogaerts, F. Reniers, The influence of power and frequency on the filamentary behavior of a flowing DBD—application to the splitting of CO₂, *Plasma Sources Sci. Technol.* 25 (2016) 025013. doi:10.1088/0963-0252/25/2/025013.

Chapter 6

Plasma ignition and autothermal operation

The results presented in chapter 6 have been submitted to Chemical Engineering Journal and are under revision at the moment of finishing the thesis.

6.1 Introduction

This chapter is devoted to developing a new DBD reactor configuration and a novel strategy using a hybrid DBD-thermo-catalytic reactor. DBD-plasma is used as reaction ignitor, rather than the classical approach of continuous operation, by taking advantage of the synergy between catalytic plasma activation from room temperature and a self-sustained exothermic reaction.

As seen in **chapter 5**, the heat released by the methanation reaction in adiabatic conditions can increase the temperature up to values where the catalyst is thermally active. Based on these results, we proposed a novel strategy; the use of DBD-plasma as ignitor to initiate the reaction, increasing temperature to activate the catalyst and achieving a self-sustained reaction in autothermal conditions.

In order to obtain the best performance, a new reactor configuration was used. The hybrid DBD-thermo-catalytic reactor was based on the adiabatic reactor used in **chapter 5**, with the incorporation of an additional catalytic bed (outside the plasma region, without electrodes). The additional bed allowed to obtain higher conversion and selectivity at higher GHSV.

Thus, the novel strategy is based on using the DBD-plasma as ignitor to initiate the chemical reaction in adiabatic conditions and take advantage of the heat released due to the exothermic methanation reaction to warm up the subsequent sections of the reactor up to a temperature where the catalyst is thermally active (**section 6.3.1**). After ignition, plasma was turned off and the specific conditions to obtain autothermal operation after ignition was studied (**section 6.3.2**). Finally, the ignition procedure was optimized, reducing the energy consumption and the start-up times (**section 6.3.3**). In this way, the use of DBD plasma as reaction ignitor opens the path to electrify chemical reactions while minimizing the start-up time to avoid the classical reactor warm-up under standby conditions.

In summary, the main objectives of this chapter are:

- Proof-of-concept of the use of plasma to ignite the CO₂ methanation reaction in an adiabatic reactor.
- Investigate the viability of autothermal reactor after plasma ignition.
- Reduce to the minimum the energy cost.
- Increase conversion and selectivity by increasing the amount of catalyst in a secondary bed and working at high gas flow.

6.2 Experimental setup: hybrid DBD adiabatic reactor

The reactor used in this chapter is based on the adiabatic configuration used in **chapter 5**, but with an additional catalyst bed. Thus, the hybrid reactor consisted in two sections; the first section, DBD plasma activation, included integrated electrodes, whereas the second section, thermal-catalysis, did not include external power or heating devices (**Figure 6.1**).

The catalyst used was the same as in chapter 5, Ni-Ce catalyst synthesised by WET impregnation (30Ce-15Ni WET). In the new hybrid reactor setup, a total amount of 0.9 g of catalyst was placed in the reactor. As explained, the catalyst was divided into two beds. The first 0.3 g was placed in the zone where the plasma was generated (first catalyst bed, same configuration as **chapter 5**). The remained 0.6 g were placed just after, in the second catalyst bed, only separated by a small quantity of quartz wool from the first bed (<2 mm). The separation between catalytic beds ensured that the latest section was not activated by plasma.

Compared with the setup used in **chapter 5**, an additional thermocouple was used to monitor the temperature in the catalyst bed (**Figure 6.1**). Thus, temperature in the first section (plasma) was measured by a thermocouple in contact with the external electrode (T1). Temperature in the second section (thermal) was measured inside the reactor at the end of the catalyst bed (T2).

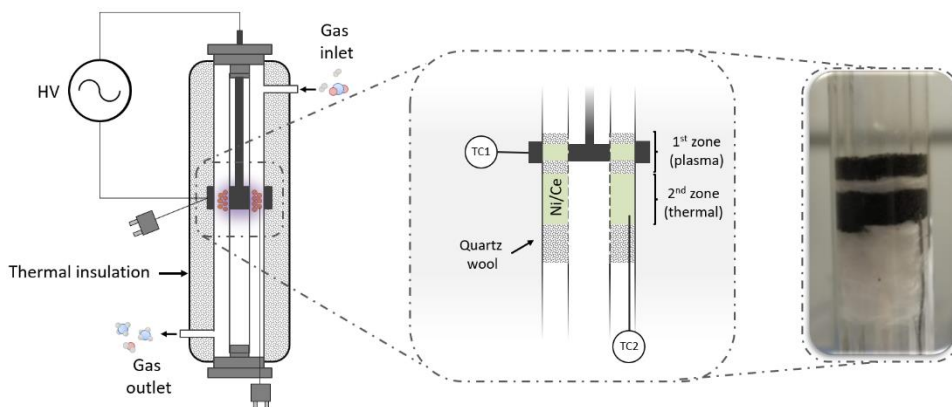


Figure 6.1. Scheme of the hybrid DBD-thermo-catalytic adiabatic reactor.

6.3 Results

6.3.1 Plasma ignition

The hybrid DBD-thermal-catalysis reactor was evaluated for CO₂ methanation reaction by applying different plasma power over time at the DBD plasma ignition section. Gases were introduced to the reactor at room temperature, being the electrical plasma activation and the heat released from the methanation reaction the sole energy inputs.

The experiments were carried out in three consecutive stages at different plasma power inputs, as seen in the scheme of **Figure 6.2**. First, plasma power was increased gradually in sequential steps (1). Second, the plasma power was decreased step-by-step (2). Third, in the last stage, the plasma was switched off (3). These three stages are marked as 1, 2 and 3 on the results figures (**Figure 6.3**). **Figure 6.3a** shows the temperature profile versus time during the experiment, being T1 the temperature in the plasma activated zone and T2 the second catalyst bed section. In **Figure 6.3b**, the obtained CO₂ conversion is represented for the same experiment, performed with a low gas flow of 200 mL·min⁻¹ of CO₂/H₂, corresponding to a GHSV of 13,333 mL·g⁻¹·h⁻¹.

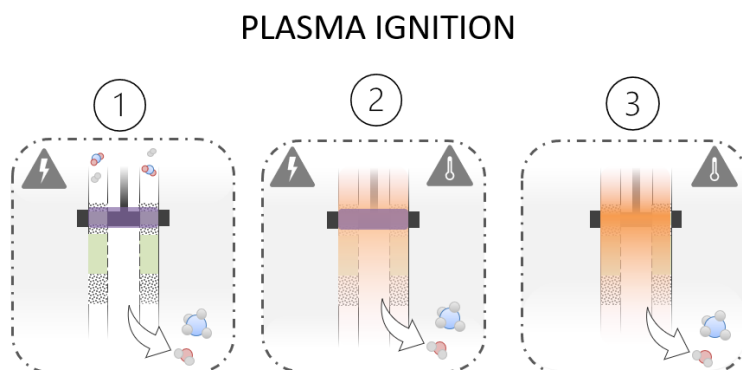


Figure 6.2. Experimental procedure. (1) Plasma activation. (2) Plasma power decrease and temperature increase (exothermicity). (3) Plasma switched off (autothermal).

As it can be seen, during the first stage, the methanation reaction started at 7 W (**Figure 6.3a**) and at a temperature around 170 °C (**Figure 6.3b**). Immediately after, the temperature drastically increased due to the heat released by the methanation reaction, reaching a temperature of 285 °C with a CO₂ conversion of 78% and 99% selectivity to methane. Power was further increased up to 10 W to obtain higher reactor temperature, where the catalyst could be more active by thermal-catalytic routes (350-400 °C). At this power, the temperature reached 360 °C at 10 W while conversion slightly increased to 84 %. The temperature measured at the end of the second bed (T2) was always lower than in the plasma zone, indicating that there was a temperature gradient of 30-40°C in the reactor. Therefore, a temperature gradient

from 370 °C to 325 °C was obtained along the length of the catalyst bed. At these temperatures, the catalyst could be active by thermal route (as seen in **chapter 5**) in the first and second catalyst bed.

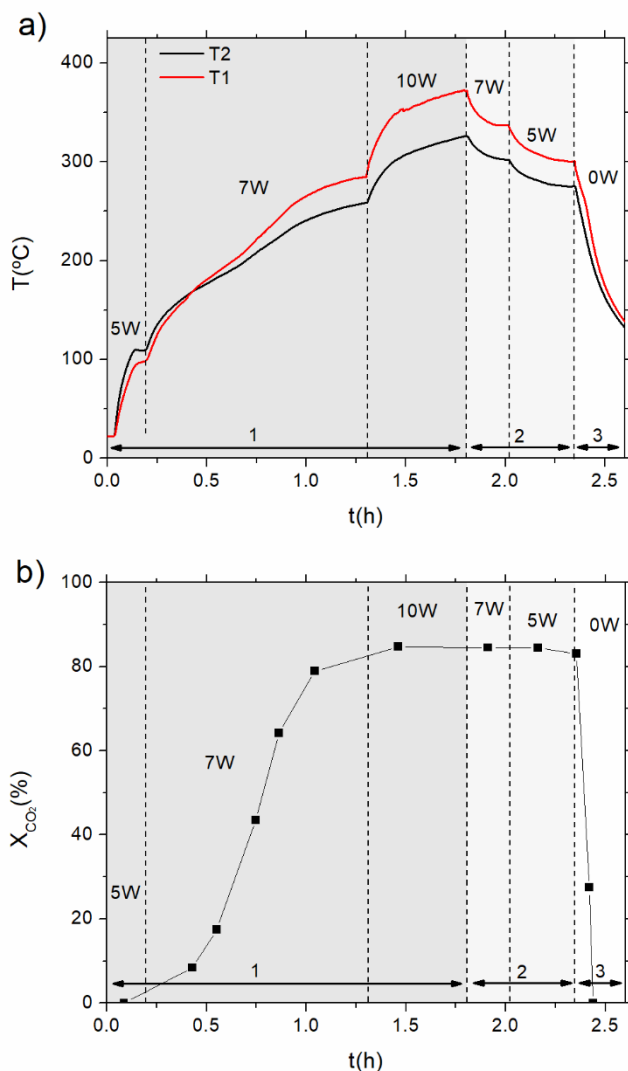


Figure 6.3. Plasma ignition experiments at a GHSV of $13,333 \text{ mL}\cdot\text{g}^{-1}\cdot\text{h}^{-1}$. **a)** Reactor temperature in the two sections of the reactor: plasma catalytic (T1) and catalytic bed (T2). **b)** CO₂ conversion values. Applied plasma power is indicated in the figure.

In the second stage, power was reduced in steps; from 10 to 7 W and from 7 to 5 W. Consequently, temperature decreased to 335 °C at 7 W and 300 °C at 5 W, while conversion and selectivity were practically unchanged. Compared with only thermal activation, higher conversion was obtained at 300 °C (results obtained in **chapter 5**) due to the synergy of plasma and thermal catalysis.

In the last stage, the power was completely stopped, conversion and temperature started to drop until the reaction was extinguished entirely. Therefore, the heat released by the methanation reaction was not sufficient to maintain the reaction at $13,333 \text{ mL}\cdot\text{g}^{-1}\cdot\text{h}^{-1}$.

In summary, experimental results inferred that DBD plasma section was capable to initiate the chemical reaction and to increase the temperature of the reactor. As explained in previous chapter, the plasma activates the reaction at low temperature due to the formation of reactive species. After plasma ignition, the temperature was significantly increased due to the heat released by the methanation reaction. Furthermore, under the conditions achieved, the catalyst was active in the second section of the reactor, as heat released by the methanation reaction increased temperature above $300 \text{ }^\circ\text{C}$. Thus, synergies between the different reactor zones were successfully validated. The reaction can be ignited only using the first part of the reactor, increasing reactor temperature and activating the second catalyst bed, which boosts conversion values. However, reaction stopped as soon as the plasma was shut-off due to the heat released by the reaction was not enough to self-sustain the system, suggesting that, at those conditions, plasma power could be reduced but not avoided.

The plasma ignition experiments showed that during plasma operation, the benefits were the reduction of the power after the activation of the thermal bed and the synergy between plasma and thermal activation. In the best conditions, the energy consumption was reduced by 30% compared to solely plasma-catalysis (from 7 W to 5 W) with an energy cost of $219 \text{ kJ}\cdot\text{mol}_{\text{CH}_4}^{-1}$, which corresponds to an energy efficiency of 68 %.

6.3.2 Autothermal operation

In view of the previous results, higher amount of heat is required to self-sustain the reaction without external power. For a gas flow of $600 \text{ mL}\cdot\text{min}^{-1}$ (GHSV of $40,000 \text{ mL}\cdot\text{g}^{-1}\cdot\text{h}^{-1}$) results followed a similar initial trend, the reaction started at 7 W with temperature close to $170 \text{ }^\circ\text{C}$ (**Figure 6.4a** and **Figure 6.4b**). However, as the reaction took place, the temperature rose up to $450 \text{ }^\circ\text{C}$, with a notable difference of almost $200 \text{ }^\circ\text{C}$ more than the results obtained at $200 \text{ mL}\cdot\text{min}^{-1}$. A direct relation of temperature with the total gas flow was observed, as the heat released by the methanation increased proportionally to the gas flow. The results follow the same trend as previous publications in thermal CO_2 methanation [1] and CO_2 plasma methanation [2], where higher reactor temperatures are obtained at higher gas flow. In this case, a temperature gradient from $450 \text{ }^\circ\text{C}$ to $330 \text{ }^\circ\text{C}$ was achieved along the reactor (T1 and T2). Regarding the activity values, 76% of conversion and 99% of selectivity were obtained.

In the second stage, temperatures started to decrease when the power was reduced due to less heat was generated by the plasma. For 6 W, 4 W and 2 W, stable

conditions with 79-78% of conversion and temperature higher than 350 °C were obtained. Finally, the applied plasma power was completely stopped and the temperature was stabilized at 337 °C with 77% conversion and 99% selectivity. The reactor temperature was maintained between 337 and 270 °C along the reactor (T1 and T2). Remarkably, self-sustained conditions were obtained for more than 1 hour without any external energy input since the heat generated by the reaction was enough to keep the reactor temperature. Therefore, the concept of using DBD plasma as reactor ignitor was experimentally validated at those specific conditions of gas flow

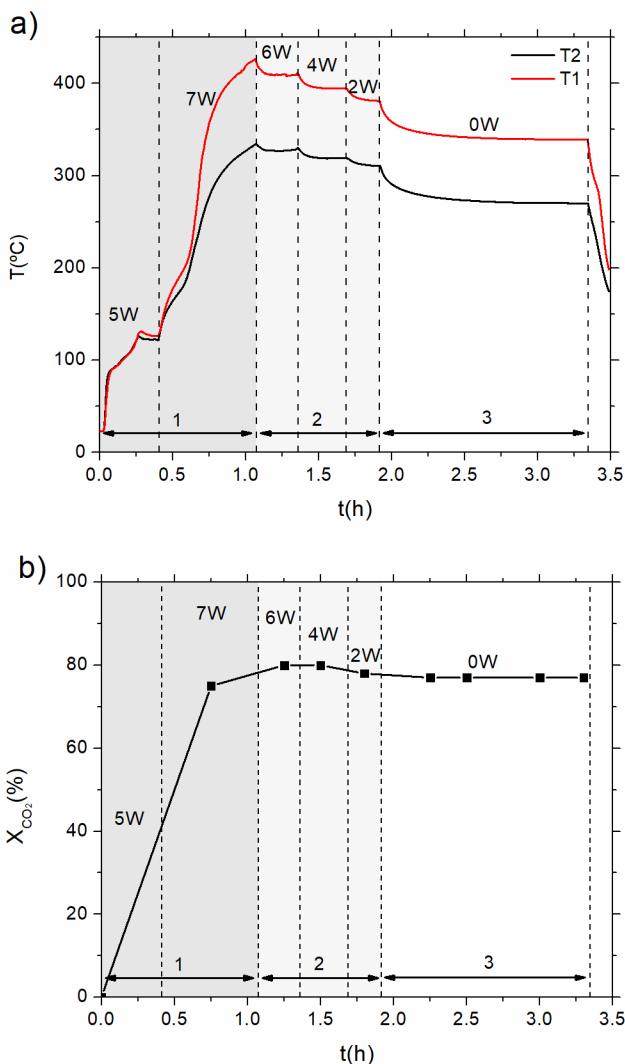


Figure 6.4. Plasma ignition experiments at a GHSV of 13,333 mL·g⁻¹·h⁻¹. **a)** Reactor temperature in the two sections of the reactor: plasma catalytic (T1) and catalytic bed (T2). **b)** CO₂ conversion values. Applied plasma power is indicated in the figure.

rate. From these experiments, it is inferred that the amount of gas flow rate, and therefore the amount of heat released, should be adjusted to balance heat losses in the present device.

After one hour, the reaction was intentionally stopped decreasing the gas flow from 600 to 200 mL·min⁻¹, resulting in the reactor cooling. The temperature was dropped by the lower amount of heat released and, consequently, the conversion stopped in line with the previous experiment. The employed cool-down procedure also demonstrated that a minimum flow of CO₂/H₂ is needed to work in autothermal conditions.

The limitation of the gas flow to obtain autothermal methanation was further confirmed by a complementary experiment performed with a gas flow of 400 mL·min⁻¹ (**Appendix E.1, Figure E.1**). Self-sustained conditions were not obtained in this case after the plasma was shut-down. Therefore, using a 600 mL·min⁻¹ flow seems to be adequate to reach the self-sustained condition in our reactor. On the other hand, working at even higher flow (900 mL·min⁻¹ - 60,000 mL·g⁻¹·h⁻¹) autothermal condition was achieved (**Appendix E.1, Figure E.2**), but despite higher temperature obtained (390 °C) it was difficult to achieve a stable temperature after 1 hour since the reactor was warming up at a rate of 0.3 °C·min⁻¹. Under these conditions, a cooling element will be needed to achieve a continuous operation, which is out of the scope of this work. In view of these results, autothermal conditions are highly dependent on the gas flow, with a specific minimum flow. The gas flow increases the only source of heat to the system (reaction). The ratio between the heat source (reaction) and heat losses (gas heating and reactor heat losses) needs to be adjusted to obtain the optimum temperature range to perform the reaction in autothermal conditions. Therefore, it has

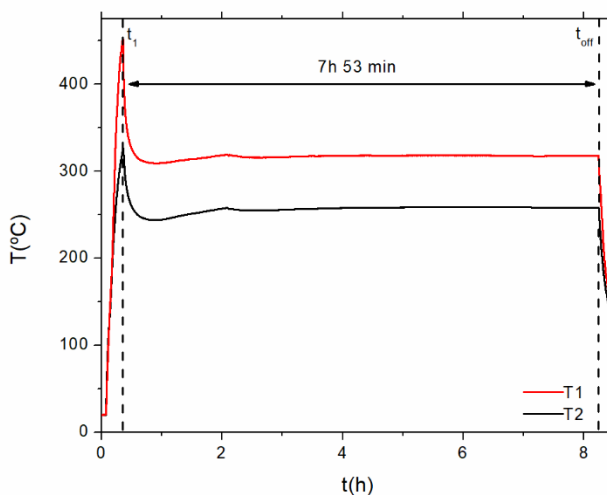


Figure 6.5. Autothermal experiments at GHSV of 40,000 mL·g⁻¹·h⁻¹ during ~ 8 h, from t_1 to t_{off} (cool-down).

been demonstrated that the reactor temperature and conversion can be adjusted by varying the total inlet gas flow in autothermal conditions.

The stability of autothermal methanation after plasma ignition was validated with a long-time experiment. **Figure 6.5** shows the temperature obtained during the experiment. The reaction was ignited at 10 W of applied plasma power until reaching 450 °C and just after the plasma was turned off (t_1). The autothermal condition was achieved for almost 8 hours of continuous operation. The conversions were stabled during the self-sustained operation with CO₂ conversion values near 76-77 % and a selectivity of 99 %. In autothermal conditions, the energy efficiency reached the maximum value of 83%, as the energy cost was reduced to zero. After 8 hours, the reaction was intentionally stopped by decreasing the CO₂/H₂ flow (t_{off}). This proof-of-concept experiment demonstrated the feasibility of continuous autothermal operation after the plasma ignition.

6.3.3 Fast and efficient operation

In the previous section, plasma has been presented as an ignitor, demonstrating the possibility to obtain self-sustained methanation in autothermal conditions. The use of plasma as an ignitor could be an efficient process if start-up time and power are low enough. In this section, the optimization of energy consumption and start-up time is presented. The experiments were done at the optimum GHSV of 40,000 mL·g⁻¹·h⁻¹, which was needed to work under autothermal conditions. The following experiments were done in one step ignition at constant power during the minimum time required to activate the reaction and reach temperature to assure that the reaction was self-sustained. Thus, 450 °C was set as a target to ensure that reaction could be continued by thermal-catalysis and to avoid thermal degradation of the catalyst ($T > 450$ °C).

Figure 6.6 shows the results obtained applying 7 W, 10 W and 15 W. The results were similar to those of the previous section, starting conversion at a temperature below 200 °C. For the lowest power (7 W) almost more than 20 minutes (t_0) were needed to get higher conversions ($X_{CO_2} > 70\%$). In addition, the higher temperature required to maintain the autothermal conditions were not reached in less than 40 minutes (t_1). At this time, plasma was shut-off (t_1) and autothermal conditions were achieved. The experiment was finished at t_{off} by decreasing the inlet flow (in a similar way to the previous section).

In the case of 10 W, start-up time was reduced to 7.9 minutes and the power was stopped after 17 minutes (t_1). More importantly, the total energy required to activate the reaction was substantially reduced from 17.8 to 10.4 kJ, as less time was needed. Thus, a significant reduction in the start-up time and total energy was obtained by increasing the power supplied.

On the other hand, higher power was counterproductive to obtain self-sustained conditions in one activation step. For 15 W, autothermal conditions were initially achieved for 20 minutes after plasma shut-off. However, conditions were not stable;

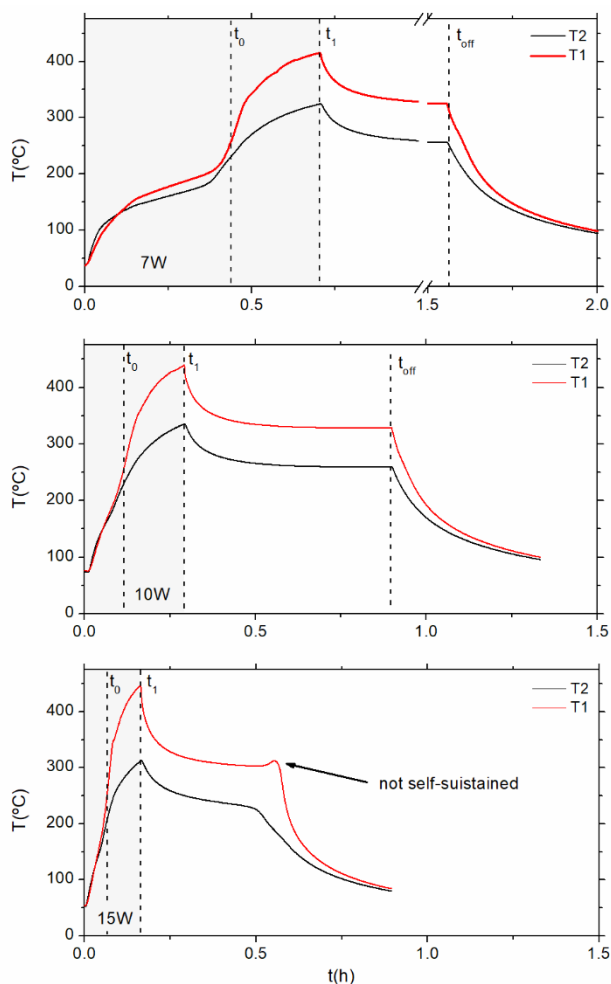


Figure 6.6. Experiments done at GHSV of $40,000 \text{ mL}\cdot\text{g}^{-1}\cdot\text{h}^{-1}$ for three different applied power 7, 10 and 15 W. t_0 is the start-up time ($X \sim 70\%$), t_1 is the plasma shut-off time and t_{off} are the cool-down time.

the temperature was continuously decreasing, and reaction was no longer self-sustained after 20 minutes. At this point, it was observed a drastic drop in temperature as conversion dropped. Thus, the reaction heat could not maintain the reactor temperature. The negative feedback between temperature and conversion caused the reaction to shut-down (as temperature decreases, the conversion also drops, decreasing the released heat and, as a consequence, the temperature further decreases).

The temperature along the reactor, start-up time, plasma-off time and energy consumption for the three experiments are summarized in **Table 6.1**. A proportional decrease of t_0 , t_1 , E as a function of the applied power can be clearly observed. In addition, the difference of temperature along the reactor (ΔT) increased for a higher

Table 6.1. Summary of results of experiments done at different power.

P(W)	Start-up t_0 (min)	Plasma-off t_1 (min)	T1(°C) at t_1	T2(°C) at t_1	$\Delta T=T_1-T_2$ at t_1	E(kJ)
7	26.5	42.3	415	325	90	17.8
10	6.7	17.4	438	335	103	10.4
15	3.9	9.8	447	312	135	8.8

power. In fact, ΔT would be directly related to the limitation to achieve autothermal conditions at higher power (15W).

At the highest applied power, the overall reactor temperature was not sufficiently high when the power was stopped. This can be clearly observed in the second catalyst bed temperature (T2), where the values were lower than in the other cases. Just before plasma was shut-off ($t \sim t_1$), the reactor was hotter in the plasma zone, but colder in the other reactor zones (compared with the other cases, 7 W and 10 W). After plasma shut-off, temperature decreased faster as was dissipated faster to the colder zones. The final temperature ($t \sim 30$ minutes) was not sufficient to self-sustain the reaction.

This can be clearly seen at the temperature achieved during self-sustained conditions, just previous to the stop of the reaction (t_{off}). The temperature was considerably lower for 15 W compared to in 10 and 7 W (302 vs 328-325°C). Therefore, temperature was not enough to self-sustain the reaction during autothermal conditions at 15 W.

The limitation seems to be the reactor thermal inertia, as temperature at plasma zone increased too faster, but the overall reactor was colder. Consequently, the heat was dissipated to the rest of the reactor, decreasing the overall temperature during the autothermal operation.

Despite the results obtained and considering that the reactor inertia seems to be the limitation to obtain self-sustained conditions, a different approach can be applied to use higher power and decrease the start-up time. In this sense, we proposed to add a second step with a lower power after the first plasma ignition to maintain a higher temperature. In this way, the first ignition step would be done at higher power to obtain a faster start-up time, while a second plasma activation step would be done at lower power with the objective to ensure that temperature along the reactor was high enough to maintain the reaction.

2-steps experiments were done at 15 W and 20 W (**Appendix E.1, Figure E.3 and Figure E.4**). In terms of start-up time and energy, the best results were obtained for 20 W, with a second step applying 5 W for 8.5 minutes (**Figure 6.7**). A start-up time of only 3 minutes from cold conditions (25 °C) was obtained with a total energy consumption of 9.5 kJ (2.6 W·h).

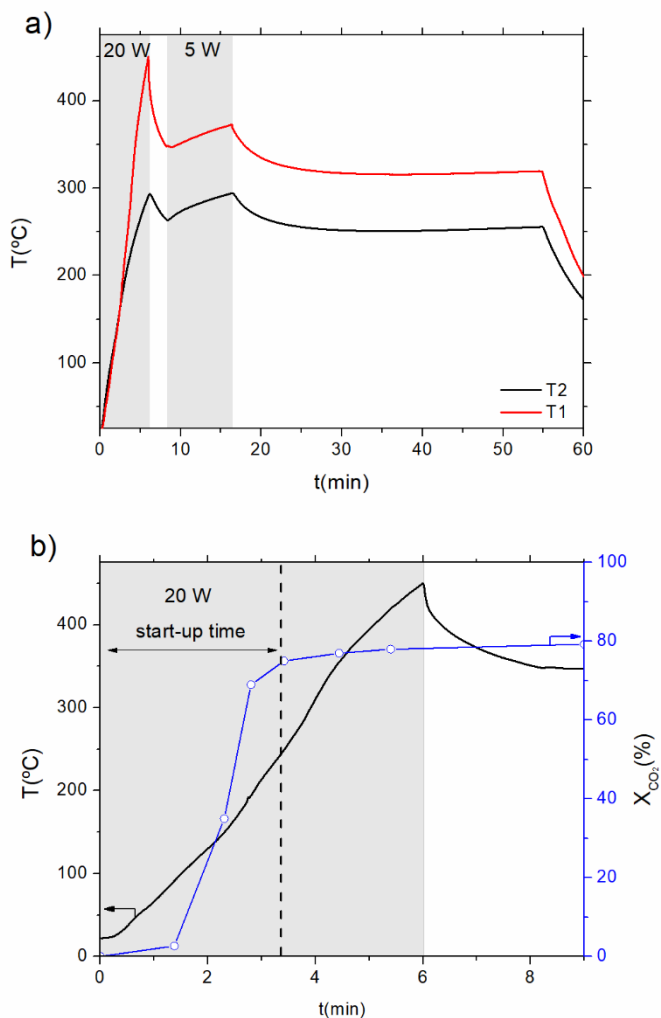


Figure 6.7. Experiments done at GHSV of 40,000 mL·g⁻¹·h⁻¹ applying 20 W and second step at 5W. **a)** Temperature vs. time. **b)** Temperature and conversion vs. time during the start-up.

6.4 Discussion

The presented hybrid plasma-thermo catalytic reactor allowed to ignite the reaction at lower temperature (170°C) due to the plasma activation of CO₂/H₂ into energetically reactive species. After plasma ignition, the temperature increased due to the heat released by the methanation reaction. The adiabatic configuration allowed to reach temperatures where the catalyst can be activated by thermal-catalysis. Thus, a second catalyst bed was activated, increasing the reactor performance. In the right conditions, reactions were self-sustained in autothermal operation after the plasma was shut-off.

The start-up time and energy consumption during plasma ignition have been optimized. Our results show extremely short times compared with thermal reactors,

which usually have higher start-up times when the reaction starts from cold conditions (30 minutes) [1]. Although most studies typically reported start-up time from warm or hot standby conditions, where reactors are kept at moderate temperatures (e.g. 250 °C). Faster times in the range of 3 to 30 minutes have been reported for start-up from warm conditions [1,3,4]. In comparison, plasma ignition showed a similar start-up time, but with the difference that no warm conditions or hot standby were required, simplifying the reactor engineering and energy consumption during standby.

On the other hand, the time obtained was sufficient to integrate with the other sub-systems of PtG, as electrolyzers. For example, commercial alkaline electrolyzers have a similar start-up time near 1-2 minutes. For other types of electrolyzers, such as polymer electrolyte membrane (PEM), faster start-up times in the range of second are reported [5], also leaving space for improvement of start-up in methanation units. The reduction in the start-up time is also important to decrease the hydrogen consumption during start-up, as generally, hydrogen is fed into the reactor to avoid carbon deposition during start-up and shut-down cycles [6].

In summary, by igniting the reaction with plasma, an extremely short start-up time was achieved facilitating the flexibility of this technology when coupled to a renewable energy source, reducing the inertia of thermal catalysis. Two main advantages arise from plasma ignition methanation. On the one hand, the low activation temperature in plasma-catalysis [7,8] (<200 °C) reduces the time to start the reaction. On the other hand, plasma heats the reactor up to 100-200 °C (without reaction). As part of the heat is produced directly in the gas by the plasma, the temperature can be increased faster and more efficiently than using external heaters. The presented methodology could also be applied to other exothermic reactions that are capable of operating under autothermal conditions.

Although the results show an interesting approach to combine plasma and thermal reactors, further research is necessary to obtain the required quality of the synthetic natural gas that could be injected into the gas grid (PtG tech.). The main limitation would be the low content of hydrogen allowed to be injected into the gas grid. The use of plasma as an ignitor or the entire combination of plasma and thermal reactor could help to achieve the requirements. In this regard and inspired in thermal reactor, work at higher pressure could increase the CH₄ yield. Recently, the effect of pressure in plasma methanation reaction was reported, where the slight increase in pressure did not negatively affect the plasma activation and higher conversion was obtained [9]. Exploring the limit of pressure in DBD are recommended. On the other hand, increasing the total conversion by combining reactors in series seems to be mandatory for plasma-catalysis, following a similar approach to thermal methanation [10]. The effect of the different gas composition, as CH₄, should be investigated in conventional plasma assisted and plasma ignition configuration. Once the required composition would be obtained, the scale-up should not be an impediment. The scale-up reactor could be implemented with multiple unit cells, in a multi-tubular configuration.

6.5 Conclusions

A new methodology of plasma CO₂ methanation was presented where plasma was used to ignite the reaction. Under this condition, a minimum GHSV of 40,000 mL·g⁻¹·h⁻¹ was found to be necessary in order to obtain autothermal conditions after plasma ignition. In autothermal operation, the reaction continued without any energy input (neither plasma nor external heating), only self-sustained by the own heat generated by the methanation reaction. Autothermal condition was demonstrated with a long-time experiment in which a stable condition was achieved for more than 8 hours. Finally, the activation conditions were optimized in order to reduce the total energy and obtain the faster start-up possible in our system. In the best conditions, a total energy consumption of 10.4 kJ was used to ignite to reaction in one step-ignition and obtaining autothermal conditions. Regarding start-up times, the faster ignition was achieved in two steps ignition with a remarkably fast time of only 3 minutes, starting from cold condition (25 °C) with an energy consumption of only 9.5 kJ. Thus, plasma ignition has been demonstrated to be an interesting option with faster start-up time and low energy consumption. In this regard, the main advantages to using plasma as ignition are: 1) the reduction of the threshold temperature in plasma methanation 2) faster heating as heat is generated inside the reactor due to plasma power losses. That permits to reduce start-up time from cold conditions up to 3 minutes which is a key factor when coupling a chemical reaction with electrical energy from intermittent renewable sources.

The concept herein demonstrated could be applied to other exothermic reactions, using plasma as an ignitor of reaction that could be self-sustained. On the other side, this methodology could be integrated into thermal reactor, accelerating the starting reaction by plasma that continues in thermal catalysis or a plasma-assisted thermal catalytic reactor. The result of the work could help to move towards the reactor electrification, improving the versatility and control of the reaction.

6.6 References

- [1] J. Guilera, T. Boeltken, F. Timm, I. Mallol, A. Alarcón, T. Andreu, Pushing the Limits of SNG Process Intensification: High GHSV Operation at Pilot Scale, *ACS Sustain. Chem. Eng.* 8 (2020) 8409–8418. doi:10.1021/acssuschemeng.0c02642.
- [2] B. Wang, M. Mikhail, M.E. Galvez, S. Cavadias, M. Tatoulian, P. Da Costa, S. Ognier, Coupling experiment and simulation analysis to investigate physical parameters of CO₂ methanation in a plasma-catalytic hybrid process, *Plasma Process. Polym.* 17 (2020) 1–11. doi:10.1002/ppap.201900261.
- [3] M. Gruber, P. Weinbrecht, L. Biffar, S. Harth, D. Trimis, J. Brabandt, O. Posdziech, R. Blumentritt, Power-to-Gas through thermal integration of high-temperature steam electrolysis and carbon dioxide methanation - Experimental results, *Fuel Process. Technol.* 181 (2018) 61–74. doi:10.1016/j.fuproc.2018.09.003.
- [4] C. Dannesboe, J.B. Hansen, I. Johannsen, Catalytic methanation of CO₂ in biogas: Experimental results from a reactor at full scale, *React. Chem. Eng.* 5 (2020) 183–189. doi:10.1039/c9re00351g.
- [5] M. Waidhas, Potential and challenges of PEM electrolyzers: kick-off meeting for the IEA technology roadmap on hydrogen, Paris; (2013).
- [6] J. Gorre, F. Ruoss, H. Karjunen, J. Schaffert, T. Tynjälä, Cost benefits of optimizing hydrogen storage and methanation capacities for Power-to-Gas plants in dynamic operation, *Appl. Energy.* 257 (2020). doi:10.1016/j.apenergy.2019.113967.
- [7] F. Ahmad, E.C. Lovell, H. Masood, P.J. Cullen, K.K. Ostrikov, J.A. Scott, R. Amal, Low-Temperature CO₂ Methanation: Synergistic Effects in Plasma-Ni Hybrid Catalytic System, *ACS Sustain. Chem. Eng.* 8 (2020) 1888–1898. doi:10.1021/acssuschemeng.9b06180.
- [8] H. Chen, Y. Mu, Y. Shao, S. Chansai, S. Xu, C.E. Stere, H. Xiang, R. Zhang, Y. Jiao, C. Hardacre, X. Fan, Coupling non-thermal plasma with Ni catalysts supported on BETA zeolite for catalytic CO₂ methanation, *Catal. Sci. Technol.* 9 (2019) 4135–4145. doi:10.1039/c9cy00590k.
- [9] B. Wang, M. Mikhail, S. Cavadias, M. Tatoulian, P. Da Costa, S. Ognier, Improvement of the activity of CO₂ methanation in a hybrid plasma-catalytic process in varying catalyst particle size or under pressure, *J. CO₂ Util.* 46 (2021). doi:10.1016/j.jcou.2021.101471.
- [10] J. Guilera, T. Andreu, N. Basset, T. Boeltken, F. Timm, I. Mallol, J.R. Morante, Synthetic natural gas production from biogas in a waste water treatment plant, *Renew. Energy.* 146 (2020) 1301–1308. doi:10.1016/j.renene.2019.07.044.

Chapter 7

Conclusions

Conclusions

The main objectives of the thesis were the development of a DBD plasma reactor for CO₂ conversion, including the study of different catalysts and the evaluation of different reactor configurations. In the first part of the thesis, Ni-based catalysts were synthesized and characterized. The catalytic performance was studied compared with thermal methanation. In addition, the energy efficiency of the process was analyzed. In the second part, different reactor configurations were studied with special focus on thermal management and the reduction of the energy cost.

The main conclusions of Part I, Catalyst for plasma CO₂ methanation, are:

- The DBD plasma reactor was validated with a Ni-based commercial catalyst, obtaining a CO₂ conversion of around 60 % with high selectivity to CH₄ (80%). The reaction was carried out at a considerably lower temperature compared with thermal methanation (100-170 °C vs. 350-400 °C) due to the plasma activation of the CO₂ molecules.
- Ni zeolite catalyst was studied in plasma and thermal methanation. For the different Si/Al ratios, the better textural and the lower affinity to water improve the catalytic activity. The incorporation of Ce boosted the conversion values at low applied power.
- The effect of Ce as a promotor was further investigated in chapter 4. Different optimum Ce composition was observed for plasma CO₂ methanation compared with thermal methanation. The dissociation of CO₂ to CO directly affected the activity of the catalyst in plasma methanation. The energy efficiency was enhanced from 29 to 40% for the optimum Ce composition.

The main conclusion of Part II, DBD reactor optimization, are:

- Experiments showed that reactor temperature depended on plasma power and reaction reactivity. It was demonstrated that reactor reached temperatures between 50 and 140 °C due to the plasma heating. Once the reactor was thermally insulated to work in adiabatic conditions, reactor temperature sharply increased from 200 to 350 °C. The higher temperature allowed to reduce the applied power and increase the energy efficiency by 20% (40 to 60%).
- Reactor temperature showed a direct relation with the gas flow rate, as the heat released by the reaction increased proportionally. Thus, reactor temperature can be controlled by modifying the gas flow either in pseudo-adiabatic and adiabatic conditions. The use of higher flow increased further the energy efficiency as the SEI was considerably reduced. In the best conditions, using an adiabatic reactor configuration and working with a high gas flow rate, an energy efficiency of 73% was obtained. Despite this, conversion and selectivity were slightly lower compared with adiabatic experiments at lower gas flow.

- Based on the results obtained in adiabatic conditions at high flow, a new reactor configuration was studied with two sequential catalytic beds and a new methodology was presented where the plasma was used to ignite the reaction. The higher temperature obtained in adiabatic configuration and high flow allowed to activate the catalyst by thermal catalysis.
- The thesis demonstrated that plasma could be used as an ignitor to start the reactor at low temperatures due to the plasma activation of CO₂ molecules. After plasma ignition and under specific conditions, the plasma can be shut down, and the reaction can be self-sustained in autothermal operation. In this configuration, the heat released by the methanation reaction can self-sustain the reaction. The ignition procedure was optimized, obtaining an extremely fast start-up time of only 3 minutes.

To summarise, Ni catalyst promoted with Ce presented the best results in plasma methanation, increasing the energy efficiency in the optimum catalyst composition. The use of an adiabatic reactor increased further the energy efficiency. A new methodology of using plasma as an ignitor was shown, minimizing the energy consumption and obtaining faster start-up times. The work performed in this thesis has opened new paths on how to make DBD CO₂ methanation a competitive technology compared with conventional thermal methanation, following the roadmap shown in **Figure 7.1**.

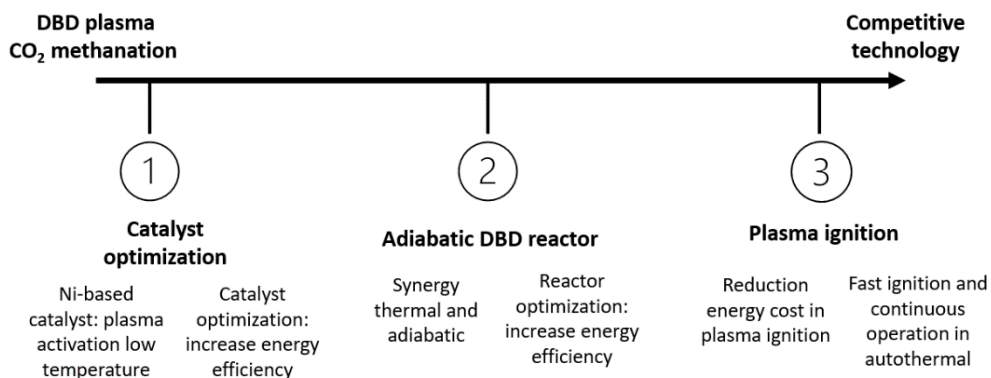


Figure 7.1. Thesis roadmap and main achievements.

Further work

Based on the work done in this thesis, there are further investigations to be done and challenges to overcome.

- Optimization and design of catalysts to work specifically in plasma catalysis. In this regard, in-situ techniques, such as DRIFTS with plasma, can reveal the direction in which should be the catalyst designed.
- Further research is necessary to obtain the required quality of the synthetic natural gas, in order to be injected into the natural gas grid. In this sense, there is work to do in plasma reactor scale-up to fit the typical industrial CO₂ sources. Considering the different possible CO₂ sources is important to study the effect of different gas compositions in plasma methanation, such as biogas or diluted streams.
- Finally, the use of plasma ignition can be interesting to be studied in other exothermic reactions that can be self-sustained. The integration of plasma in thermal reactors can be further developed.

Appendix

The appendix is divided into five parts:

- **Appendix A**, chapter 2. Equipment, characterization techniques and reactor geometry optimization.
- **Appendix B**, chapter 3. Supplementary catalyst characterization.
- **Appendix C**, chapter 4. Supplementary catalyst characterization and information of experimental setup for CO methanation experiments.
- **Appendix D**, chapter 5. Characterization of catalyst synthesized by wet impregnation, supplementary and theoretical power calculated for thermal methanation.
- **Appendix E**, chapter 6. Supplementary results of ignition experiments.



Appendix A

Appendix of chapter 2

A.1 Equipment and characterization techniques

Several techniques were used to characterize the catalyst (N_2 physisorption, CO_2 adsorption, H_2 -TPR, XRD, TEM, DRIFTS, ICP and TGA-DSC). The techniques and equipment are explained in this section.

- **N_2 physisorption and CO_2 adsorption**

The catalyst was analyzed with a Autosorb iQ equipment (chapter 3) and TriStar II 3020-Micromeritics (chapters 4 and 5). Textural properties of the catalysts were determined by N_2 -physisorption [1,2], while CO_2 affinity was measured by CO_2 adsorption [3,4]. N_2 physisorption measurements were carried out at $-196\text{ }^\circ\text{C}$. CO_2 adsorption measurements were done at 0°C . Prior to the measurements, the samples were degassed at $90\text{ }^\circ\text{C}$ for 1 h, and then at $250\text{ }^\circ\text{C}$ for 4 h. Brunauer-Emmett-Teller (BET) method was used to estimate surface area for a relative pressure (P/P_0) range between 0.05-0.30. Barrett-Joyner-Halenda (BJH) method was applied to the desorption branch of the isotherm to determine the pore size. The total pore volume was calculated from the adsorbed volume of nitrogen at a relative pressure of 0.95. The micropore volume was determined using the t-plot method. The mesopore volume was given by the difference between the total pore volume and the micropore volume.

- **Temperature programmed reduction**

The reducibility of the calcined catalysts was studied by temperature programmed reduction (H_2 -TPR) [5] with an Autochem Micromeritics equipment. H_2 -TPR was conducted using 12 vol.% H_2 /Ar at a flow of $50\text{ mL}\cdot\text{min}^{-1}$ in the temperature range of 35 to $800\text{ }^\circ\text{C}$ at a heating ramp of $10\text{ }^\circ\text{C}\cdot\text{min}^{-1}$. The amount of H_2 uptake was measured with a thermal conductivity detector.

- **X-ray diffraction**

Catalyst structural crystallinity was determined by XRD [6]. XRD (Bruker D8 Advance A25) was carried out by using a Cu $K\alpha$ radiation ($\lambda=1.5406\text{ nm}$), at 40 kV and 40 mA in a range from 20 to $60\text{--}80^\circ$. Crystalline phase was identified by using standard published by the International Centre for Diffraction Data (ICDD).

- **TEM**

Morphology and composition of catalysts were evaluated by TEM [7–9]. The catalysts of chapter 3 were analyzed with a HRTEM 2010 JEOL LaB6 microscope (200 kV) at Université Pierre et Marie Curie (Paris, France). The average Ni⁰ particle size was determined by using the ImageJ software (200 particles for each catalyst). In chapter 4, the catalysts were analyzed with Zeiss LIBRA 120 at IREC and FEI Tecnai F20 at ICN2. The FEI Tecnai F20 field emission gun microscope with a 0.19 nm point-to-point resolution at 200 kV was equipped with an embedded Quantum Gatan Image Filter for EELS analyses.

- **DRIFTS**

Diffuse reflectance infrared Fourier transform spectroscopy (DRIFTS) [2,10] experiments were done to analyze the species formed during the methanation reaction in thermal-catalysis operation. DRIFTS experiments were done in a BRUKER FTIR spectrometer (Vertex 70) using a praying mantis with a high-temperature reaction chamber. Before the CO₂ methanation DRIFTS experiments, the catalysts were in-situ reduced at 450 °C using a mix of 5% H₂ with Argon (2.5 mL·min⁻¹ of H₂ and 50 mL·min⁻¹ Ar). After the reduction, the system was cooled down to 200 °C, purged with Ar for 30 minutes and, finally, a background spectrum was measured. The gas feed was changed to the reaction gas diluted with Ar (8 mL·min⁻¹ of H₂, 2 mL·min⁻¹ of CO₂ and 10 mL·min⁻¹ of Ar). Spectrums were collected every 5 minutes for 30 minutes, and temperatures were increased 25 °C between 200 and 250 °C.

- **ICP**

Inductively coupled plasma optical emission spectrometry (ICP, Perkin Elmer Optima) was used to quantify the nickel and cerium content in the catalysts.

- **TGA-DSC**

Thermogravimetric analysis [11] were performed on a Setsys Evolution TGA from Setaram instruments. TGA-DSC was used to determine the hydrophobicity index (h index) and identify carbon deposition. For the h index, samples (0.035–0.040 g) were firstly saturated with water and then heated between 20 and 500 °C (10 °C·min⁻¹) under air flow (30 mL·min⁻¹). From the obtained results, h index was determined as the ratio between the registered mass loss at 150 and 400 °C. In the case of the experiments carried out for the identification of carbon deposits in the post-plasma samples, TGA-DSC analysis were carried out again under air flow (30 mL·min⁻¹), and samples were heated from 20 to 800 °C (10 °C·min⁻¹).

A.2 Reactor geometry optimization

DBD reactor geometry was optimized during the thesis. The inner quartz tube diameter was varied between 14 and 16 mm. Thus, the GAP was modified between 1 mm and 2 mm. The reactors performance were determined by comparing the methanation reaction. 30Ce-Ni was used as catalyst (developed in **chapter 4**). The reaction was performed in pseudo-adiabatic conditions and a constant gas flow of 200 mL·min⁻¹.

Figure A.1 shows the obtained conversions versus the power. The reactor with a GAP of 1.0 showed lower conversion, especially at low power. On the other hand, GAP distances of 1.5 and 2.0 mm presented very similar results, with a slightly higher conversion at low power for the higher GAP value. Therefore, the use of higher GAP showed better performance.

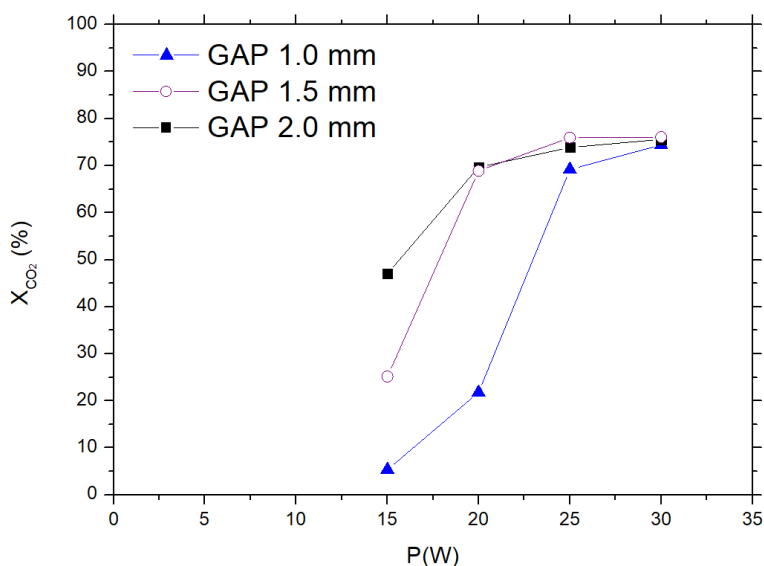


Figure A.1. Conversion vs power with the different reactor configurations: 1.0, 1.5 and 2.0 mm GAP distance.

It is important to note that these experiments were performed keeping the same electrode length (10 mm) and the same amount of catalyst. Therefore, as GAP increased, part of the plasma was generated without catalyst (**Figure A.2**).

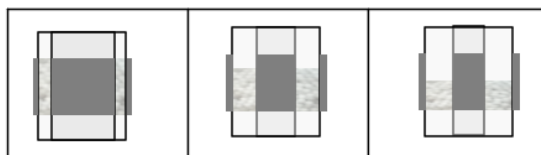


Figure A.2. Reactors schemes for the different GAP, keeping electrode length to 10 mm. The fraction of volume with catalyst (V_c) with respect to plasma volume (V_p) decreased for larger distance GAP: a) $V_c/V_p \sim 100\%$ b) $V_c/V_p \sim 70\%$ c) $V_c/V_p \sim 50\%$.

Additional experiments were done to determine whether the improvement was due to the change in the ratio between catalyst and plasma (V_d/V_p). Experiments were done with different electrode lengths and GAP distances. The electrode length was reduced in the reactor with a GAP of 2 mm to maintain the same V_d/V_p ratio as the reactor with 1 mm of GAP (**Figure A.3**).

Figure A.4 shows the results comparing 5 and 10 mm of length. The conversion decreased when the length was reduced (V_d/V_p was increased). However, if we compare with the same V_d/V_p configuration and lower GPA (1 mm), the conversions were higher than the reactor with the lowest GAP. Thus, even some effects could be related to the catalyst/plasma ratio, the change of GAP (and the effect of the discharge) cause the significant improvement.

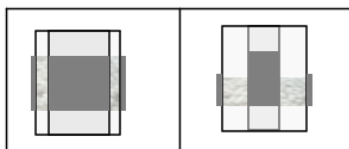


Figure A.3. Similar conditions for GAP 1 and 2 mm with an electrode of 10 mm and 5 mm.

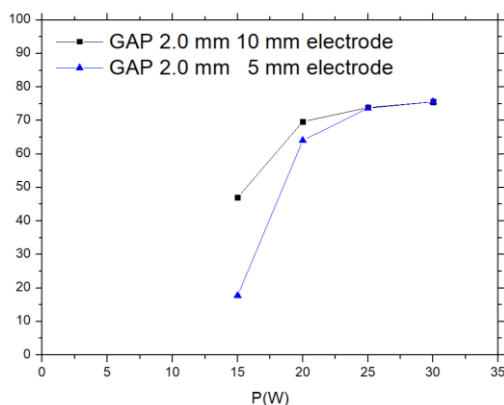


Figure A.4. Conversion vs power with the different reactor configurations: GAP 2.0 mm and electrode of 10 and 5 mm of length.

In summary, the best reactor configuration was obtained with the higher GAP of 2.0 mm and keeping the electrode length to 10 mm. The obtained configuration was used in the adiabatic/pseudo-adiabatic configuration studies (**chapter 5** and **6**).

A.3 LabView program: power measurement

A LabView program was developed to monitor in-situ electrical signals and calculated the power by the Lissajous method. **Figure A.5** shows the front panel of the LabView program.

The LabView program was based on a modification of the example from Picoscope, “*PicoScope5000AExamplesStreamingMSO*” (picosdk-ni-labview-examples). The original program was modified to acquire the three channels (voltage, current and

voltage across the Lissajous capacitor). The stream data were processed as shown in **Figure A.6** and **Figure A.7**, where the data was passed through a SubVI to preselect only a period for the Lissajous measurement. The power measurement was implemented in an additional SubVI (**Figure A.8**) with the Lissajous method. Finally the power was averaged over 100 cycles.

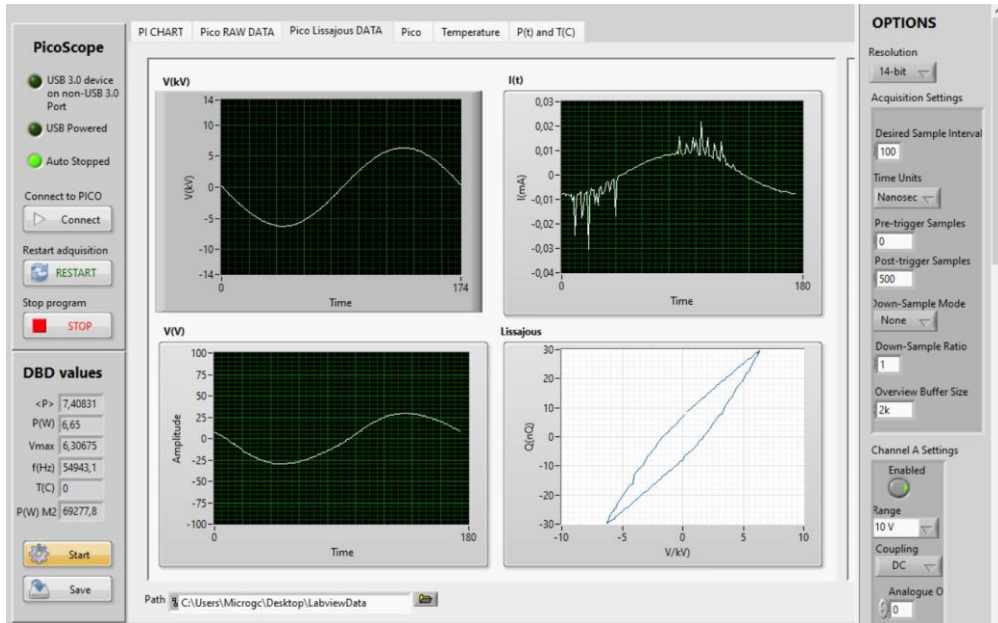


Figure A.5. LabView front panel.

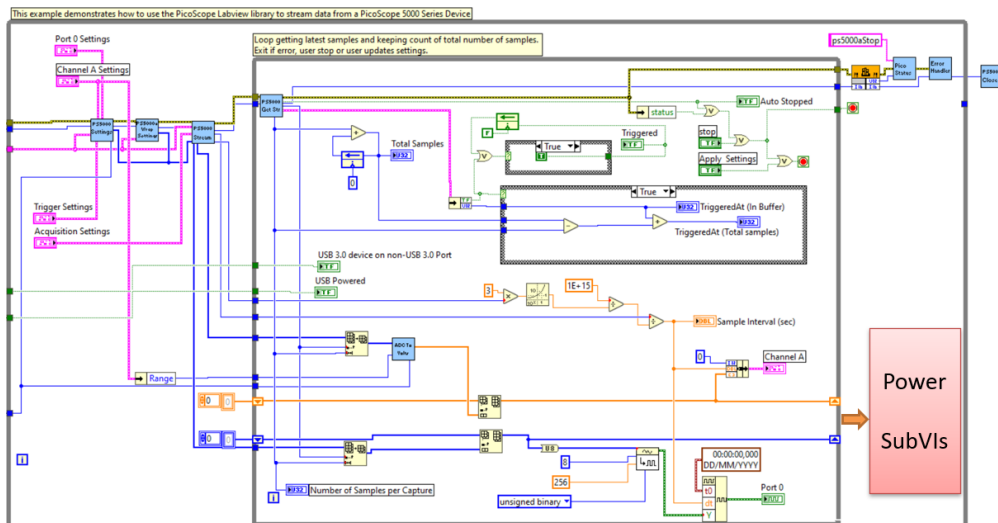


Figure A.6. PicoScope5000AExemplesStreamingMSO.

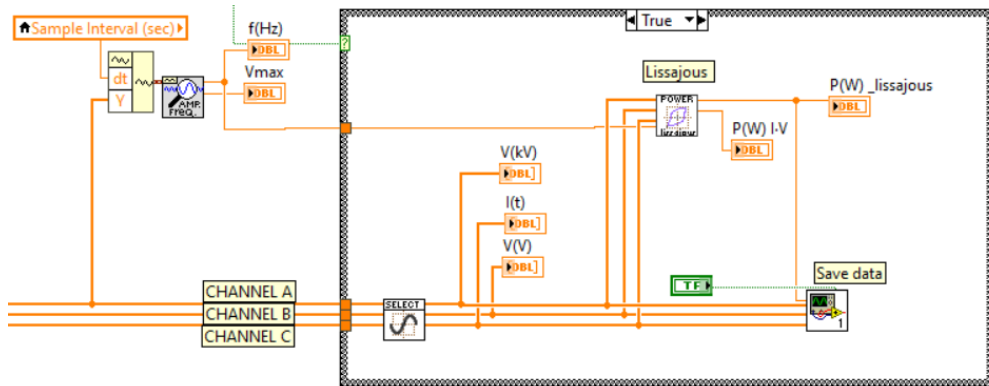


Figure A.7. Block diagram of the modified PicoScope5000AExemplesStreamingMSO for power calculation.

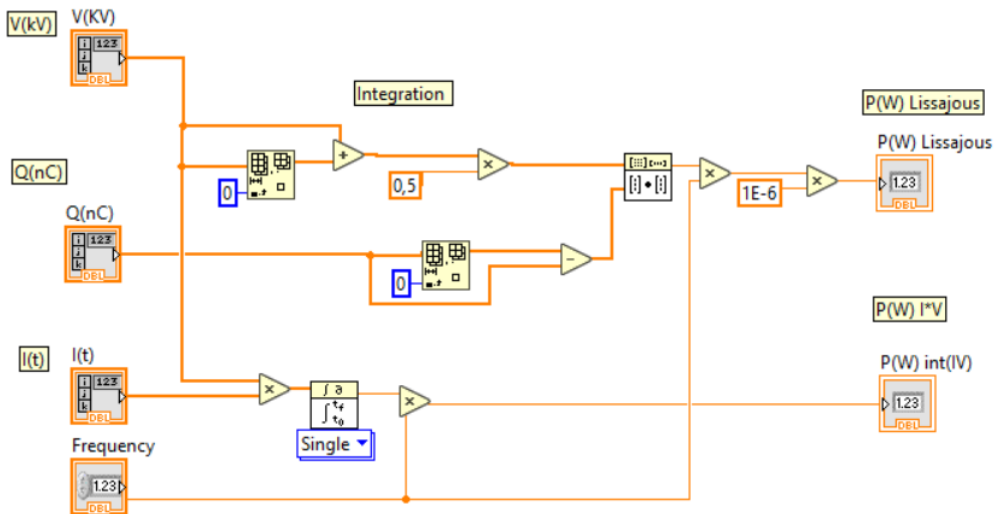


Figure A.8. LabView block diagram of power calculation SubVI.

Appendix B

Appendix of chapter 3

B.1 Supplementary catalyst characterization

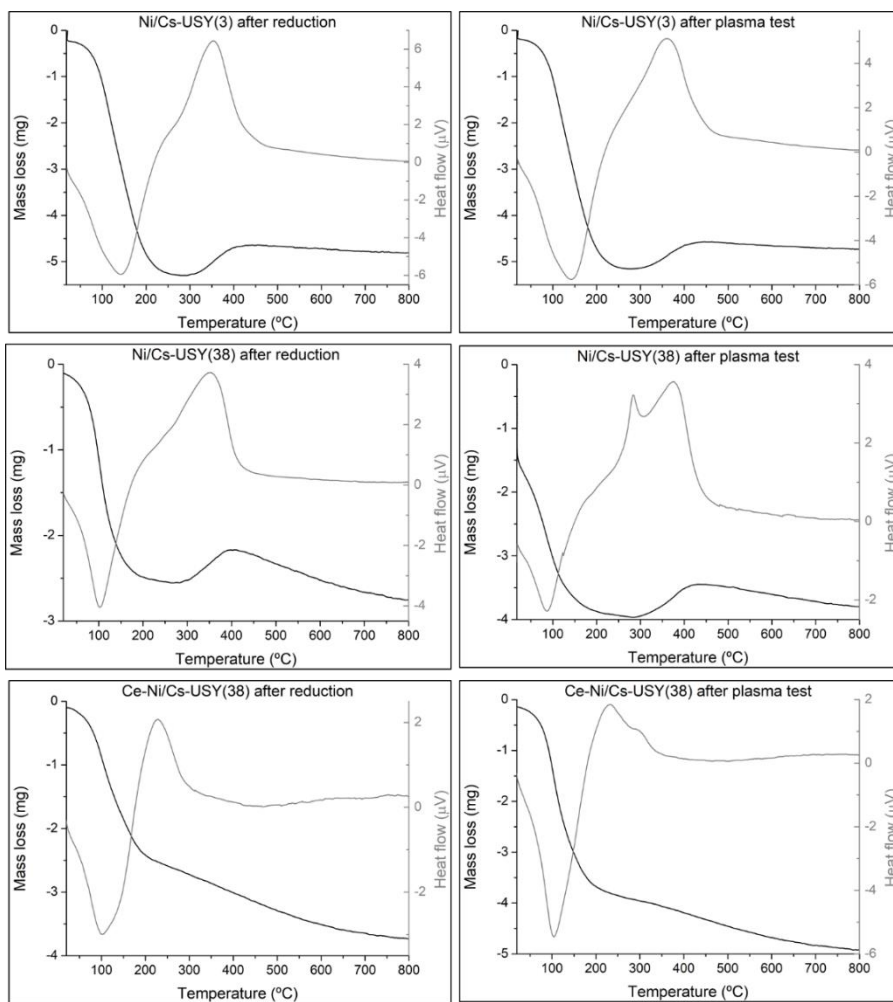


Figure B.1. TGA-DSC analysis results obtained for the Ni/Cs-USY(3), Ni/Cs-USY(38) and Ce-Ni/Cs-USY(38) catalysts after pre-reduction treatment and after plasma tests.

Appendix C

Appendix of chapter 4

C.1 Supplementary catalyst characterization

Supplementary information: N₂-physisoption isotherms, H₂-TPR profile, HRTEM, DRIFT and catalytic additional results. Initial TEM images were done at IREC (**Figure C.3**), while the detailed HRTEM analysis (**Figure C.4 to C.7**) was performed by Ting Zhang and analyzed together with Jordi Arbiol at the Catalan Institute of Nanoscience and Nanotechnology (ICN2).

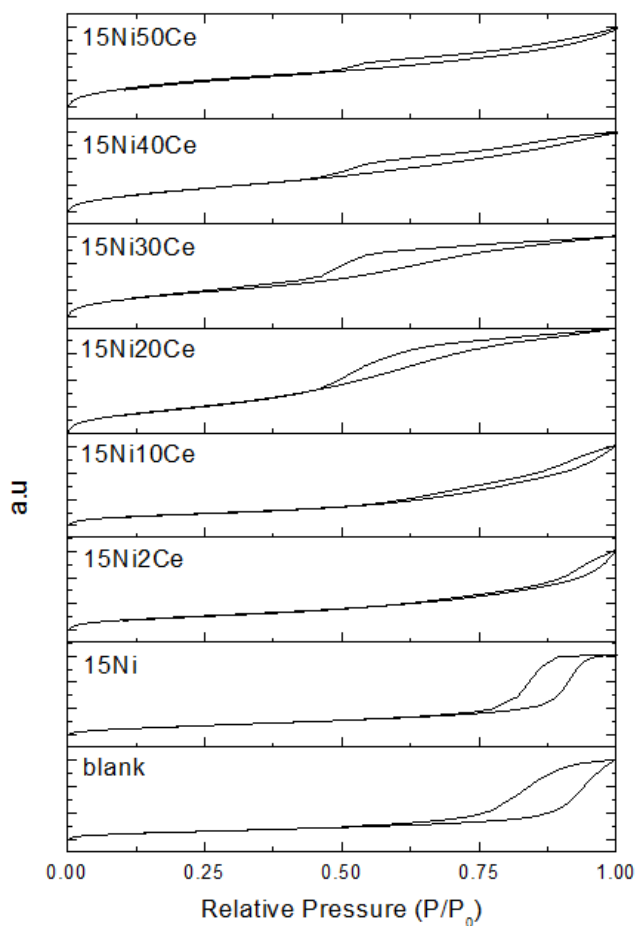


Figure C.1. N₂-physisoption isotherms.

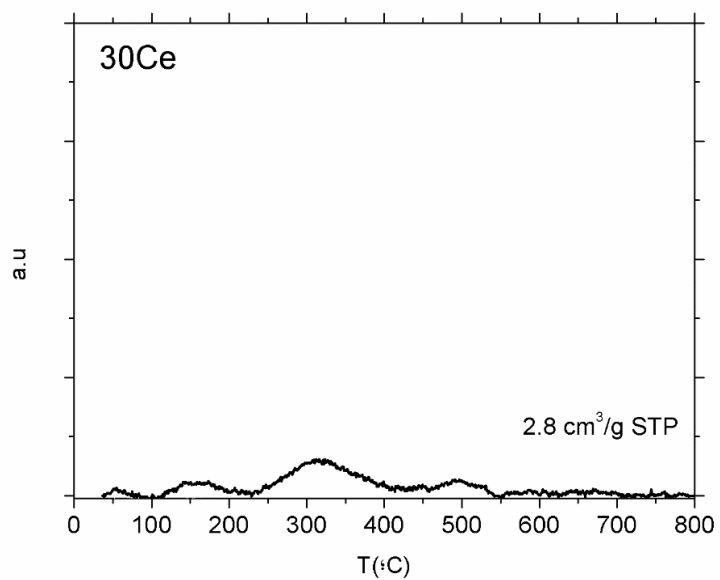


Figure C.2. H₂-TPR profile of the 30% Ce (Ce/Al₂O₃).

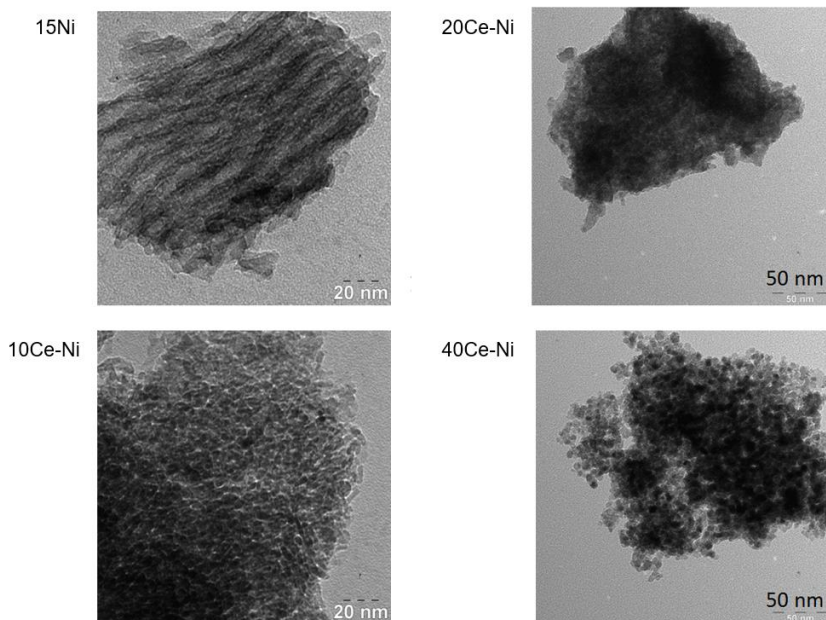


Figure C.3. TEM micrographs for 15Ni, 10Ce-Ni, 20Ce-Ni and 40Ce-Ni.

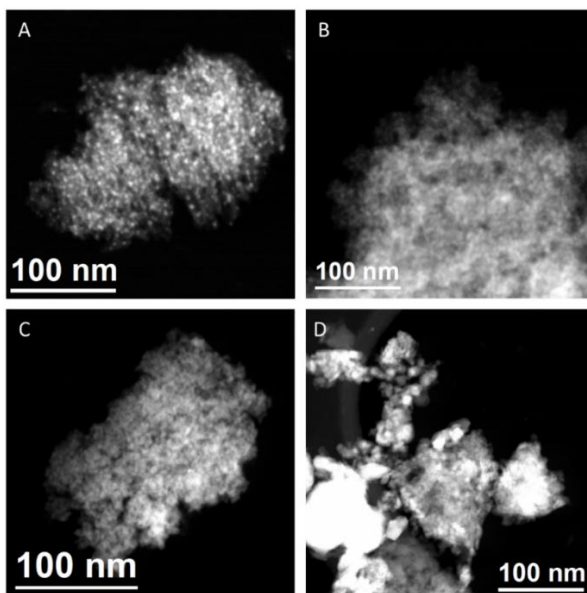


Figure C.4. General HAADF STEM micrographs obtained on the a) 15Ni, b) 10Ce-Ni, c) 30Ce-Ni and d) 50Ce-Ni.

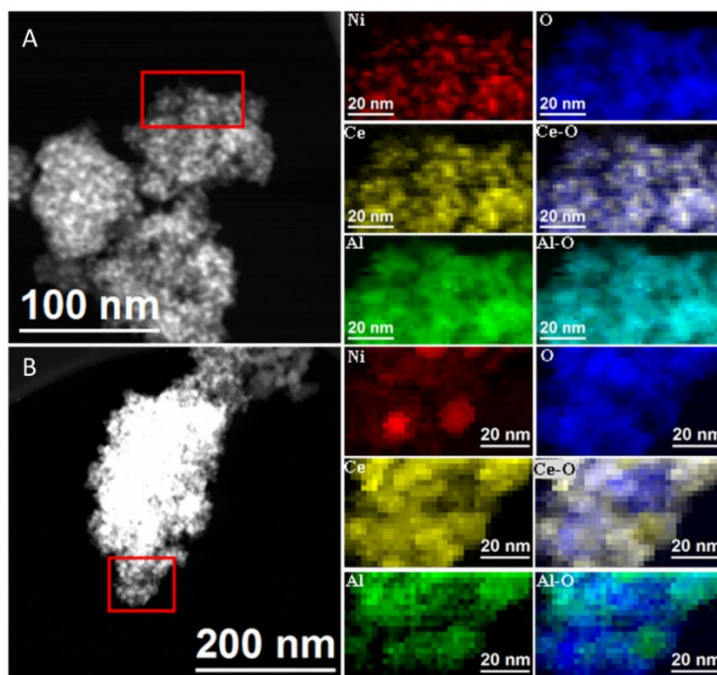


Figure C.5. STEM micrograph of a) 10Ce-Ni catalyst and b) 30Ce-Ni catalyst. EELS chemical composition maps obtained from the red squared area on the STEM micrograph on the left. Individual Ni L_{2,3}-edges at 855 eV (red), Ce M_{4,5}-edges at 833 eV (yellow), Al K-edges at 1560 eV (green) and O K-edge at 532 eV (blue) composition maps as well as their composites (Ce-O and Al-O).

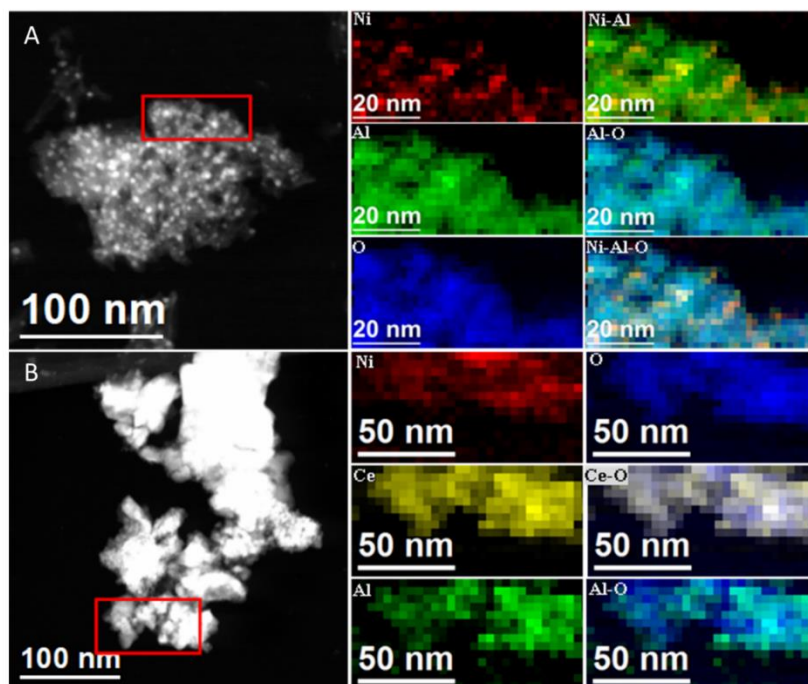


Figure C.6. STEM micrograph of **a)** 15Ni catalyst and **b)** 50Ce-Ni catalyst. EELS chemical composition maps obtained from the red squared area on the STEM micrograph on the left. Individual Ni L_{2,3}-edges at 855 eV (red), Ce M_{4,5}-edges at 833 eV (yellow), Al K-edges at 1560 eV (green) and O K-edge at 532 eV (blue) composition maps as well as their composites (Ce-O and Al-O).

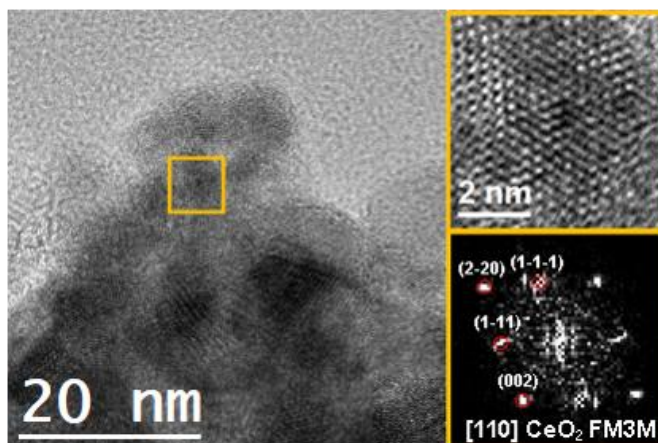


Figure C.7. HRTEM micrograph of 50Ce-Ni. On the right, the detail of the orange squared region and its corresponding power spectrum (bottom). The crystal phase is in agreement with the CeO₂ cubic phase (space group = FM3M) with $a=b=c=5.4100$ Å. From the crystalline domain, the CeO₂ lattice fringe distances were measured to be 0.272, 0.329 nm, 0.206 nm and 0.316 nm, at 57.24°, 95.01° and 133.92° which could be interpreted as the cubic CeO₂ phase, visualized along its [110] zone axis.

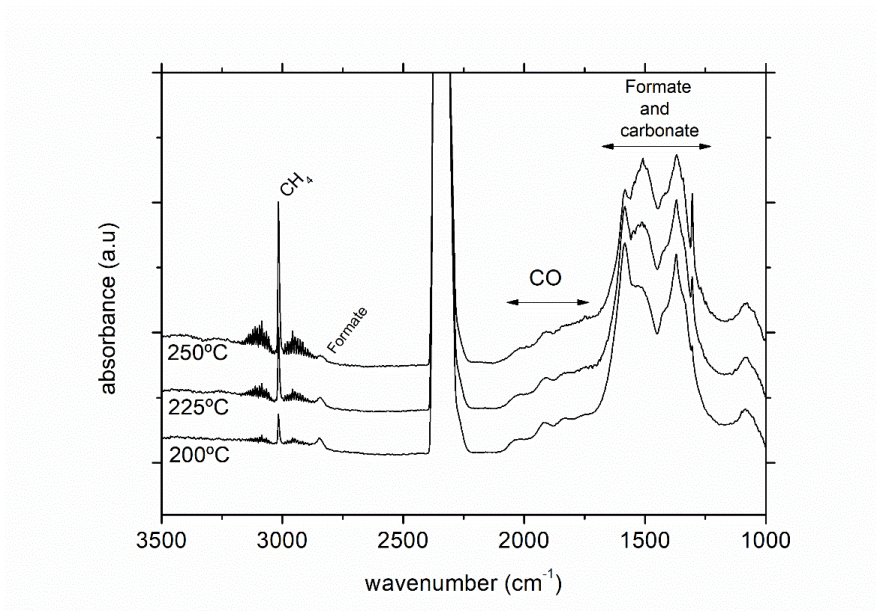


Figure C.8. DRIFTS spectra of 30Ce-Ni.

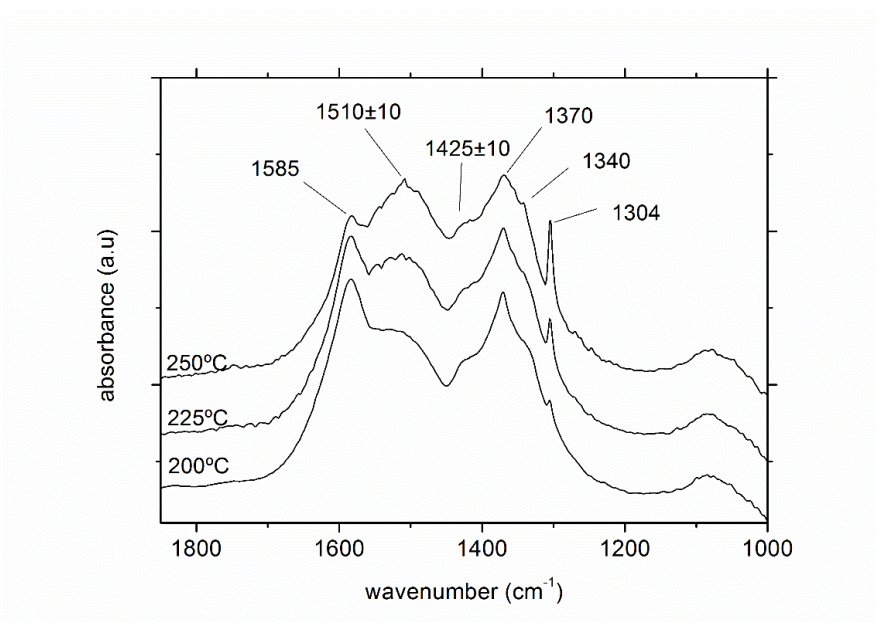
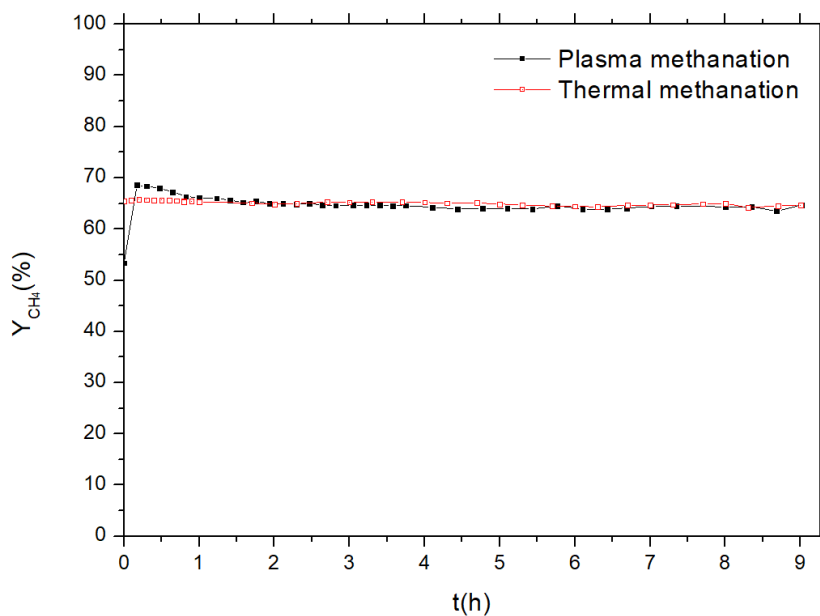


Figure C.9. DRIFTS spectra of 30Ce-Ni between 1820 and 1000 cm⁻¹.

Table C.2. Table of the different bands observed in DRIFTS experiments.

Species	Bands (cm ⁻¹)		
CO ₂	2345		
CH ₄	3020		
Linear CO	2040	1920	
Formate	2850	1585	1370
Carbonate	1425	1340	-
Carboxylates	1304	-	-

**Figure C.10.** Plasma stability experiment during 8h with 20Ce-Ni catalyst. For comparison, thermal stability was performed, adjusting the initial temperature to have a similar conversion than plasma stability experiment.

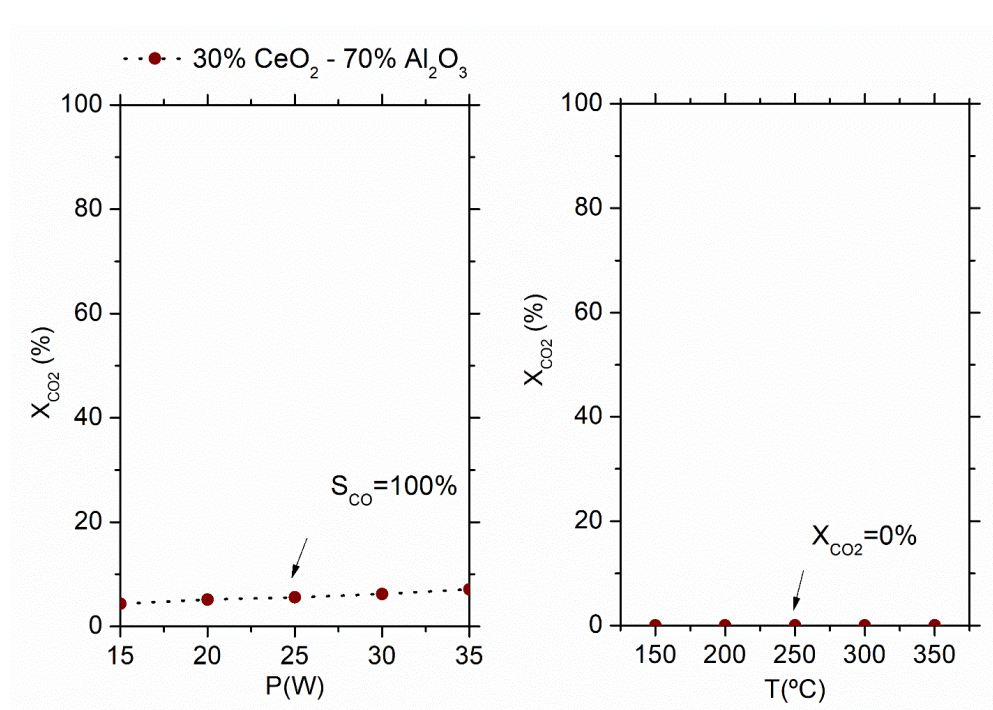


Figure C.11. Catalytic results of 30% Ce (Ce/Al₂O₃). **(Left)** Plasma **(Right)** Thermal.

C.2 Experimental setup for the CO methanation experiments

CO methanation experiments were done in a fixed-bed micro reactor (Microactivity Reference, PID Eng&Tech) prepared to work with CO gas (**Figure C.11**). For the experiments, 0.3g of catalyst was loaded in the reactor. The catalyst was reduced ex-situ using the same conditions for the CO₂ methanation (see **chapter 2**). A total flow of 100 mL·min⁻¹ of CO/H₂ (ratio 2) was used. The output gases were analyzed with a micro gas chromatograph equipped with MoSieve and PoraPLOT columns.

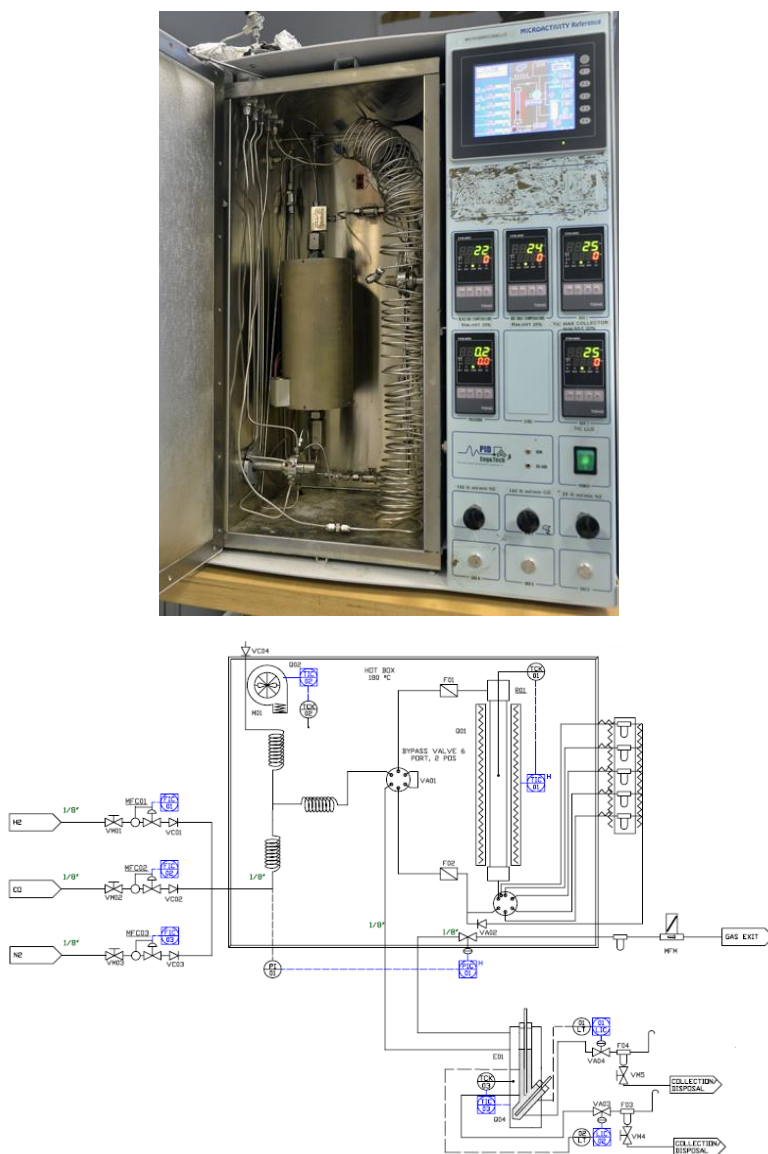


Figure C.12. Microactivity reactor used for the thermal CO methanation experiments.

Appendix D

Appendix of chapter 5

D.1 Characterization of catalyst prepared by wet impregnation on commercial alumina

The 30Ce-Ni-WET catalyst prepared by wet impregnation was characterized with BET, H₂-TPR and CO₂ methanation experiments. The catalyst was compared with the equivalent EISA catalyst (30Ce-Ni EISA).

Figure D.1 shows the H₂-TPR results. For 30Ce-Ni WET sample, NiO species was reduced at a lower temperature (200-350 °C) which corresponds to species with weak interaction with the support. On the other hand, 30Ce-Ni EISA samples presented mainly NiO species with stronger interaction with the support (350-600°C). **Table D.1** summarize the results of H₂-TPR and N₂-physisorption. The catalyst prepared by wet impregnation showed better textural properties (higher surface area) and better reducibility. Finally, (**Figure D.2**) XRD shows that 30Ce-Ni-WET have higher crystallinity than 30Ce-Ni-EISA.

Comparing the activity, **Figure D.3**, 30Ce-Ni-WET presented higher conversion values compared with 30Ce-Ni-EISA. The higher activity can be directly related to the better textural and reducibility of the 30Ce-Ni-WET.

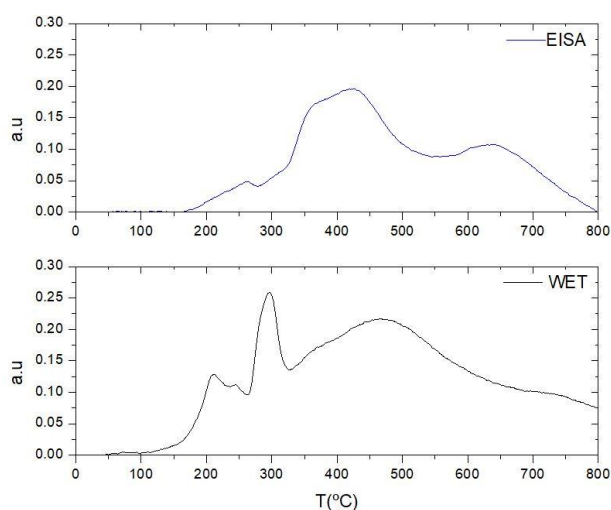
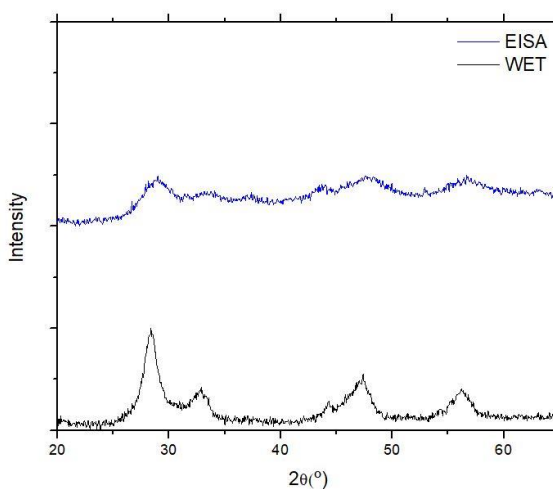
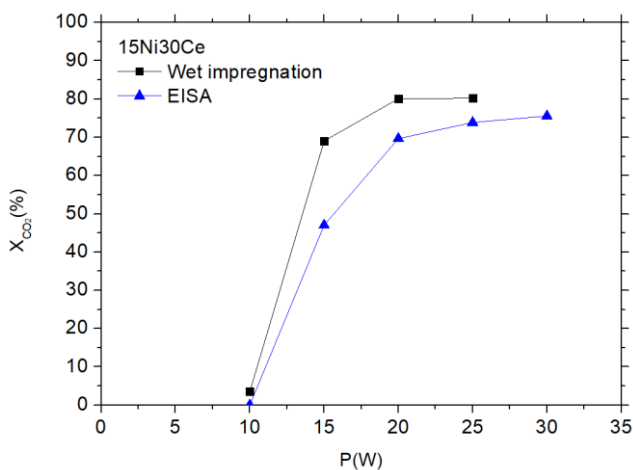


Figure D.1. H₂-TPR results of 30Ce-Ni prepared by EISA and 30Ce-Ni by WET impregnation method.

Table D.1. Summary of the main physicochemical characterization.

Sample	BET		H ₂ -TPR
	Surface area (m ² .g ⁻¹)	Pore size (nm)	T _{red} (°C)
30Ce-Ni- EISA	42	4.3	426
30Ce-Ni- WET	149	8.4	300

**Figure D.2.** XRD results of 30Ce-Ni prepared by EISA and 30Ce-Ni by WET impregnation method.**Figure D.3.** Comparison of 30Ce-Ni prepared by EISA and 30Ce-Ni by WET impregnation method (200 mL·min⁻¹ CO₂/H₂ in pseudo-adiabatic reactor configuration).

D.2 Additional results: Adiabatic and pseudo-adiabatic configuration

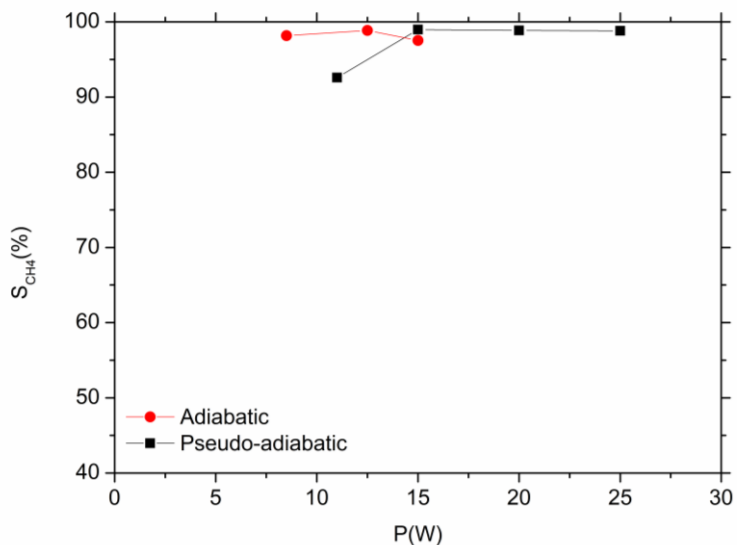


Figure D.4. Selectivity vs power for adiabatic and pseudo-adiabatic ($40,000 \text{ mL}\cdot\text{g}^{-1}\cdot\text{h}^{-1}$).

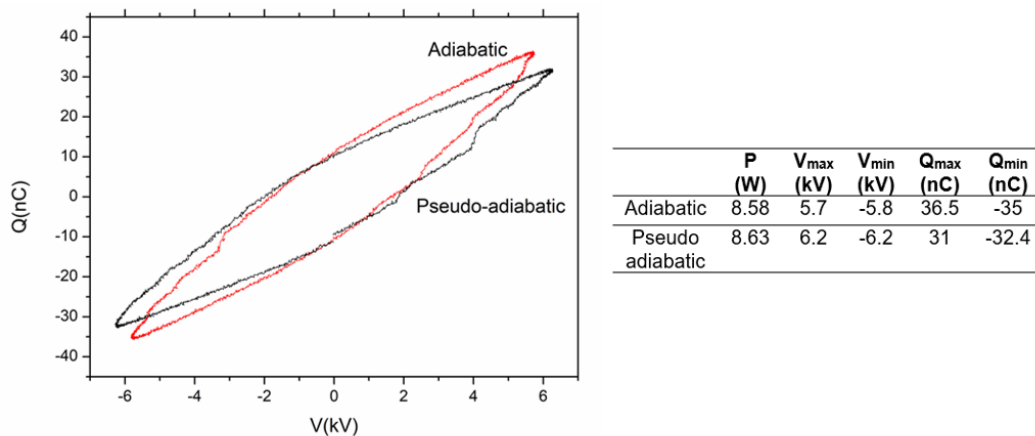


Figure D.5. Lissajous figures for adiabatic and pseudo-adiabatic.

D. 3 Theoretical power calculated for thermal methanation

The theoretical power needed in the case thermal methanation was calculated considering that the power that is needed to heat the gases, considering the same conditions used for plasma methanation (GHSV).

The power needed to heat 200 mL·min⁻¹ of CO/H₂ from 25°C to 350°C was calculated using the next equation:

$$P(W) = \eta \cdot F(\text{mols} \cdot \text{s}^{-1}) \cdot Cp (J \cdot \text{mols}^{-1} \cdot K^{-1}) \cdot \Delta T(K)$$

where F is the number of mols of CO/H₂, ΔT is the increment of temperature (ΔT= 325 K), η is the heater efficiency and the Cp is the heat capacity of the gas:

$$Cp_{CO_2/H_2} = 0.8 \cdot Cp_{H_2} + 0.2 \cdot Cp_{CO_2}$$

As the Cp is dependent of the temperature, the heat capacity used in the equation 1 is an average between the Cp_{CO_2/H_2} at 25°C and Cp_{CO_2/H_2} at 350 °C. The heater efficiency value (η) was obtained from the data of a real methanation reactor from a pilot plant [12]. All the constants and values used can be found in the next table.

Flow CO ₂ /H ₂ (mL·min ⁻¹)	Cp @ 25°C		Cp @ 350°C		Cp (J·mol ⁻¹ ·K ⁻¹)	F (mol·s ⁻¹)	η (%)	P (W)
	H ₂	CO ₂	H ₂	CO ₂				
200	28.84	37.12	29.35	47.87	31.77	0.00003	34.2	4.1
700	28.84	37.12	29.35	47.87	31.77	0.00005	34.2	14.4

Appendix E

Appendix of chapter 6

E. 1 Experiments done at different GHSV

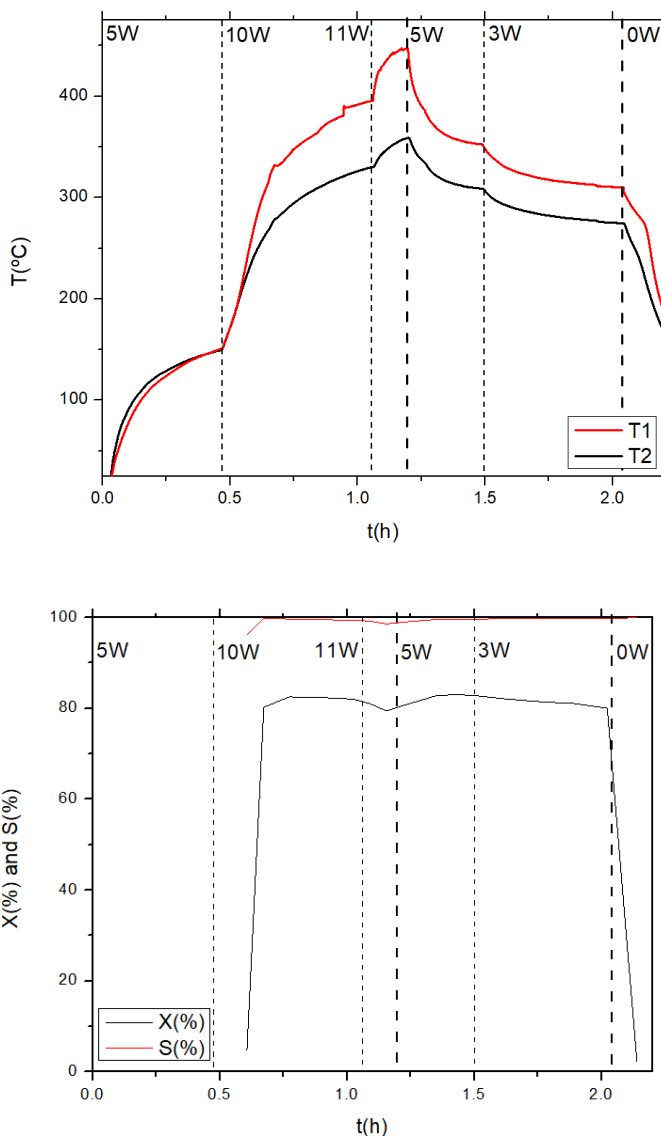


Figure E.1. Experiment done at $26,666 \text{ mL}\cdot\text{g}^{-1}\cdot\text{h}^{-1}$.

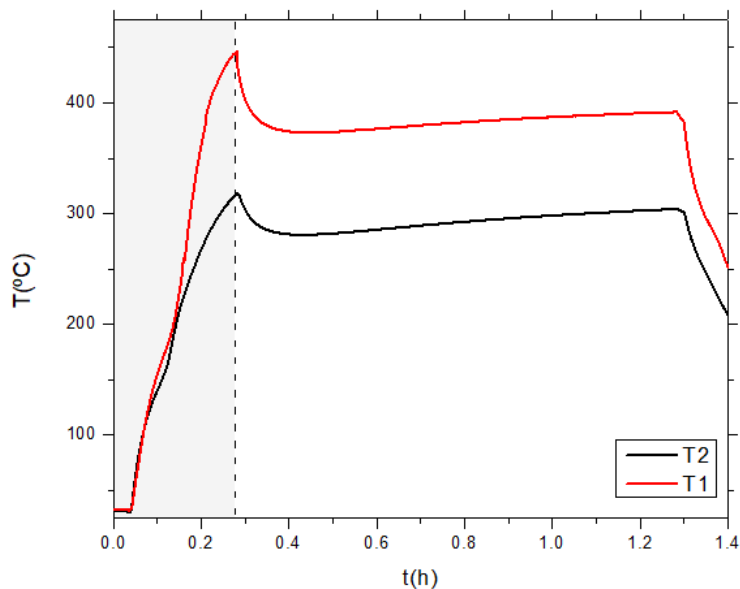


Figure E.2. Experiment done at $60,000 \text{ mL}\cdot\text{g}^{-1}\cdot\text{h}^{-1}$ activated with 10 W (grey area).

E. 2 Two steps activation experiments

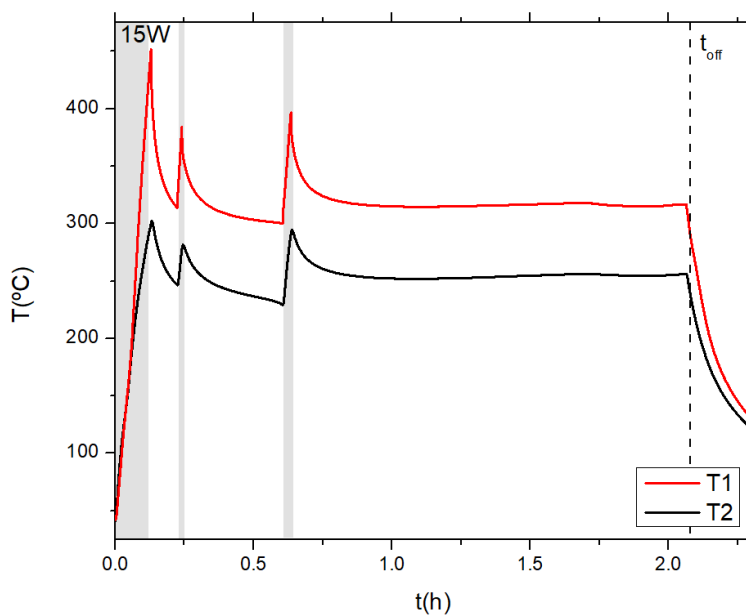


Figure E.3. Experiment done at $40,000 \text{ mL}\cdot\text{g}^{-1}\cdot\text{h}^{-1}$ activated with 15 W . Plasma was activated in the grey areas while plasma was shut-off in white areas.

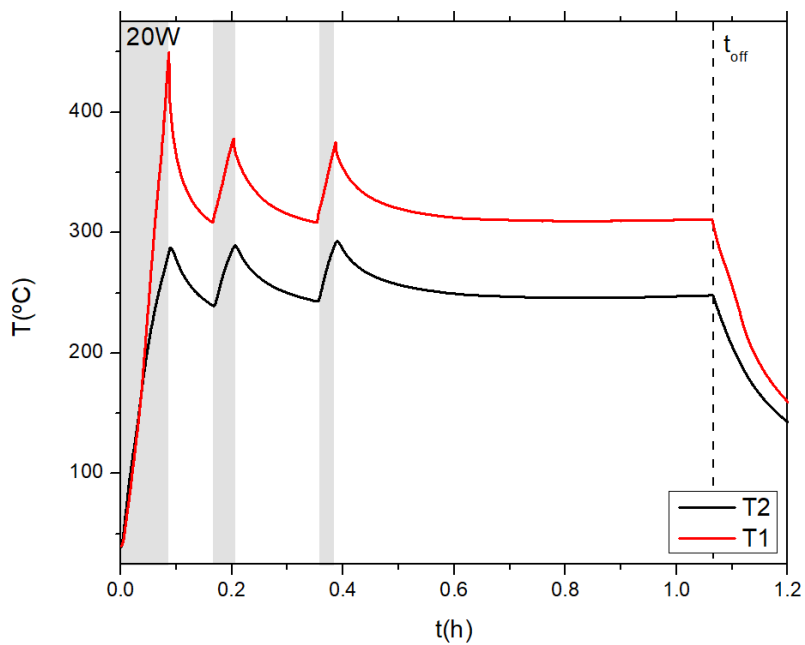


Figure E.4. Experiment done at $40,000 \text{ mL}\cdot\text{g}^{-1}\cdot\text{h}^{-1}$ activated with plasma 20 W.

Appendix references

- [1] M. Thommes, K. Kaneko, A. V. Neimark, J.P. Olivier, F. Rodriguez-Reinoso, J. Rouquerol, K.S.W. Sing, Physisorption of gases, with special reference to the evaluation of surface area and pore size distribution (IUPAC Technical Report), *Pure Appl. Chem.* 87 (2015) 1051–1069. doi:10.1515/pac-2014-1117.
- [2] R. Bardestani, G.S. Patience, S. Kaliaguine, Experimental methods in chemical engineering: specific surface area and pore size distribution measurements—BET, BJH, and DFT, *Can. J. Chem. Eng.* 97 (2019) 2781–2791. doi:10.1002/cjce.23632.
- [3] Y. Wang, M.D. LeVan, Adsorption Equilibrium of Carbon Dioxide and Water Vapor on Zeolites 5A and 13X and Silica Gel: Pure Components, *J. Chem. Eng. Data.* 54 (2009) 2839–2844. doi:10.1021/je800900a.
- [4] Y. Park, D.-K. Moon, Y.-H. Kim, H. Ahn, C.-H. Lee, Adsorption isotherms of CO₂, CO, N₂, CH₄, Ar and H₂ on activated carbon and zeolite LiX up to 1.0 MPa, *Adsorption.* 20 (2014) 631–647. doi:10.1007/s10450-014-9608-x.
- [5] C. Pirola, F. Galli, G.S. Patience, Experimental methods in chemical engineering: Temperature programmed reduction—TPR, *Can. J. Chem. Eng.* 96 (2018) 2317–2320. doi:10.1002/cjce.23317.
- [6] R.A. Dunlap, X-ray diffraction techniques, in: *Nov. Microstruct. Solids*, Morgan & Claypool Publishers, 2018: pp. 2–16. doi:10.1088/2053-2571/aae653ch2.
- [7] H. Reimer, Ludwig, Kohl, *Transmission Electron Microscopy*, Springer New York, New York, NY, 2008. doi:10.1007/978-0-387-40093-8.
- [8] D.B. Williams, C.B. Carter, *Transmission Electron Microscopy*, Springer US, Boston, MA, 2009. doi:10.1007/978-0-387-76501-3.
- [9] N. Braidy, A. Béchu, J.C. de Souza Terra, G.S. Patience, Experimental methods in chemical engineering: Transmission electron microscopy—TEM, *Can. J. Chem. Eng.* 98 (2020) 628–641. doi:10.1002/cjce.23692.
- [10] M.B. Mitchell, Fundamentals and Applications of Diffuse Reflectance Infrared Fourier Transform (DRIFT) Spectroscopy, in: *Struct. Relations Polym.*, n.d.: pp. 351–375. doi:10.1021/ba-1993-0236.ch013.
- [11] N. Saadatkah, A. Carillo Garcia, S. Ackermann, P. Leclerc, M. Latifi, S. Samih, G.S. Patience, J. Chaouki, Experimental methods in chemical engineering: Thermogravimetric analysis—TGA, *Can. J. Chem. Eng.* 98 (2020) 34–43. doi:10.1002/cjce.23673.
- [12] J. Guilera, T. Andreu, N. Basset, T. Boeltken, F. Timm, I. Mallol, J.R. Morante, Synthetic natural gas production from biogas in a waste water treatment plant, *Renew. Energy.* 146 (2020) 1301–1308. doi:10.1016/j.renene.2019.07.044.

-CV-

PERSONAL INFORMATION

Name: Martí Biset Peiró
Birthday: 16/01/1991
Nationality: Spanish
Email: marti.biset@gmail.com
mbiset@irec.cat
ResearcherID: A-4429-2019
Scopus Author ID: 57193497187
ORCID: 0000-0002-1255-7733

EDUCATION

- 2017 - Present **Nanoscience Ph.D.**
Thesis: DBD plasma reactor for CO₂ methanation
University of Barcelona (UB)
Barcelona-Spain
- 2014 - 2015 **Nanoscience and Nanotechnology M.Sc.**
University of Barcelona (UB)
Thesis: NiFe thin films as oxygen evolution catalyst
Barcelona-Spain
- 2009 - 2014 **Physics B.Sc.**
University of Barcelona (UB)
Barcelona-Spain

PROFESSIONAL EXPERIENCE

- 2017 - Present **Laboratory Technician**
Catalonia Institute for Energy Research (IREC)
Barcelona-Spain
- 2015 - 2017 **Laboratory Technician Assistant**
Catalonia Institute for Energy Research (IREC)
Barcelona-Spain

PUBLICATIONS

9 research articles, 3 as first author.

- Jordi Guilera, José Antoni Díaz-López, Antonio Berenguer, **Martí Biset-Peiró**, Teresa Andreu
Fischer-Tropsch synthesis: towards a highly-selective catalyst by lanthanide promotion under relevant CO₂ syngas mixtures
Applied Catalysis A: General **2021**, 118423
- Ting Zhang, Xu Han, Hong Liu, **Martí Biset-Peiró**, Xuan Zhang, Pingping Tan, Pengyi Tang, Bo Yang, Lirong Zheng, Joan Ramon Morante, Jordi Arbiol.
Quasi-Double-Star Nickel and Iron Active Sites for High-Efficient Carbon Dioxide Electroreduction. Energy & Environmental Science. **2021**, 14, 4847-4857
- José Antonio Díaz-López, Jordi Guilera, **Martí Biset-Peiró**, Dan Enache, Gordon Kelly, Teresa Andreu.
Passivation of Co/Al₂O₃ Catalyst by Atomic Layer Deposition to Reduce Deactivation in the Fischer–Tropsch Synthesis. Catalysts. **2021**, 11, 732.
- **Martí Biset-Peiró**, Rubén Mey, Jordi Guilera, Teresa Andreu.
Adiabatic plasma-catalytic reactor configuration: Energy efficiency enhancement by plasma and thermal synergies on CO₂ methanation. Chemical Engineering Journal. **2020**, 393, 124786
- Peng-Yi Tang, Li-Juan Han, Franziska Simone Hegner, Paul Paciok, **Martí Biset-Peiró**, Hong-Chu Du, Xian-Kui Wei, Lei Jin, Hai-Bing Xie, Qin Shi, Teresa Andreu, Mónica Lira-Cantú, Marc Heggen, Rafal E. Dunin-Borkowski, Núria López, José Ramón Galán-Mascarós, Joan Ramon Morante, Jordi Arbiol.
Boosting Photoelectrochemical Water Oxidation of Hematite in Acidic Electrolytes by Surface State Modification. Advanced Energy Materials. **2019**, 9, 1901836.
- **Martí Biset-Peiró**, Jordi Guilera, Ting Zhang, Jordi Arbiol, Teresa Andreu.
On the role of ceria in Ni-Al₂O₃ catalyst for CO₂ plasma methanation. Applied Catalysis A: General. **2019**, 575, 223 – 229
- Maria del Carmen Bacariza¹, **Martí Biset-Peiró**¹, Ines Graça, Jordi Guilera, Joan Ramon Morante, José M. Lopes, Teresa Andreu, Carlos Henriques.
DBD plasma-assisted CO₂ methanation using zeolite-based catalysts: Structure composition-reactivity approach and effect of Ce as promoter. Journal of CO₂ Utilization. **2018**, 26, 202-211

- PengYi Tang, HaiBing Xie, Carles Ros, LiJuan Han, **Martí Biset-Peiró**, YongMin He, Wesley Kramer, Alejandro Pérez Rodríguez, Edgardo Saucedo, José Ramón Galán-Mascarós, Teresa Andreu, Joan Ramon Morantea, Jordi Arbiol. Enhanced Photoelectrochemical Water Splitting of Hematite Multilayer Nanowires Photoanode with Tuning Surface State via Bottom-up Interfacial Engineering. *Energy Environ. Sci.*, **2017**, 00, 113
- **Martí Biset-Peiró**, Sebastián Murcia-López, Cristian Fàbrega, Joan Ramon Morante, T. Andreu. Multilayer Ni/Fe thin films as oxygen evolution catalysts for solar fuel production. *Journal of Physics D: Applied Physics*. **2017**, 50, 104003

CONFERENCES

8 participations in conferences, 2 as oral speaker.

- T. Andreu, J. Guilera, A. Alarcon, **M. Biset-Peiró**. Structured catalysts for synthetic natural gas production through CO₂ methanation. 2019. Presented at IV International Congress of Nanoscience and Nanotechnology, Quito, Ecuador.
- **M. Biset-Peiró**, R. Mey, J. Guilera, T. Andreu. Methanation through plasma-catalysis: synergy between plasma and thermal activation. 2019. Presented at 3rd Adding value to CO₂, Móstoles, Spain.
- **M. Biset-Peiró**, R. Mey, J. Guilera, T. Andreu. CO₂ methanation by plasma-catalysis: increase in energy efficiency through temperature control. 2019. Presented at Secat'19, Cordova, Spain.
- **M. Biset-Peiró**; J. Guilera; J.R. Morante; T. Andreu. Plasma catalysis for CO₂ methanation: catalyst and reactor optimization. JIPI (Jornada d'Investigadors Predoctorals Interdisciplinària). M. Biset-Peiró; J. Guilera; J.R. Morante; T. Andreu.
- E. Pervolarakis, **M. Biset-Peiró**, M. Charalampakis, G. Kiriakidis, J. R. Morante, T. Andreu, V. Binas. Co-Ni bimetallic catalysts supported on CeO₂ for CO₂ plasma and thermal methanation. Presented at TCM 2018 - 7th International Symposium Transparent Conductive Materials, Crete, Greece.
- **M. Biset-Peiró**, J. Guilera, J.R. Morante, T. Andreu. 2017. CO₂ valorization through plasma-catalysis. Presented Forum for next generation researchers – VI World Material, Strasbourg, France.
- **M. Biset-Peiró**, J. Guilera, A. Ceballos, J.R. Morante, T. Andreu. 2017. Mesoporous Ni-CeO₂-Al₂O₃ catalyst for plasma-catalysis CO₂ methanation. Presented at 21st Solid State Ionics, Padua, Italy.

- **M. Biset-Peiró** , J. Guilera, A. Ceballos, J. R. Morante, T. Andreu. 2017. New routes for CO₂ methanation: plasma-catalysis. Presented at 2nd Adding value to CO₂, Tarragona, Spain.

SUPERVISION OF BACHELOR AND MASTER THESIS

Supervision of 1 MSc thesis.

1. MSc Diego Roberto Ledesma Ruiz. Producción de hidrógeno mediante reformado de biogás con plasma – catálisis. University of Barcelona. 2021.